Recent Developments in 2D Nanomaterials for Chemiresistive-Type Gas Sensors

Recent Developments in 2D Nanomaterials for Chemiresistive-Type Gas Sensors

Seon-Jin Choi,[1,*] *and Il-Doo Kim*[2,3*]

[1]Department of Chemistry, Massachusetts Institute of Technology, 77 Massachusetts Avenue, Cambridge, Massachusetts 02139, United States

[2]Department of Materials Science and Engineering, Korea Advanced Institute of Science and Technology (KAIST), 291 Daehak-ro, Yuseong-gu, Daejeon 34141, Republic of Korea

[3]Advanced Nanosensor Research Center, KAIST Institute for the NanoCentury, KAIST, Daejeon 34141, Republic of Korea

*Address correspondence to seonjin@mit.edu, idkim@kaist.ac.kr

Keywords: 2D materials, nanosheets, chemiresistive-type, gas sensors, wearable sensors

Abstract

Two-dimensional (2D) nanostructures are gaining tremendous interests due to the fascinating physical, chemical, electrical, and optical properties. Recent advances in 2D nanomaterials synthesis have contributed to optimization of various parameters such as physical dimension and chemical structure for specific applications. In particular, development of high performance gas sensors is gaining vast importance for real-time and on-site environmental monitoring by detection of hazardous chemical species. In this review, we comprehensively report recent achievements of 2D nanostructured materials for chemiresistive-type gas sensors. Firstly, the basic sensing mechanism is described based on charge transfer behavior between gas species and 2D nanomaterials. Secondly, diverse synthesis strategies and characteristic gas sensing properties of 2D nanostructures such as graphene, metal oxides, transition metal dichalcogenides (TMDS), metal organic frameworks (MOFs), phosphorus, and MXenes are presented. In addition, recent trends in synthesis of 2D heterostructures by integrating two different types of 2D nanomaterials and their gas sensing properties are discussed. Finally, this review provides perspectives and future research directions for gas sensor technology using various 2D nanomaterials.

1. Introduction

Since the discovery of graphene as a unique two-dimensional (2D) layered structure, various 2D nanomaterials are gaining intensive attention in fundamental analysis as well as application in various research fields.[1-3] Generally, 2D layered nanomaterials possess large surface area and high surface-to-volume ratio. In addition, their unique structures and atomically thin layers are attractive due to the distinctive material properties, which cannot be achieved with conventional bulk structures. Recent advances in synthesis process and discovery of new types of 2D nanomaterials, including transition metal dichalcogenides (TMDs), metal-organic frameworks (MOFs), metal oxides, black phosphorus, as well as transition metal carbides and carbonitrides (MXene), further diversify material compositions and properties.[4, 5] As general synthesis techniques, mechanical and chemical exfoliations have been demonstrated to obtain atomically thin 2D nanomaterials. In addition, various synthesis strategies including solution phase reaction, hydrothermal reaction, chemical vapor deposition, and electrodeposition have been exploited to form various 2D nanomaterials.[6]

So far, numerous applications have been demonstrated using 2D nanomaterials such as optical electronics,[7, 8] chemical catalysts,[9] energy conversion devices,[10-12] and biomedical uses.[13-15] In addition, sensing characteristics of 2D nanomaterials with layered structures have been investigated for detection of biological compounds in solution.[16] In particular, gas sensing properties of various 2D nanomaterials have been continuously investigated for further optimization of gas sensing performance.[17-24]

2D layered nanomaterials are advantageous for gas sensing application due to their large surface area, which facilitates surface reactions. For the chemiresistive-type gas sensors, electrical resistivity or conductivity are altered due to the surface reaction between chemical analytes and 2D nanomaterials. To further enhance gas sensing performance, various synthetic techniques especially optimized for formation of porous layered structures have been

proposed to accommodate facile gas transport into the sensing layers and improve activated chemical reaction at the edge sites of 2D layers.[25] Mechanical stability of 2D layered structure is advantageous for flexible and bendable electronics.[26] Recently, 2D nanomaterials were integrated on a flexible and portable device to detect chemical analytes for real-time wearable sensing applications.[26, 27] In particular, graphene and TMDs have been mainly demonstrated for wearable gas sensors integrated on a flexible substrate.[28]

In this review, we comprehensively highlight recent research studies on chemiresistive-type gas sensors using diverse 2D nanomaterials. Firstly, the basic sensing principle is discussed for understanding chemiresistive-type gas sensors with emphasis on surface charge transfer and Schottky barrier modulation. Then, recent progresses in fabrication techniques of the 2D nanomaterial-based gas sensors and their fascinating gas sensing characteristics are introduced. In particularly, the sensing performances of various 2D nanomaterials such as graphene, TMDs, metal oxides, MOFs, black phosphorus, MXene, and their composites are summarized and compared. Finally, the perspectives of novel 2D nanomaterials-based gas sensors in the aspects of high performance sensing characteristics and facile sensor fabrication routes are highlighted.

2. Basic sensing principle of 2D nanostructures

Various explanations on the chemiresistive-type sensing behavior have been proposed in literature. It is obvious that the charge transfer occurs on the surface of 2D layered nanomaterials when gas molecules are exposed on 2D layers, which results in modulation of overall conductivity (resistivity) of sensing layers. In general, the electrical property of 2D nanomaterials can be controlled with respect to the charge affinity of gas species. In other words, oxidizing gas molecules such as NO_2 and NO tend to withdraw electrons from 2D nanomaterials, whereas reducing gas molecules including most volatile organic compounds

(VOCs) donate electrons to the 2D nanomaterials. As illustrated in Figure 1, the surface charge transfer (i) can generally occur on the surface by direct exchange of charge carriers between adsorbed gas species and 2D nanomaterials. For *p*-type 2D nanomaterials, an increase in conductivity is generally observed when the sensing layer is exposed to oxidizing gas molecules. Unlike oxidizing gases, reducing gases decrease the conductivity of the sensing layer. Opposite conductivity transitions occur for the case of *n*-type 2D materials toward oxidizing and reducing gases, respectively. The surface charge transfer is commonly evidenced by computational simulation such as first-principles calculations based on density functional theory (DFT).[29, 30]

Another important interpretation of sensing behavior is charge carrier transfer by Schottky barrier modulation during exposure of the sensing layer to analyte gases.[31] The charge transfer property can be manipulated by fundamental understanding of interfacial phenomena upon interaction with chemical molecules. As shown in Figure 1, adsorption of gas molecules on a 2D nanomaterial can induce transitions of built-in potential ($V_{built\text{-}in}$) as well as Schottky barrier (E_{SB}) (ii). In other word, Fermi level of *n*-type sensing layer tends to move toward the valence band when electron withdrawing NO_2 is absorbed, which results in decrease in conductivity due to the increase of Schottky barrier and decreased built-in potential. In contrast, the Fermi level moves close to the conduction band under exposure to electron donating NH_3, thereby increasing conductivity by decreasing Schottky barrier and increasing built-in potential. The opposite conductivity transitions occur in the case of *p*-type sensing layer since the majority charge carriers are holes. Specifically, Fermi level of *p*-type sensing layer moves toward the valence band when the sensing layer is exposed to NO_2. This results in decrease of Schottky barrier and increased built-in potential. The opposite transition occurs under electron donating NH_3 by decreasing the conductivity of *p*-type sensing layer. In this regard, the sensing characteristic can be further manipulated by controlling the Schottky

barrier and the built-in potential to maximize conductivity transition. In addition, chemical doping in 2D layered nanomaterials can further optimize gas sensing property by engineering interfacial potential alignment, thus facilitating Schottky barrier modulation.

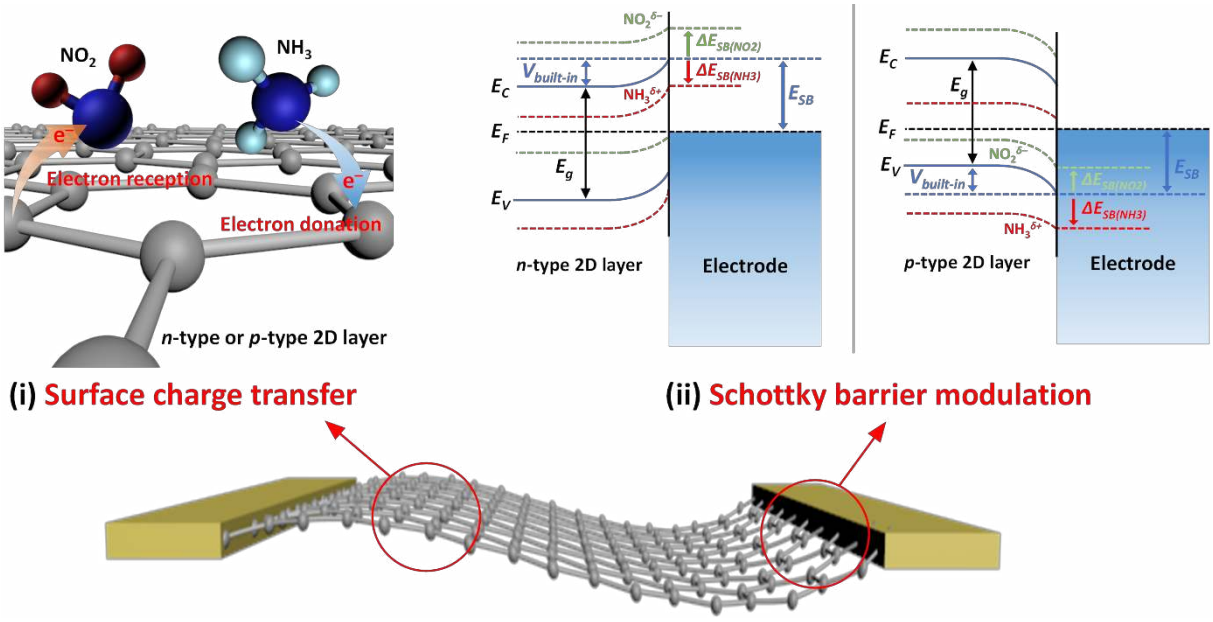

Figure 1. Schematic illustration of gas sensing mechanisms of 2D layered nanomaterials.

3. 2D nanomaterials for gas sensors

Recent advances in synthesis techniques have resulted in the emergence of various 2D nanostructures. Unique layered structures with atomic thickness exhibit exceptionally high surface area, which is advantageous for gas sensing applications. In this part, we introduce recent development of 2D nanostructures such as graphene, TMDs, metal oxides, MOFs, phosphorus, MXenes, and emerging layered composites for chemiresistive type gas sensors (**Figure 2**).

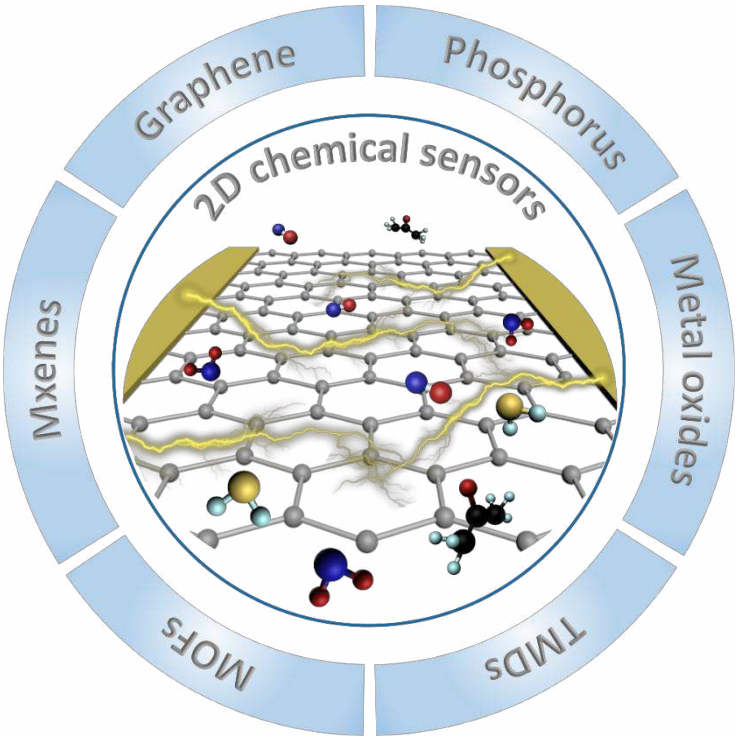

Figure 2. Diverse 2D layered nanostructures for chemiresistive-type chemical sensors.

3.1 Graphene and its derivatives

Graphene is a fascinating 2D layer possessing high electrical conductivity, optical transparency, and mechanical stability. Chemical sensing property of graphene was first investigated about a decade ago, and electrical signal transitions were observed by changing local carrier concentration in graphene during adsorption and desorption of gas molecules.[32] Since the first observation of chemical sensing property, graphene and graphene derivatives have been widely used to investigate chemical sensing properties. Previous reviews have emphasized in-depth studies of graphene-based materials for chemical sensing applications.[22, 33-35] Single-layer graphene as well as graphene derivatives including graphene oxide (GO), reduced graphene oxides (RGO), chemically modified graphene, and graphene composites have been synthesized and demonstrated as chemical sensors. **Table 1** presents summary of recent research achievements on the use of graphene-based nanostructures in chemical sensing applications. Based on the previous studies, the major advantage of graphene-based

sensing nanostructures is the operation at low temperature, which can reduce power consumption for portable and wearable applications. Interestingly, various studies revealed that graphene derivatives and their composite nanostructures could exhibit high sensitivity and selectivity toward nitrogen dioxide (NO_2).

For practical application of graphene as chemical sensors, GO has several advantages such as facile synthesis for mass production and high degree of dispersion for uniform coating on a sensor substrate. In addition, oxygen functional groups and defects play a crucial role in adsorption of chemical molecules.[22] Choi *et al.* found that hydroxyl groups in GO can particularly enhance NO_2 sensing performance with high recovery rates.[36] Experimental result revealed that high response [$\Delta R/R_0$ (%)] of ~17% was achieved using GO film toward NO_2 at 5 ppm as compared to graphene and RGO sheets. This can be explained by semiconducting behavior of GO containing hydroxyl and epoxy groups, which is electrically sensitive to charge transfer between GO film and NO_2 molecules. Density functional theory (DFT) calculations confirmed the facile adsorption of NO_2 on carbon basal plane in GO particularly on hydroxyl groups, which are the predominant active sites for NO_2 adsorption. Nevertheless, high electrical resistance of GO film hinders its wide application as active sensing material due to large signal to noise which is originated from high base resistance of GO layer. Instead, reduced graphene oxide (RGO) sheets can provide much improved sensing performance due to their high electrical conductivity and defect sites for gas adsorption.

Various RGO sensors have been fabricated and demonstrated for chemical sensing property. In general, chemical and thermal reduction processes are employed to improve electrical conductivity of GO sheets.[37-40] Fowler *et al.* synthesized single-layer RGO film on interdigitated electrode arrays to investigate its detection capability toward NO_2 and ammonia (NH_3) gases.[37] In order to form RGO dispersion, GO was directly dispersed in anhydrous hydrazine solution (98%) and subsequently, the RGO dispersion was coated on the substrate

by spin-coating process. The responses [$\Delta R/R_0$ (%)] of the single-layer RGO film were –13% and 2.5% toward 5 ppm of NO_2 and NH_3, respectively, at room temperature. The opposite sign of response values was attributed to the *p*-type and *n*-type doping characteristic of NO_2 and NH_3, respectively. On the other hand, Lu *et al*. synthesized RGO sheets on Au interdigitated electrodes by thermal annealing of GO in Ar ambient to investigate sensing property toward NO_2.[39] GO sheets were firstly dispersed on the electrodes and subsequentthermal reduction was performed at 100, 200, and 300 °C for 1 h, respectively. The sensitivity [$(G_{gas}–G_{air})/G_{air}$] of RGO sensor after thermal reduction at 300 °C was 1.56 toward 100 ppm of NO_2 at room temperature.

Optical reduction of GO sheets is a powerful strategy to form RGO sheets by effectively eliminating oxygen functional groups and improve electrical property within a short time.[41-44] The optical reduction process is versatile to form RGO, in which the optical irradiation can be performed on a solid substrate and in solution medium.[42] In particular, optical reduction is advantageous considering that RGO can be formed on a flexible plastic substrate without causing damage to the substrate,[45, 46] which can be applicable to fabrication of wearable chemical sensors. Recently, Choi *et al*. investigated H_2S sensing characteristic using optically reduced GO sheets on a colorless polyimide (cPI) substrate for application in wearable chemical sensors (**Figure 3**).[47] Commercially available GO sheets were coated on the cPI substrate patterned with interdigitated Au electrodes. Subsequently, ultrafast optical irradiation, *i.e.*, intense pulse light (IPL), was performed using a xenon flash lamp on the GO-coated cPI substrate to form RGO sheets (IPL-RGO) (Figure 3a). As a result, approximately 100-fold enhancement in electrical conductivity was achieved in about 1 sec after reaching the current peak within 4 msec (Figure 3b). Surface chemical composition of IPL-RGO was investigated using X-ray photoelectron spectroscopy (XPS), which revealed a substantial reduction in oxygen functional groups including C=O were observed after IPL irradiation.

The reduction in oxygen functional groups was mainly achieved by photothermal energy even in air ambient within a few milliseconds.[42] The chemical sensing characteristic revealed that IPL-RGO exhibited distinctive resistance transition toward H_2S in the concentration range of 5–20 ppm at room temperature, whereas pristine GO exhibited negligible resistance change due to large signal noise (Figure 3c). The maximum sensitivity [$(R_{air}–R_{gas})/R_{air}$ (%)] was 0.238% toward H_2S at 20 ppm. In addition, consistent H_2S sensing characteristic was observed even after subjecting the IPL-RGO sheets to mechanical deformation up to 10^4 bending cycles. To investigate its potential application in wearable chemical sensors, IPL-RGO sheets were integrated on a watch-type sensing module, which successfully transmitted sensing date to a smartphone *via* wireless communication (Figure 3d). Consistent resistance transitions were observed with multiple exposure of the wearable sensing platform to 20 ppm of H_2S (Figure 3e). Various interfering analytes including toluene ($C_6H_5CH_3$), acetone (CH_3COCH_3), hydrogen (H_2), carbon monoxide (CO), methane (CH_4), and ethanol (C_2H_5OH) were evaluated at 20 ppm using the IPL-RGO sensors. Principal component analysis (PCA) revealed the selective pattern recognition of different analytes into distinctive clusters without overlap (Figure 3f).

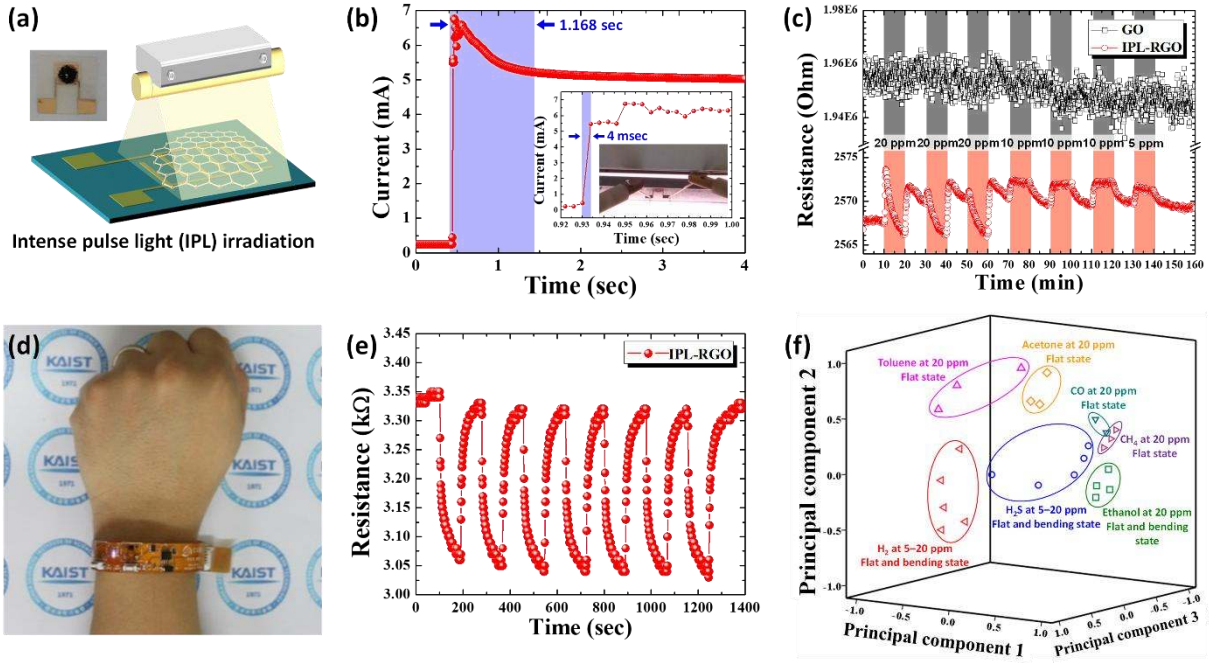

Figure 3. (a) Schematic illustration of optical reduction of GO using intense pulsed light (IPL) on cPI substrate. (b) Real-time current transition of GO during IPL irradiation. (c) H_2S sensing characteristic of GO and IPL-treated RGO (IPL-RGO) sheets at room temperature. (d) Camera image of wearable watch-type sensing platform integrated with the IPL-RGO sensor. (e) H_2S sensing characteristic of IPL-RGO sensor using the wearable sensing platform. (f) Principal component analysis (PCA) for selective pattern recognition of IPL-RGO sensor. Reprinted with permission from Ref.[47] Copyright (2016), Nature Publishing Group.

Chemical modification of graphene is gaining much interests in recent years to obtain improved sensing properties by doping with foreign atoms or functionalization of molecules on its surface. Chemical modification can be generally performed by adding various dopants such as sulfonic groups,[48] fluorine,[49, 50] and boron.[51] Yuan *et al.* proposed sulfonated RGO for NO_2 sensing at room temperature.[48] The chemical composition of sulfonated RGO was studied by XPS analysis. C/O atomic ratio of sulfonated RGO was 5.57, which was lower than 7.75 of RGO precursor due to functionalization using sulfonic groups. As a result, a 16.4-fold enhancement in response [G/G_0] was achieved toward NO_2 at 50 ppm with theoretical limit of detection (LOD) at 3.6 ppm. In addition, the sulfonated RGO exhibited good reversible sensing property upon repeated exposure to NO_2 since adsorbed NO_2 molecules can be effectively removed from the sulfonated RGO surface after N_2 injection.

The improved NO_2 sensing performance can be explained by the formation of SO_3^- groups on RGO leading to favorable adsorption of NO_2 molecules. The stronger electron-withdrawing ability of sulfophenyl group after NO_2 adsorption resulted in larger conductivity changes by increasing hole doping level in RGO sheets.

Very recently, fluorinated GO was synthesized for NH_3 sensors.[49, 50] Kim *et al*. synthesized fluorinated GO by dissolving fluorine source (XtalFluor-E) and GO dispersion in HF solution.[49] The atomic ratio of C to F was $C_{2.38}F$ with the fluorine atomic percentage of 25.21%, which was calculated by XPS analysis. The fluorinated GO exhibited enhanced response [$\Delta R/R_0$ (%)] of 121% as compared to the response (~6%) of pristine RGO at 500 ppm of NH_3 with good selectivity and reversible sensing property. On the other hand, Park *et al*. also reported fluorinated GO synthesized by gas-fluorination method for NH_3 detection.[50] GO sheets were exposed to fluorine gas at different partial pressures in the range of 0.1–0.5 bar with N_2 as balance gas. For the fluorine gas treatment at 0.1 bar, the atomic ratio of F/C was 8.7% with the fluorine atomic percentage of 4.94%. The maximum NH_3 sensitivity [$\Delta R/R_{N2}$ (%)] was approximately 7% at 100 ppm. The improved NH_3 sensing performance of fluorinated GO was mainly attributed to the fluorine functional groups on the surface of GO. The fluorine functional groups change the electronic structure of GO by hole doping due to the high electronegativity of fluorine. The adsorption of NH_3 resulted in the electron donation to the fluorinated GO, thereby increasing the resistance by decreased hole carrier concentrations. DFT calculations revealed that NH_3 molecules bind strongly to both O and OH groups on GO in the case of fluorine doping, rather than direct interaction of fluorine atoms with NH_3 molecules.[49]

With regard to chemical modification, boron-doped graphene was synthesized by bubbler-assisted chemical vapor deposition (CVD), and chemical detection capability toward NO_2 and NH_3 was investigated.[51] To dope boron into graphene, vapor mixture of triethylborane (TEB)

and hexane solutions was vaporized with Ar into the CVD reactor at 1000 °C for 5 min. The synthesized boron-doped graphene was transferred to a silicon wafer. The formation of a monolayer with the thickness of less than 1 nm was confirmed by atomic force microscopy. The atomic percentage of boron in graphene was found to be ~1.75%. The boron-doped graphene exhibited chemical sensing capability toward 1 ppb and 1 ppm of NO_2 and NH_3, respectively, under continuous UV light irradiation. The theoretical LOD was calculated to be 95 ppb for NO_2 and 60 ppb for NH_3 when the signal-to-noise ratio was a factor of 3. The improved NO_2 and NH_3 sensing properties of boron-doped graphene were mainly attributed to the strong adsorption of target analytes to the boron-doped graphene.

Not only chemical doping, but also introduction of defect can further improve chemical sensing property. Lee *et al*. revealed that defect density in graphene can enhance sensitivity up to 33% and 614% toward NO_2 and NH_3, respectively, as compared to the sensitivities of pristine graphene.[52] In order to control defect density in CVD-grown graphene, reactive ion etching technique was employed by controlling treatment power and oxygen flow, which resulted in the increase in the concertation of sp^3-type defects and vacancies by the detachment of carbon atoms. The ratio of sp^3/sp^2 increased from 15% for the pristine graphene to 21% for the defect-engineered graphene after reactive ion etching. As a result, the sensitivities [$\Delta R/R_0$ (%)] of the defect-engineered graphene increased to 53% and 25% toward NO_2 and NH_3 at 20 ppm, respectively. DFT calculations revealed that vacancies in graphene are essential to activate sensing of gas molecules. The positive effect of defects on sensing characteristic was also evidenced in field effect transistor (FET)-type chemical sensors, in which external defects on SiO_2 substrate can modulate sensitivity of graphene.[53]

Recently, single-layer graphene obtained by CVD as well as multilayered graphene derivatives have been integrated on a flexible substrate.[54, 55] However, graphene-based sensing layer exhibited inherent irreversible reaction kinetics, in which the baseline resistance

drifted under cyclic exposure to analyte gas due to sluggish recovery process.[37, 56, 57] To address this issue, operation of chemical sensors at elevated temperatures has been attempted by accelerating desorption rate during the refreshing process.[58] Kim *et al*. developed transparent and flexible all-graphene sensors on a polyimide substrate for improved NO_2 detection at an elevated temperature by self-activated operation (**Figure 4**).[59] Three-layer graphene sheets were grown by CVD process on a Cu foil at 1000 °C. In order to effectively generate heat during the self-activated operation, narrow graphene channel of 5 μm width and 5 mm length was patterned by oxygen plasma treatment. Subsequently, the three-layer graphene sheets were transferred to the flexible polyimide substrate (Figure 4a). The graphene sensor exhibited voltage-dependent self-activation wherein the operation temperature was 73.4 °C at 60 V (Figure 4b). The elevation of sensor temperature was attributed to the Joule heating in the micropatterned graphene under applied bias. The sensing characteristic was evaluated toward 5 ppm of NO_2 at different applied voltages in the range of 1–60 V. Improved sensitivity [$(R_{gas}–R_{air})/R_{air}$ (%)] of 12.49% was achieved at 60 V as compared to the sensitivity (4.47%) at 1 V (Figure 4c). In addition, selective NO_2 detection was observed with minor response toward interfering analytes such as NH_3, H_2O, CH_2CH_5OH, CH_3COCH_3 at the applied voltage of 60 V. In particular, improved response time (89 sec) and recovery time (579 sec) were obtained by increasing voltage at 60 V assisted by the Joule heating.

Graphene-based flexible and transparent chemical sensors were also fabricated by integration of single-layer graphene as a sensing layer and bi-layer graphene as a transparent heating layer.[60] The graphene layers were synthesized by CVD and transferred to a flexible and transparent polyethersulfone (PES) substrate. It is noted that the graphene heater and graphene sensing layer were electrically separated for reliable device operation. The effect of the bi-layer graphene heater on recovery process was investigated after exposure to NO_2 at 40 ppm. The sensitivity [$\Delta R/R_0$ (%)] toward NO_2 was observed to be 39% at room temperature.

However, substantially long recovery time over 3000 sec was required for the sensor to recover to its baseline level (Figure 4d). On the other hand, a very fast recovery time within 20 sec was achieved by operating the bi-layer graphene heater at 165 °C (Figure 4e). The bi-layer graphene heater was operated at 30 V corresponding to the power consumption of 1.7 W with the overall sensor dimension of 2 cm × 2 cm.

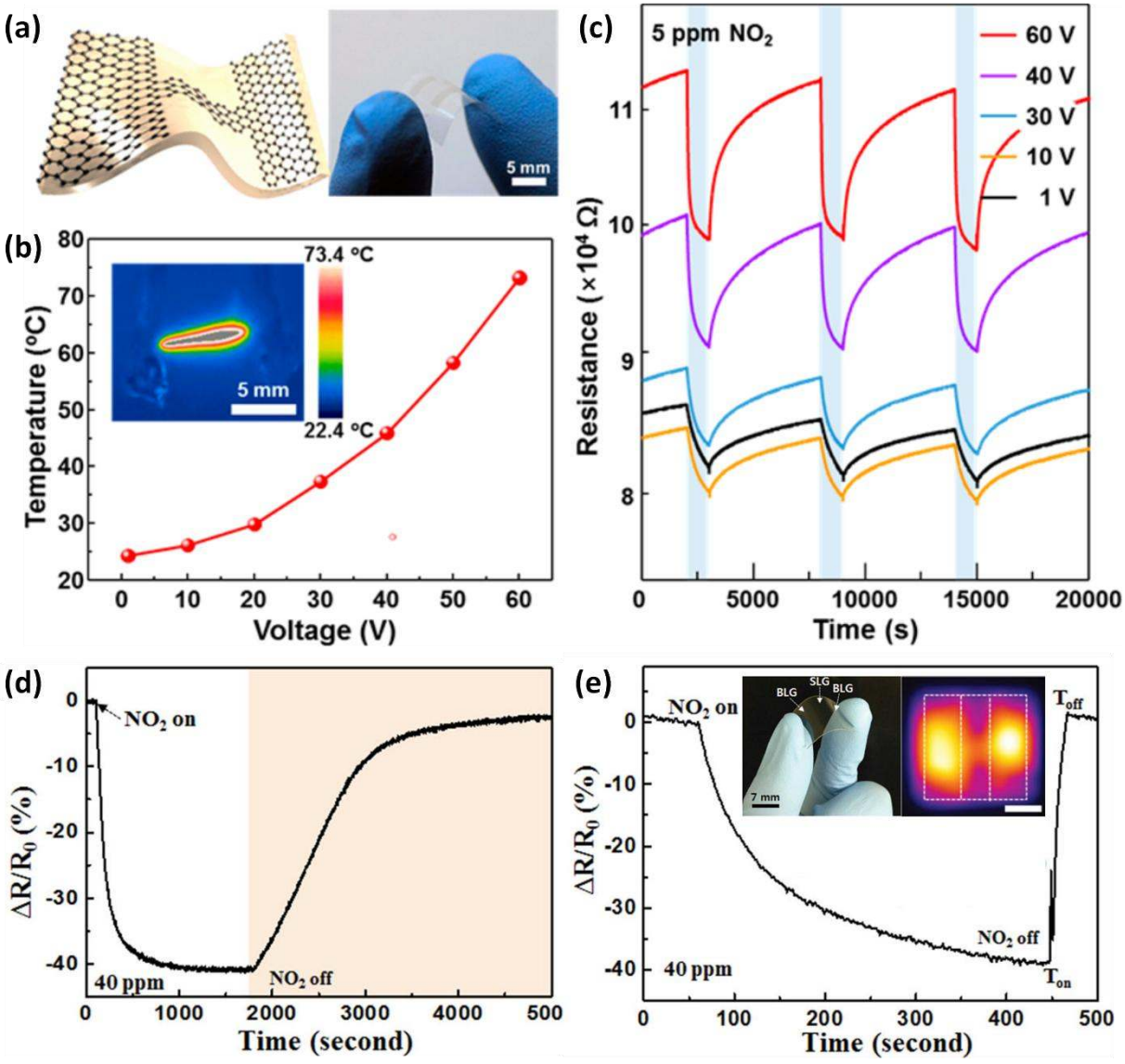

Figure 4. (a) Three-layer graphene sheets with micropatterned channel (width: 5 μm, length: 5 mm) on a flexible polyimide substrate. (b) Voltage-dependent self-activation of micropatterned graphene sensor in the applied voltages in the range of 1 V–60 V. (c) NO_2 sensing characteristic of the micropatterned graphene sensor at 5 ppm under the applied voltages in the range of 1 V–60 V. Reprinted with permission from Ref.[59] Copyright (2015), American Chemical Society. NO_2 (40 ppm) sensing characteristic of graphene-based flexible

sensor at room temperature with recovery process (d) without heater operation and (e) with heater operation (T_{on} =165 °C). Reprinted with permission from Ref.[60] Copyright (2014), Wiley.

Different types of conductive elements can be integrated on a flexible substrate to generate heat and accelerate response and recovery processes during gas sensing. For example, the conductive elements such as silver nanowires (Ag NWs),[61] metal nanotubes,[62] and metal mesh[63, 64] were employed on a plastic substrate as flexible heaters. Recently, Choi *et al.* investigated reversible NO_2 reaction kinetics of RGO sheets on a Ag NW-embedded cPI film, which can generate heat under applied voltage.[65] Filtration and transfer technique was employed to form partially embedded Ag NWs in the cPI film, wherein Ag NWs on a filter paper after vacuum filtration was transferred to a glass substrate by mechanical pressure. Subsequently, precursor solution of polyamic acid (PAA) was coated on the substrate using screen printing technique. The Ag NW-embedded cPI film was obtained after subsequent imidization process by annealing of PAA at elevated temperature. As a result, the Ag NW-embedded cPI film exhibited heat generation property under different applied voltages, *i.e.*, 0 V (22.7 °C), 1 V (35.3 °C), and 1.8 V (71.7 °C) (Figure 5a). Particularly, the Ag NW-embedded cPI film exhibited excellent long-term heating stability under continuous operation for 190 h, and mechanical stability up to 7200 bending cycles under heating operation. Optically reduced GO was integrated on the Ag NW-embedded cPI film to demonstrate reversible NO_2 reaction under different operating temperature. Figure 5b presents NO_2 sensing property of RGO sensing layer in the concentration range of 5–20 ppm at different operating temperatures. As evidenced in many studies, irreversible reaction toward NO_2 was observed at room temperature, in which the baseline resistance drifted to lower resistance value. The maximum deviation from the initial baseline resistance was 2.5% at room temperature toward 20 ppm of NO_2. On the other hand, remarkably improved reversibility

was achieved by increasing substrate temperature, wherein the minimum deviation was 1% at 71.7 °C. In addition, the sensitivity [$(R_0–R)/R_0$ (%)] of RGO sensor was 2.69% at 71.7 °C. The quantitative calculation by desorption rate constants revealed that approximately 1.7-fold enhancement in desorption rate was achieved by elevating substrate temperature to 71.7 °C as compared to the desorption rate at room temperature. Moreover, the reversible reaction capability was observed even in mechanically bent state with the bending angle of 30°, in which the maximum deviation from the initial resistance decreased from 4.1% to 2.4% by increasing the substrate temperature (Figure 5c).

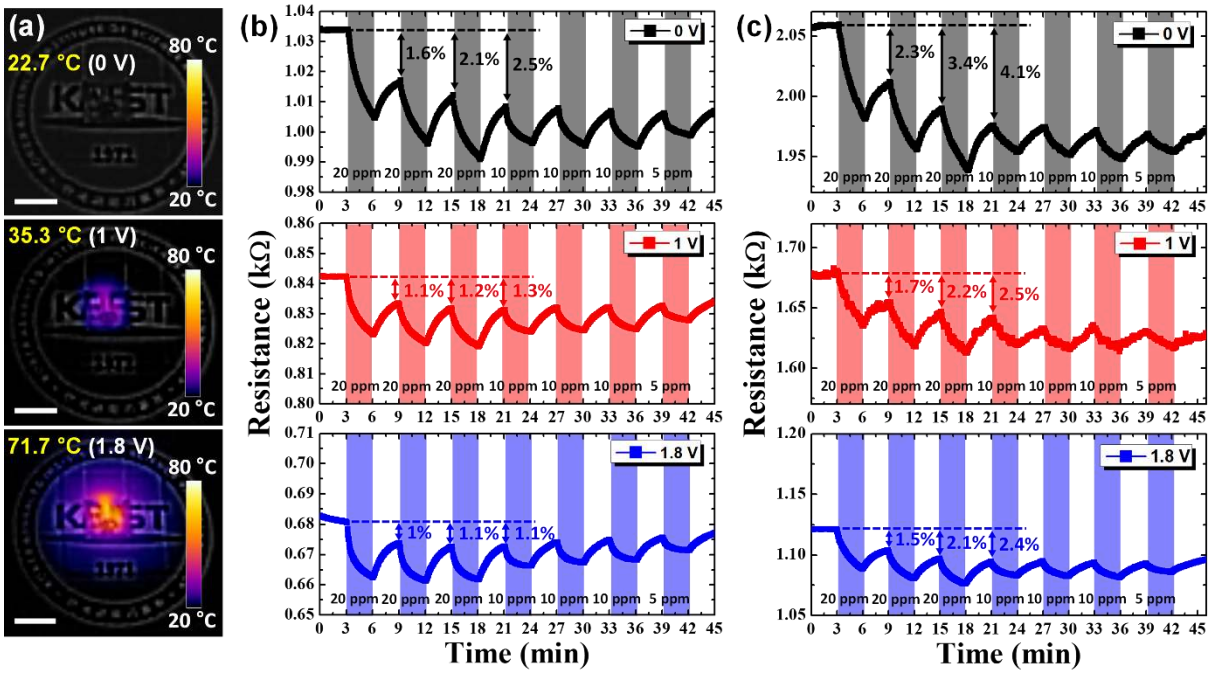

Figure 5. Infrared images of RGO sensing layer on the Ag NW-embedded cPI film at different applied voltages at 0 V (room temperature), 1 V (35.3 °C), and 1.8 V (71.7 °C). (scale bar: 1 cm). (b) Demonstration of reversible NO_2 sensing characteristic of RGO sensors on the Ag NW-embedded cPI film at different operating temperatures in (b) flat and (c) bent state with the bending angle of 30°. Reprinted with permission from Ref.[65] Copyright (2016), Wiley.

To improve reversibility even at low temperature, functionalization of various organic and inorganic materials with graphene-based sensing layer has been demonstrated. In particular, metallic nanoparticles (NPs) such as Pd,[66-68] Pt,[69] Ag,[70] and Al[71] have been widely used for catalytic functionalization of graphene layers. Li *et al.* synthesized Pd NP decorated RGO

composites by solution mixing method, in which chemically reduced GO solution and Pd NPs were mixed together to induce physical adsorption.[66] The composite Pd-RGO sensor exhibited sensitivity [ΔG/G] of 4% toward 2 ppb of NO with reversible sensing property. In addition, Lee *et al*. developed wireless hydrogen sensors based on Pt-decorated RGO on a flexible substrate.[69] Dynamic sensitivity transitions revealed that the hydrogen sensing was reversible with a sensitivity [$\Delta R/R_0$ (%)] of 9% at 50 ppm with fast (60 sec) recovery time. For the flexible NO_2 detection at room temperature, fully printed graphene composite of sulfonated graphene and Ag NPs on a flexible polyimide film was proposed .[70] A very fast recovery time within 20 sec and a high sensitivity [$(R_{air}–R_{gas})/R_{air}$ (%)] of 74.6% toward NO_2 at 50 ppm were achieved. Moreover, Cho *et al*. demonstrated flexible NO_2 sensor with improved sensitivity [$(R_{gas}–R_{air})/R_{air}$ (%)] of 2.89% at 1.2 ppm using Al-decorated multilayer graphene.[71]

Metal oxide nanostructures were also incorporated into graphene to improve sensitivity.[72] Various metal oxides such as Fe_2O_3,[73] WO_3,[74-76] SnO_2,[77] and Zn_2SnO_4[78] were recently demonstrated for the detection of H_2S, acetone, formaldehyde (HCHO). Very recently, graphitic carbon nitride (g-C_3N_4) nanosheets were hybridized with graphene for NO_2 sensing application.[79-81] Chen *et al*. synthesized g-C_3N_4/RGO stacked hybrid facilitating layer-by-layer self-assembly into multi-layered 2D structure.[79] The g-C_3N_4/RGO 2D hybrid exhibited *p*-type sensing property with a sensitivity [$(I - I_0)/ I_0$ (%)] of 110% toward NO_2 at 2 ppm, which is approximately three times higher than the sensitivity (35%) of pristine RGO at 2 ppm. In addition, high selectivity toward NO_2 was investigated with minor sensing capability toward interfering analytes such as NH_3, sulfur dioxide (SO_2), $C_6H_5CH_3$, ethyl acetate ($C_4H_8O_2$), and hexane (C_6H_{14}). Interestingly, g-C_3N_4/RGO hybrid presented selective sensing property under assistance of UV light irradiation by transforming *n*-type semiconducting behavior with the sensitivity of about –3% to 2 ppm. In addition, Hang *et al*. synthesized g-

C_3N_4 nanosheets by liquid-phase exfoliation method to incorporate into graphene.[81] 15 wt% g-C_3N_4 nanosheet-loaded graphene sensors exhibited the highest sensitivity [$(R_{gas}–R_{air})/R_{air}$ (%) = ~30%] toward 5 ppm of NO_2.

Organic nanostructures such as carbon dots,[82] carbon fibers,[83, 84] and, conducting polymer[85] have been synthesized and used for the detection of NH_3, NO_2, and dimethyl methylphosphonate (DMMP). In particular, one-dimensional fibrous structures such as polyurethane nanofibers[83] and cotton yarns[84] were combined with graphene for stretchable and wearable NO_2 sensing applications (Table 1). There are still numerous opportunities for improving chemical sensing property by variation in materials and compositions combined with graphene-based layers.

Table 1. Recent studies for chemical sensors using graphene-based 2D nanostructures.

Material	Sensing type	Response definition	Sensitivity (Response)	Detection limit	Testing ambient	Target gas	Selectivity	Response / recovery time	Operating temperature	Ref.
GO	Resistance change	$\Delta R/R_0$ (%)	~17% @ 5 ppm	650 ppb$^+$	Dry air	NO_2	NH_3, H_2	-/-	Room temp.	[36]
Multilayered RGO sheets	Resistance change	$(R_{air}–R_{gas})/R_{air}$ (%)	0.238% @ 20 ppm	1 ppm	Dry and humid air	H_2S	H_2, C_2H_5OH, CO, CH_4, CH_3COCH_3, $C_6H_5CH_3$	-/-	Room temp.	[47]
Sulfonated RGO	Conductivity change	G/G_0	24.7 @ 50 ppm	3.6 ppm$^+$	Dry N_2	NO_2	NH_3, H_2O, $C_6H_5CH_3$	-/-	Room temp.	[48]
Fluorinated GO	Resistance change	$\Delta R/R_0$ (%)	121% @ 500 ppm	6.12 ppb$^+$	Dry air	NH_3	NO_2, H_2, C_2H_5OH, $C_6H_5CH_3$, CH_3COCH_3	86 sec/ 116 sec	Room temp.	[49]
Graphene	Resistance change	$(R_{air}–R_{gas})/R_{air}$ (%)	39% @ 200 ppm	-	Air	NO_2	-	180 sec/-	Room temp.	[54]
Multilayered graphene	Resistance change	$\Delta R/R_0$ (%)	55% @ 4000 ppm	430 ppb$^+$	N_2	NH_3	-	-/-	Room temp.	[55]
Graphene	Conductivity change	$(I - I_0)/I_0$ (%)	65% @ 2.5 ppm	387 ppt$^+$	Air	NO_2	-	1400 sec/ 1500 sec	Room temp.	[56]
Multilayered graphene film	Resistance change	$\Delta R/R_0$ (%)	38.7% @ 5 ppm	200 ppb	Dry N_2	NO_2	-	-/-	Room temp.	[57]
Single graphene layer	Resistance change	R/R_0 (%)	8% @ 2.5 ppm	2.5 ppm	Dry N_2	NO_2	-	24 sec/ 50 sec	45 °C	[58]

Three-layer graphene channel layer	Resistance change	$(R_{gas}–R_{air})/R_{air}$ (%)	12.49% @ 5 ppm	6.87 ppb^{+}	Dry air	NO_2	NH_3, H_2O, CH_2H_5OH, CH_3COCH_3	89 sec/ 579 sec	73.4 °C	[59]
Single graphene layer	Resistance change	$\Delta R/R_0$ (%)	40% @ 40 ppm	0.5 ppm	Air	NO_2	-	<20 sec / 11sec	100–165 °C	[60]
Multilayered RGO sheets	Resistance change	$(R_{air}–R_{gas})/R_{air}$ (%)	2.69% @ 20 ppm	5 ppm	Dry air	NO_2	-	-/-	71.7 °C	[65]
Single-layer graphene-Pd	Resistance change	$(R_{gas}–R_{air})/R_{air}$ (%)	33% @ 1000 ppm	20 ppm	Dry N_2	H_2	-	~ 60 sec/-	Room temp.	[67]
Pt-RGO	Resistance change	$\Delta R/R_0$ (%)	~9% @ 50 ppm	1 ppm	Air	H_2	-	12 sec/ 60 sec	Room temp.	[69]
Sulfonated RGO-Ag	Resistance change	$(R_{air}–R_{gas})/R_{air}$ (%)	74.6% @ 50 ppm	0.5 ppm	Dry Air (30% RH)	NO_2	NH_3, CH_3OH, C_2H_5OH, H_2O $C_6H_5CH_3$	12 sec/ 20 sec	Room temp.	[70]
Multilayered graphene-Al	Resistance change	$(R_{gas}–R_{air})/R_{air}$ (%)	2.89% @ 1.2 ppm	-	Dry air	NO_2	NH_3	-/-	150 °C	[71]
Graphene-Zn_2SnO_4	Resistance change	R_{air}/R_{gas}	18.9 @ 1000 ppm	10 ppm	Air	HCHO	-	200 sec/ 50 sec	Room temp. (20 °C)	[78]
g-C_3N_4-RGO	Conductivity change	$(I - I_0)/I_0$ (%)	110% @ 2 ppm	100 ppb	Dry N_2	NO_2	NH_3, SO_2, $C_6H_5CH_3$, $C_4H_8O_2$, C_6H_{14}	138 sec/ 318 sec	Room temp.	[79]
g-C_3N_4-Graphene	Resistance change	$(R_{gas}–R_{air})/R_{air}$ (%)	~30% @ 5 ppm	600 ppb^{+}	Dry N_2	NO_2	-	-/-	150 °C	[81]

Carbon dot-RGO	Conductivity change	$(I - I_0)/ I_0$ (%)	74.3%% @ 5 ppm	10 ppb	Air	NO_2	NH_3, $CHCl_3$ C_2H_5OH, $C_6H_5CH_3$, CH_3OH, C_6H_{14}, CH_3COCH_3, DMF, DMMP, DCM	100 se/ 150 sec	Room temp.	[82]
RGO-Polyurethane nanofiber	Conductivity change	$(I - I_0)/ I_0$ (%)	~100% @ 2.5 ppm	50 ppb	Dry air	NO_2	-	120 sec/-	Room temp.	[83]
RGO-Cotton yarn	Resistance change	$(R_{gas}–R_{air})/R_{air}$ (%)	12% @ 1.25 ppm	0.25 ppm	Air	NO_2	C_2H_5OH, CH_3COCH_3, CO_2, C_2H_4	-/-	Room temp.	[84]
Inkjet-printed graphene-PEDOT:PSS	Resistance change	$(R_{gas}–R_{air})/R_{air}$ (%)	9.6% @ 500 ppm	10 ppm[+]	Dry air	NH_3	C_2H_5OH, $C_6H_5CH_3$, CH_3OH, CH_3COCH_3	3 min/ 5 min	Room temp.	[85]
Ozone treated graphene	Resistance change	$(R_{air}–R_{gas})/R_{air}$ (%)	19.7% @ 200 ppm	1.3 ppb[+]	Air	NO_2	-	-/-	Room temp.	[86]
Holey RGO	Resistance change	$(R_{gas}–R_{air})/R_{air}$ (%)	54% @ 12.5 ppm	60 ppb	Dry air	NO_2	NH_3, CO, H_2S, H_2	-/-	Room temp.	[87]
Single crystalline graphene	Resistance change	$(R_{gas}–R_{air})/R_{air}$ (%)	828% @ 50 ppb	-	Air	DMMP	-	-/-	Room temp.	[88]
RGO	Resistance change	$\Delta R/R_0$ (%)	~6% @ 75.7% RH	4.3% RH	Dry air	H_2O	-	4 sec/ 10 sec	Room temp.	[89]

[+]Theoretical detection limit, DMMP=dimethylmethylphosphonate

3.2 Transition metal dichalcogenides (TMDs)

As emerging 2D nanomaterials, TMDs are getting tremendous attention for fundamental understanding of material properties and application in various research fields.[3, 90-95] The proposed synthesis strategies of 2D TMDs include mechanical exfoliation, electrochemical intercalation, sonication, and CVD.[96] Unique semiconducting property of TMDs have paved the way for technological breakthroughs in sensing applications such as optical sensing,[97, 98] DNA sensor,[99, 100] tactile sensor,[101] and gas sensor.[24] **Table 2** presents recent progresses of diverse 2D TMDs for application in gas sensors. Among the various TMDs, molybdenum disulfide (MoS_2) has been intensively studied in terms of its synthesis and sensor applications.[102-105] Late *et al*. synthesized MoS_2 by mechanical exfoliation using the Scotch-tape and investigated sensing behavior toward NO_2 and NH_3.[30] Different numbers of MoS_2 layers were deposited on a SiO_2/Si substrate to fabricate field effect transistor (FET) (**Figure 6a**). Scanning electron microscopy (SEM) analysis showed two-layer MoS_2-based FET (Figure 6b). The gas sensing characterization revealed that improved sensitivity [$(R_{gas}–R_{N2})/R_{N2}$ (%)] was achieved using five-layer MoS_2 FET as compared to two-layer MoS_2 FET. Particularly, five-layer MoS_2 FET exhibited the highest sensitivity (1372%) toward NO_2 at 1000 ppm under applying positive gate voltage (+15 V), while reduced sensitivity was observed toward NH_3 (Figure 6c). Single-layer and multi-layer MoS_2-based FETs have also been demonstrated for nitrogen monoxide (NO) sensors at room temperature.[106] The MoS_2 layers were prepared by mechanical exfoliation using bulk MoS_2 layered structure. The sensing results revealed that multi-layer MoS_2, *i.e.*, bilayer (2L), exhibited stable and sensitive response [$\Delta I/I_0$ (%)=80%] toward NO at 2 ppm with *n*-type sensing property, whereas single-layer MoS_2 showed unstable current transitions. Mechanically exfoliated monolayer MoS_2 also exhibited sensing property toward 1 ppm of triethylamine (TEA) with the sensitivity [$\Delta G/G_0$ (%)] of ~3 % at room temperature.[107] The monolayer MoS_2 was particularly

selective to TEA with minor responses to interfering analytes such as tetrahydrofuran (THF), nitrotoluene (TN), 1,5-dichloropentane (DCP), 1,4-dichlorobenzene (DCB), and methanol (CH_3OH). In a different synthesis strategy, CVD-grown monolayer MoS_2 was formed on SiO_2/Si substrate to investigate NO_2 and NH_3 sensing characteristic.[31] In particular, sensing electrodes of Ti/Au were deposited using e-beam evaporation to form Schottky contact. As a result, over 20% decrease in current was observed upon exposure to 20 ppb of NO_2 due to the Schottky barrier modulation, in which the Fermi level of MoS_2 moved toward the valence band. On the other hand, lowering the Schottky barrier height increased the current up to 40% at 1 ppm of NH_3, which resulted from the Fermi level shift toward the conduction band. In addition, Cho *et al*. investigated NO_2 sensing property of CVD-grown MoS_2 with three atomic layers, which demonstrated high sensitivity [$(R_{gas}–R_{N2})/R_{N2}$ (%)] of ~120% at 1 ppm with the LOD of 120 ppb at room temperature.[108] Chemical reaction by sulfonation of Mo layers has also been proposed as a vapor phase growth technique by heating sulfur powder in Ar ambient.[109] After the sulfurization, the average thickness of MoS_2 film was 20 nm. The MoS_2 film sensor exhibited NH_3 sensing property with the sensitivity [$\Delta R/R_0$ (%)] of 0.1% at 30 ppm with a theoretical LOD of 51 ppb at room temperature. Recently, vertically aligned MoS_2 was proposed by rapid sulfurization method using CVD process for improved NO_2 sensors as compared to horizontally aligned MoS_2.[110] It has been reported that edge sites of nanostructured MoS_2 exhibit much higher catalytic effects compared to the basal plane.[111] For this reason, approximately 5-fold enhancement in sensitivity was obtained for vertically aligned (edge exposed) MoS_2 film compared to the horizontally aligned (basal plane exposed) MoS_2 film, which was attributed to the stronger binding energy of NO_2 molecules to the edge sites.

The effect on sensing characteristic with respect to the number of layers was investigated using different types of TMDs such as tungsten disulfide (WS_2). Different numbers of layers

were formed by atomic layer deposition (ALD)-based process, wherein very thin WO_3 was deposited on a 6 inch SiO_2/Si substrate and subsequently sulfurized at 1000 °C using mixed flow of Ar and H_2S.[112] Monolayer (1L), bilayer (2L), and tetra-layer (4L) of WS_2 nanosheets were prepared by controlling deposition cycles using ALD. In order to investigate current transition of WS_2 nanosheets, thermal evaporation was used by forming Cr/Au electrodes with a separation distance of 1 mm (Figure 6d). Gas sensing evaluation was performed at 100 °C toward acetone (0.5–10 ppm) and NO_2 (25–500 ppm). Decrease in current transitions was observed when the WS_2 nanosheets were exposed to acetone (Figure 6e). In particular, WS_2 nanosheets with 2L and 4L could detect as low as 0.5 ppm of acetone, whereas 1L WS_2 nanosheet exhibited negligible current changes. On the other hand, increasing current transitions were observed toward NO_2 (Figure 6f). Similarly, the 4L WS_2 nanosheets showed improved NO_2 sensing property. The WS_2 nanosheets exhibited *p*-type sensing behavior due to the formation of high Schottky barrier between the metal contact and WS_2 nanosheets, which blocked electron carrier transport. When the sensor was exposed to acetone a decrease in current was observed, which was attributed to the downward bending of the valence band by limiting hole transport through the WS_2 nanosheets. In contrast, upward bending of valence band upon exposure of the sensor to NO_2 resulted in higher current by effectively transporting holes. In addition, the effect of the number of WS_2 layers on recovery speed after NH_3 sensing was investigated by Qin *et al.*[29] Although the response intensity decreased to 2.58% toward NH_3 at 250 ppm, the recovery time greatly shortened by 272 sec for the monolayer WS_2 as compared to the recovery time (2000 sec) for bulk WS_2. The poor recovery of multi-layered WS_2 nanosheets was explained by the intercalation and confinement of NH_3 molecules between WS_2 nanosheets, which resulted in stronger binding to WS_2. Theoretical studies about the adsorption of various gas molecules such as H_2, O_2, H_2O, NH_3, NO, NO_2, and CO have been performed based on DFT calculations.[113] The results revealed that facile

adsorption of specific molecules such as O_2, H_2O, NH_3, and NO_2 on WS_2 can facilitate charge transfer, thereby providing great potential for significantly enhanced gas sensors.

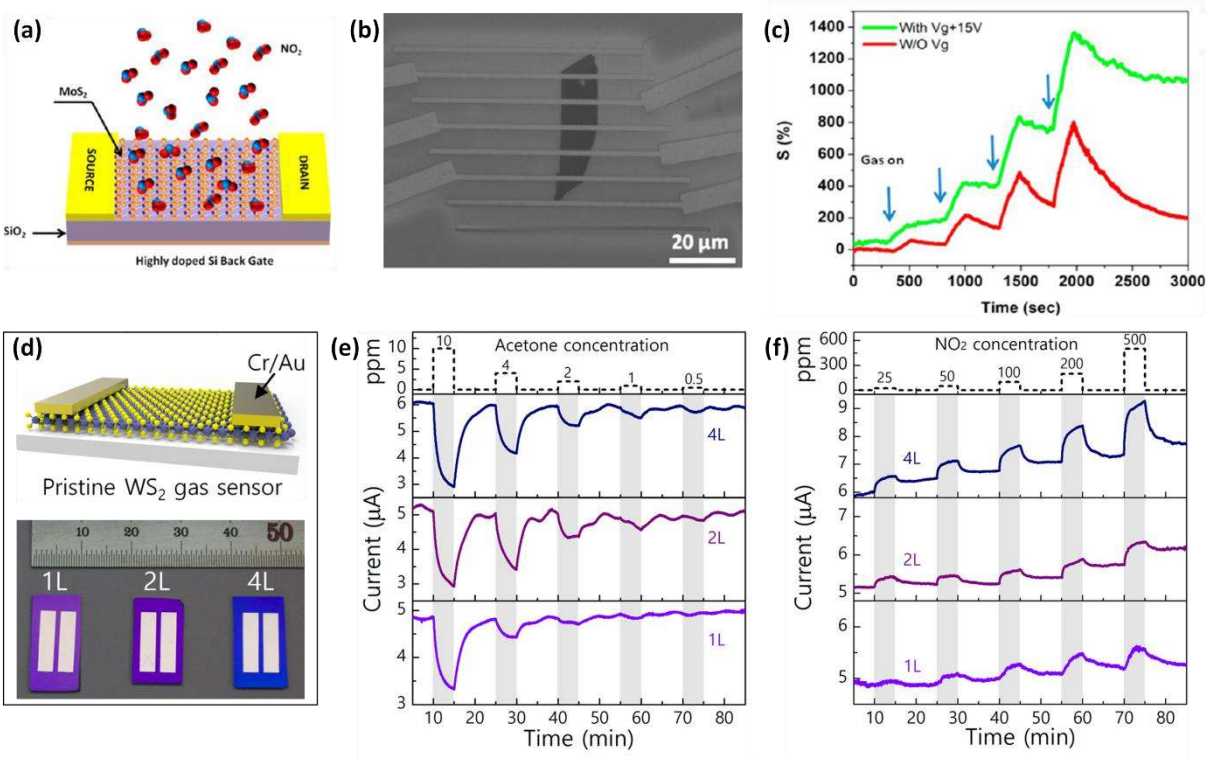

Figure 6. (a) Schematic illustration of MoS_2-based FETs for NO_2 sensing. (b) SEM image of two-layer MoS_2-based FETs. (c) NO_2 sensing property of two-layer MoS_2-based FETs with and without applied gate voltage at the gas concentration in the range of 100–1000 ppm. Reprinted with permission from Ref.[30] Copyright (2013), American Chemical Society. (d) Schematic illustration of WS_2 nanosheets on SiO_2/Si substrate with Cr/Au electrodes and camera image of WS_2-based sensors with different layer thicknesses. Gas sensing properties of WS_2-based sensors with different layer thicknesses toward (e) acetone and (f) NO_2. Reprinted with permission from Ref.[112] Copyright (2016), American Chemical Society.

Different types of 2D TMDs can be explored by replacing chalcogen component with selenium (Se). Late *et al*. demonstrated high-performance NH_3 sensor using single-layer $MoSe_2$ nanosheets obtained by mechanical exfoliation from bulk $MoSe_2$ crystals.[114] High sensitivity [$\Delta R/R_0$ (%)] of ~1200% was achieved toward 500 ppm of NH_3 at room temperature. Raman spectra analysis confirmed the charge transfer mechanism by exposure of the sensor to NH_3, thereby inducing *n*-doping in $MoSe_2$ nanosheets. Recently, the effect of

lateral sizes of $MoSe_2$ nanosheets on NO_2 detection was investigated by Zhang *et al.*[115] The $MoSe_2$ nanosheets were prepared by liquid phase exfoliation process, in which $MoSe_2$ powder was dispersed in organic solvent and ultrasonically treated for 2 h. Subsequently, various lateral sizes of $MoSe_2$ nanosheets were obtained at different centrifugation speeds. In general, increasing the centrifugation speeds resulted in decreased lateral sizes of $MoSe_2$ nanosheets. The average lateral sized of $MoSe_2$ nanosheets were 4.2, 1.2, and 0.6 μm at centrifugation speeds of 3000, 5000, and 8000 rpm, respectively. Sensing results revealed sensitivity [$\Delta I/I_0$ (%)] of ~90% toward 100 ppm of NO_2 using $MoSe_2$ nanosheets with small lateral size at room temperature. However, poor recovery led to drift of baseline after exposure to NO_2. On the other hand, $MoSe_2$ nanosheets with large lateral size exhibited reversible recovery although the sensitivity greatly decreased. The characteristic sensing properties of $MoSe_2$ nanosheets with different lateral sizes were attributed to different NO_2 adsorption energies at edge sites and basal plane sites. The $MoSe_2$ nanosheets exhibited *p*-type semiconducting property with increasing conductivity upon exposure to NO_2 due to the increased hole concentration.

As a new type of 2D TMDs, platinum diselenide ($PtSe_2$) has been synthesized by changing transition metal component and its NO_2 sensing property was investigated.[116] Large-scale $PtSe_2$ thin films were synthesized by thermally assisted conversion process on SiO_2/Si substrate at 400 °C. Specifically, Pt layers with a thickness, e.g., 0.5 nm, was deposited by sputtering on SiO_2/Si substrate. Subsequently, Pt layers were selenized by heating Se source under Ar/H_2 flow to transport the vaporized Se source in a tube furnace. The thermally converted $PtSe_2$ film exhibited 1T crystalline structure (**Figure 7a**). A high-angle annular dark-field scanning transmission electron microscopy (HAADF-STEM) image revealed polycrystalline structures containing nanoscale $PtSe_2$ domains (Figure 7b). The sensitivity [$\Delta R/R0$ (%)] of $PtSe_2$ film to 1 ppm of NO_2 was ~0.25% at room temperature (Figure 7c). In

particular, very fast response and recovery times in the range of 2–53.7 sec and 7.4–38.7 sec, respectively, were observed in the NO_2 concentration range of 0.1–1 ppm at room temperature. By replacing transition metal, rhenium disulfide (ReS_2) nanosheets were synthesized by CVD process.[117] Interestingly, vertically oriented arrays of ReS_2 nanosheets were obtained by sulfonation of ReO_3 using sulfur source in a tube furnace with Ar flow at 650 °C. The synthesis process can be achieved in single-step process to form ReS_2 nanosheets on an interdigitated electrode without further transferring process. The obtained ReS_2 nanosheets exhibited a distorted 1T structure as illustrated in Figure 7d. SEM analysis clearly showed ReS_2 nanosheets structure after sulfonation of ReO_3 (Figure 7e). In addition, Quasi-hexagonal pattern indicating (100) and (010) reflections was observed from a fast Fourier transform image (in the inset of Figure 7e). The humidity sensing property was evaluated in the relative humidity (RH) ranges of 30–80% using ReS_2 with about 10 nm thick (~14 layers) channel. The ReS_2 nanosheets exhibited *n*-type semiconducting behavior indicating increased carrier concentration upon exposure to H_2O. The response [$\Delta R/R_{Dry}$ (%)] of about 60% was observed toward 70% RH at room temperature (Figure 7f). In particular, very fast response and recovery times were achieved with approximately 20 sec and 10 sec, respectively. The humidity sensing properties have been exploited using diverse 2D TMDs such as few-layer MoS_2,[118] ultrathin VS_2 nanosheets,[119] and WS_2 nanosheets.[120] Jha *et al.* synthesized WS_2 nanosheets by liquid phase exfoliation from bulk WS_2 powder for application in humidity sensor.[120] Approximately, four-layer WS_2 nanosheets were obtained with lateral dimension of 1.2 μm. Ultrasensitive and stable response [$\Delta I/I_0$] of 37.5 was achieved at 80% RH after stabilization of baseline resistances in dry air (25% RH).

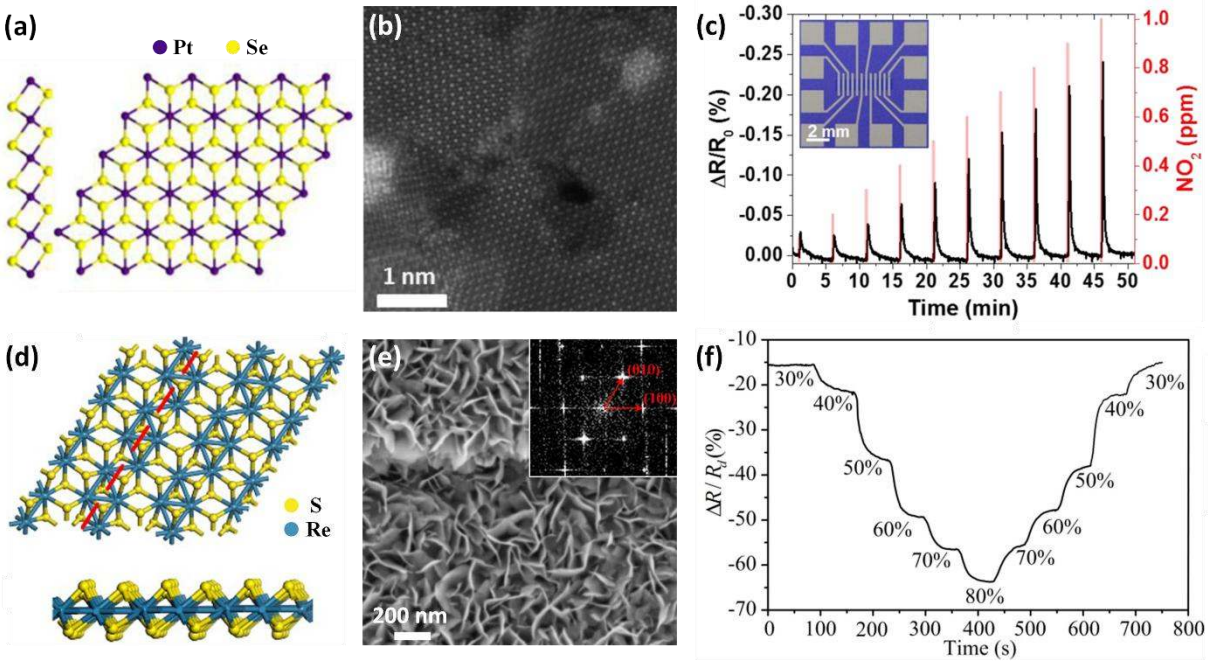

Figure 7. (a) Schematic illustration of 1T crystal structure of $PtSe_2$. (b) High-angle annular dark-field STEM (HAADF-STEM) image of $PtSe_2$. (c) Dynamic response transitions of $PtSe_2$ in the NO_2 concentration ranges of 0.1–1 ppm at room temperature. Reprinted with permission from Ref.[116] Copyright (2016), American Chemical Society. (d) Schematic illustration of ReS_2 crystal structure. (e) SEM image of ReS_2 nanosheets on interdigitated electrodes with the fast Fourier transform (FFT) pattern of the STEM image. (f) Humidity sensing characteristic of ReS_2 nanosheets in the RH ranges of 30–80%. Reprinted with permission from Ref.[117] Copyright (2016), IOP Publishing.

Various composites combined with 2D TMDs are gaining much interest to further improve sensing performances beyond pristine TMDs.[121] Diverse heterostructures by functionalization of TMDs with metallic nanostructures such as Ag NWs,[112] Au NPs,[122] Nb,[123] Pd NPs,[124] and Pt NPs[125] have been demonstrated for gas detection. He *et al.* proposed flexible MoS_2 thin film transistors (TFTs) by functionalization using Pt NPs for practical gas-sensing applications.[125] Single- and multi-layered MoS_2 sheets were synthesized by Li ion intercalation and dispersion processes.[126] The MoS_2 TFT arrays were formed by spin-coating on flexible polyethylene terephthalate (PET) substrate patterned with RGO electrodes (*i.e.*, source and drain electrodes) and Ag for contact pads (**Figure 8a**). The thickness of MoS_2 thin film and the channel length were 4 nm and 1.5 mm, respectively. The

MoS_2 film was functionalized with Pt NPs by immersing in aqueous solution containing K_2PtCl_4 and subsequent reduction using light irradiation. The gas sensing property of MoS_2 FET arrays was evaluated toward NO_2 and compared with other 2D sensing layers such as RGO sheets (Figure 8b). Pristine MoS_2 thin film and RGO sheets exhibited relatively low sensitivities [$\Delta I/I_0$ (%)] of 6.1% and 3.4% to 1.2 ppm of NO_2, respectively. Slightly improved sensitivity of RGO sheets functionalized with Pt NPs was observed, which was similar to sensitivity of pristine MoS_2 thin film. On the other hand, 3-fold higher sensitivity of ~16% to 1.2 ppm of NO_2 was achieved using MoS_2 thin film functionalized with Pt NPs (Figure 8c). In addition, Cho *et al*. decorated Pd NPs on MoS_2 flake to form 2D hybrid structure on a flexible polyimide substrate and investigated its gas sensing property toward NO_2 and NH_3 (Figure 8d).[121] In particular, reliable NH_3 sensing property was obtained at 150 °C even after mechanical bending stress for 5000 cycles.

Diverse metal oxides such as TiO_2 quantum dots,[127] SnO_2 nanocrystals,[128] and Fe_2O_3 NPs[129] have also been incorporated into 2D TMDs. Cui *et al*. proposed SnO_2 nanocrystal-decorated MoS_2 nanosheets, *i.e.*, MoS_2/SnO_2, for stable NO_2 sensing in air ambient at room temperature.[128] The SnO_2 nanocrystal behaves as strong *p*-type dopants for MoS_2 nanosheets, which forms *p*-type channels in the MoS_2 nanosheets. The MoS_2/SnO_2 composite was prepared by wet chemistry method, wherein $SnCl_4$ solution was mixed with MoS_2 dispersed solution. Subsequently, of MoS_2/SnO_2 nanohybrids were annealed in a tube furnace at 300 °C for 2 h under Ar ambient. As a result, MoS_2 nanosheets exhibited semiconducting trigonal prismatic phase (2H-MoS_2) composed of 2–3 layers after annealing. In addition, SnO_2 nanocrystals with the size the order of 2–5 nm were successfully decorated on MoS_2 nanosheets (Figure 8e). High-resolution transmission electron microscopy (TEM) analysis revealed rutile SnO_2 with the lattice spacing of 0.34 nm, which corresponds to (110) plane. Interestingly, the MoS_2/SnO_2 nanohybrids showed *p*-type semiconducting behavior, whereas

pristine MoS_2 nanosheets and SnO_2 nanocrystals exhibited *n*-type semiconducting characteristics. This result was mainly attributed to the electron transfer from MoS_2 nanosheets to SnO_2 nanocrystals due to the work function differences, which generated *p*-type channel in the MoS_2 nanosheets. By functionalization with SnO_2 nanocrystals, the MoS_2/SnO_2 nanohybrids exhibited high sensitivity [$\Delta G/G_0$ (%) = 28%] and selectivity to 10 ppm of NO_2 with excellent recovery property under repeated exposure to NO_2 (Figure 8f).

To further improve sensitivity and stability, 2D TMD nanosheets can be functionalized on the 1D fibrous scaffold for selective exposure of edge sites while preventing direct exposure to air ambient.[130] A polymeric scaffold was prepared by electrospinning technique from *N,N*-dimethylformamide (DMF) solution containing mixed polymers of polyacrylonitrile (PAN) and poly(styrene acrylonitrile) (SAN). After electrospinning of the solution, two-step heat-treatment was performed at 400 °C for 2 h and subsequently at 700 °C for 5 h to form multi-tubular carbon nanofibers (MTCNFs) resulting from the decomposition of SAN sacrificial channels. To prepare WS_2 functionalized MTCNFs, ammonium tetrathiotungstate was additionally dissolved in the electrospinning solution with identical heat-treatment condition. TEM analysis revealed that WS_2 functionalized MTCNFs had porous structure with multiple channels (Figure 8g). In addition, high-resolution TEM image confirmed the monolayered WS_2 nanoflakes on the surface of MTCNFs with the thickness and lateral dimension of 0.3 nm and 3.4 nm, respectively. In particular, edge abundant structures were obtained due to the uniaxial growth of 2D WS_2 nanoflakes in the MTCNFs, which is advantageous for gas reaction at the edge sites. As a result, improved NO_2 sensing characteristic was achieved for the WS_2 functionalized MTCNFs with the response [$\Delta R/R_0$ (%)] of 15% to 1 ppm of NO_2 at room temperature as compared to the response (15% at 4 ppm) of pristine CNF fiber (Figure 8h). In addition, stable response and recovery characteristics of WS_2 functionalized MTCNFs were observed during cyclic exposure of the sensing layer to 0.2 ppm of NO_2, whereas

pristine CNFs exhibited severe drift of baseline resistance with inappreciable response to 0.2 ppm. Moreover, the WS_2 functionalized MTCNFs could detect various chemical species including NH_3 and toluene as confirmed by pattern recognition using principal component analysis (PCA) (Figure 8i).

As evidenced in the recent studies, multi-compositional hybrid structures combined with 2D TMD nanosheets can be further explored to enhance sensitivity and stability for reversible sensing reaction.

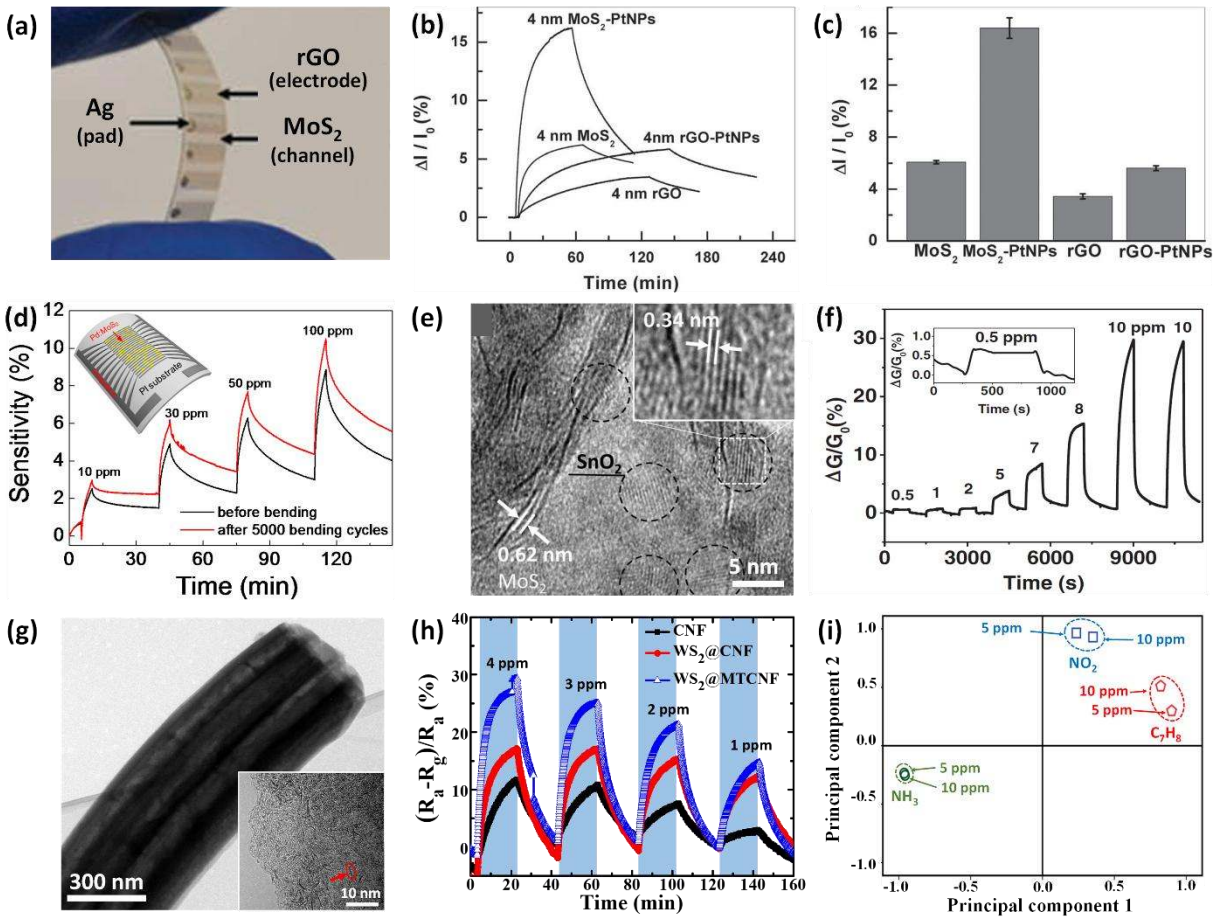

Figure 8. (a) MoS_2 thin film transistor functionalized by Pt NPs on the flexible PET film. (b) Dynamic response transitions and (c) response property of Pt NP-decorated MoS_2 TFT toward NO_2 at 1.2 ppm comparing with different 2D sheets and composites. Reprinted with permission from Ref.[125] Copyright (2012), Wiley. (d) Dynamic sensitivity transitions of Pd NP-decorated MoS_2 flakes on a polyimide substrate toward NH_3 at 150 °C before bending and after bending for 5000 cycles. Reprinted with permission from Ref.[121] Copyright (2015), MDPI. Reprinted with permission from Ref.[128] Copyright (2015), Wiley. (g) TEM analysis

of WS_2 functionalized MTCNFs with high-resolution TEM image in the inset. (h) Dynamic response transitions of carbon nanofibers (CNFs), WS_2 functionalized CNFs, and WS_2 functionalized MTCNFs toward NO_2 at room temperature. (i) Principal component analysis (PCA) toward NO_2, NH_3, and toluene using two sensors i.e., CNFs and WS_2 functionalized MTCNFs. Copyright (2015), MDPI. Reprinted with permission from Ref.[130] Copyright (2017), The Royal Society of Chemistry.

Table 2. Recent studies for chemical sensors using TMD-based 2D nanostructures

Material	Sensing type	Response definition	Sensitivity (Response)	Detection limit	Testing ambient	Target gas	Selectivity	Response / recovery time	Operating temperature	Ref.
Five-layer MoS_2	Resistance change	$(R_{gas}–R_{N2})/R_{N2}$ (%)	1372% @ 1000 ppm	10 ppm	Dry N_2	NO_2	-	-/-	Room temp.	[30]
Two-layer MoS_2 FET	Conductivity change	$\Delta I/I_0$ (%)	80% @ 2 ppm	0.8 ppm	N_2	NO	-	-/-	Room temp.	[106]
Monolayer MoS_2	Conductivity change	$\Delta G/G_0$ (%)	~3 % @ 1 ppm	10 ppb$^+$	Dry N_2	TEA	THF, CH_3OH, NT, DCP, DCB	~ 5 sec/ -	Room temp.	[107]
Atomic-Layered MoS_2 film	Resistance change	$(R_{gas}–R_{N2})/R_{N2}$ (%)	~120% @ 1 ppm	120 ppb	N_2	NO_2	H_2, H_2S, NH_3	-/-	Room temp.	[108]
MoS_2 thin film	Resistance change	$\Delta R/R_0$ (%)	0.1% @ 30 ppm	51 ppb$^+$	Dry N_2	NH_3	-	-/-	Room temp.	[109]
Vertically Aligned MoS_2 Layers	Resistance change	$\Delta R/R_0$ (%)	~10% @ 100 ppm	0.1 ppm	N_2	NO_2	C_2H_5OH	-/-	Room temp.	[110]
WS_2 nanosheet-Ag nanowire	Conductivity change	$\Delta I/I_0$ (%)	667% @ 500 ppm	25 ppm	Dry air	NO_2	CH_3COCH_3	-/-	100 °C	[112]
Monolayer WS_2	Conductivity change	$\Delta I/I_0$ (%)	~2.5% @250 ppm	50 ppm	Dry (30% RH) air	NH_3	CH_3COCH_3, CO, CH_3OH, CH_2O_2	200 sec/ 271.9 sec	Room temp.	[29]

Single-layer $MoSe_2$	Resistance change	$\Delta R/R_0$ (%)	~1100 @ 500 ppm	50 ppm	N_2	NH_3	-	~150 sec/ ~540 sec	Room temp.	[114]
$MoSe_2$ nanosheets	Conductivity change	$\Delta I/I_0$ (%)	~90% @ 100 ppm	5 ppm	N_2	NO_2	NH_3, CO, H_2S, CH_4	300 sec/ 600 sec	Room temp.	[115]
$PtSe_2$ films	Resistance change	$\Delta R/R_0$ (%)	~0.25% @ 1 ppm	9 ppb^+	N_2	NO_2	-	2 sec/ 7.4 sec	Room temp.	[116]
Vertically oriented ReS_2 nanosheets	Resistance change	$\Delta R/R_{Dry}$ (%)	~60% @ 70% RH	30% RH	N_2	Humidity	-	~20 sec/ ~10 sec	Room temp.	[117]
MoS_2 nanosheets	Resistance change	R_{Humid}/R_{Dry}	~3 @ 60% RH	10% RH	Dry air	Humidity	-	9 sec/ 17 sec	Room temp.	[118]
WS_2 nanosheets	Conductivity change	$\Delta I/I_0$	37.5 @ 80% RH	40% RH	Dry air (25% RH)	Humidity	-	13 sec/ 17 sec	Room temp.	[120]
Al-MoS_2 flake	Resistance change	$\Delta R/R_0$ (%)	~6% @ 5 ppm	-	Dry air	NO_2	NH_3	-/-	150 °C	[121]
Pd-MoS_2 flake	Resistance change	$\Delta R/R_0$ (%)	~5.5% @ 100 ppm	-	Dry air	NH_3	NO_2	-/-	150 °C	[121]
Au-MoS_2	Resistance change	$\Delta R/R_0$ (%)	~15% @ 1000 ppm	-	N_2	CH_3CO CH_3	C_6H_{14}, C_2H_5OH, CH_3CHO, $C_6H_5CH_3$	-/-	Room temp.	[122]

Nb-doped $MoSe_2$	Resistance change	$(R_{NO2}-R_{N2})/R_{N2}$ (%)	8.03% @ 3 ppm	-	N_2	NO_2	-	<30 sec/-	150 °C	[123]
MoS_2 Nanosheet-Pd Nanoparticle	Resistance change	R_{N2}/R_{H2}	10 @ 50000 ppm	500 ppm	N_2	H_2	NH_3, C_2H_5OH, CH_3COCH_3	40 sec/ 83 sec	Room temp.	[124]
Pt-MoS_2	Conductivity change	$\Delta I/I_0$ (%)	~16% @ 1.2 ppm	2 ppb[+]	N_2	NO_2	-	> 30 min	Room temp.	[125]
WS_2 nanosheet-TiO_2 quantum doc	Conductivity change	$\Delta I/I_0$ (%)	56.69% @ 500 ppm	20 ppm	Dry air	NH_3	CH_3COCH_3, C_2H_5OH, CH_3OH, CH_2O_2	200 sec/ 174 sec	Room temp.	[127]
SnO_2 nanocrystal-MoS_2 nanosheet	Conductivity change	$\Delta G/G_0$ (%)	28% @ 10 ppm	0.5 ppm	Dry air	NO_2	H_2, H_2S, CO, NH_3	408 sec/ 162 sec	Room temp.	[128]
WS_2-carbon nanofiber	Resistance change	$\Delta R/R_0$ (%)	28% @ 4 ppm	10 ppb[+]	Dry air	NO_2	NH_3, $C_6H_5CH_3$	224 sec/	Room temp.	[130]
WS_2 thin film	Resistance change	$\Delta R/R_0$ (%)	0.02% @ 5 ppm	1.4 ppm	N_2	NH_3	-	-/-	Room temp.	[131]
MUA-conjugated MoS_2	Resistance change	$\Delta R/R_0$ (%)	~15% @ 1000 ppm	1 ppm	N_2	CH_3COCH_3	$C_6H_5CH_3$, C_2H_5OH, C_6H_{14}, C_2H_5COH	-/-	Room temp.	[132]

[+]Theoretical detection limit, THF=tetrahydrofuran, TN=nitrotoluene, DCP=1,5-dichloropentane, DCB=1,4-dichlorobenzene, RH= relative humidity, MUA= mercaptoundecanoic acid, TEA=triethylamine

3.3 Metal oxide nanosheets

Metal oxides have been widely used as chemical sensing layers due to their superior gas sensitivity at elevated temperatures.[133] For example, diverse metal oxide nanostructures such as 0D NPs,[134, 135] 1D NWs,[136, 137] 1D nanofibers,[138-140] 1D nanotubes,[141-143] and hierarchical 3D architectures[144, 145] have been synthesized for gas sensing applications. In addition, the developments of 2D nanosheets using metal oxides are advantageous for gas sensing application considering their large surface area and the fact that chemical reactions mainly occur on the surface of metal oxides. In general, metal oxide nanosheets such as ZnO,[146-149] SnO_2,[150, 151] WO_3,[152] CuO,[153] and Co_3O_4[154] can be easily prepared by hydrothermal or solvothermal synthesis. In addition, other synthesis methods such as precipitation[155] and sonochemical process[156] for synthesis of ZnO nanosheets at room temperature have been proposed. Among the various metal oxide nanosheets, ZnO has been intensively studied for gas sensing application exhibiting *n*-type semiconducting property. Zeng *et al.* synthesized ZnO nanosheets by using facile two-step solution phase processes, in which ZnO seed layers were prepared first and subsequently ZnO nanosheets were grown on the ZnO seed layers by solvothermal process.[146] SEM observation revealed that ZnO nanosheets were interconnected into a network of sheets (**Figure 9a**). High-resolution SEM analysis confirmed that the average thickness of ZnO nanosheet was 30 nm (Figure 9b). In addition, TEM analysis showed quasi-single crystalline structure of ZnO with wurtzite phase. Gas sensing characteristic was evaluated that optimum operating temperature was observed to be 300 °C with the response [R_{air}/R_{gas}] of 11.2 toward 100 ppm of carbon monoxide (CO). In particular, very fast response and recovery times of 25 sec and 36 sec, respectively, were achieved at 100 ppm of CO at 300 °C with fully reversible sensing characteristic (Figure 9c). The ZnO nanosheets synthesized by sonochemical process, in which the ZnO nanosheets were obtained by chemical etching of ZnO nanorods, exhibited high sensitivity toward

acetaldehyde and formaldehyde at 220 °C.[156] The maximum sensitivities [$\Delta R/R_{gas}$ (%)] were 75% and 77% to 1 ppm of formaldehyde and acetaldehyde, respectively. In addition, the response was saturated within 10 sec with the theoretical LOD as low as 5 ppb. Recently, Xu *et al.* hydrothermally synthesized ZnO nanosheets whose exposed crystal facets were controlled to be (0001) and $(10\bar{1}0)$, and then investigated their sensing property toward ethanol.[147] The comparison study revealed that the ZnO nanosheets with dominant facet of (0001) exhibited greater response [R_{air}/R_{gas}] of 83.6 to 50 ppm of ethanol at 330 °C as compared to the sensitivity (28.4) of ZnO nanosheets with $(10\bar{1}0)$ facet. The improved ethanol response of ZnO nanosheets with the (0001) facet was mainly attributed to the favorable adsorption of gas molecules due to a large amount of oxygen vacancy defects and unsaturated dangling bonds of Zn.

As another *n*-type semiconducting material, SnO_2 nanosheets were synthesized by hydrothermal method, and then evaluated for the detection of ethanol and CO. Lou *et al.* prepared SnO_2 nanosheets with diameter in the range of 200–300 nm and thickness of about 15 nm.[150] The SnO_2 nanosheets exhibited high sensitivity and selectivity toward ethanol at 100 ppm with the response [R_{air}/R_{gas}] of 39.6 at 300 °C. In addition, very fast response and recovery times of 1 sec and 9 sec, respectively, were achieved toward 20 ppm of ethanol at 300 °C. Similarly, Zeng *et al*. proposed 2D SnO_2 nanosheets with tetragonal rutile crystal structure for CO sensing.[151] SEM observation revealed that the overall size of the SnO_2 nanosheets was approximately 150 nm with an average thickness of 50 nm. The maximum response [R_{air}/R_{gas}] was observed to be about 70 toward 100 ppm of CO at 300 °C with fast response and recovery times of 9 and 18 sec, respectively. In addition, a similar hydrothermal synthesis was used to prepare *n*-type WO_3 nanosheets by Wang *et al.*[152] Polygonal WO_3 nanosheets were obtained with the dimension of a few hundred nanometers with the thickness of 10 nm. Moreover, the WO_3 nanosheets exhibited single crystalline structure with

monoclinic phase. Sensing characteristic of WO_3 nanosheets toward NO_2 was investigated comparing against WO_3 NPs. The optimum operating temperature of WO_3 nanosheets was found to be 140 °C, which was slightly lower than the temperature (160 °C) of WO_3 NPs. The maximum response (R_g/R_a) of WO_3 nanosheets was 5.67 at 140 °C, while that of WO_3 NPs was 1.39 at 160 °C.

As *p*-type semiconducting materials, Co_3O_4 and CuO nanosheets were investigated for the detection of NH_3 and various VOCs.[153, 154] Co_3O_4 nanosheets were prepared by facile hydrothermal process without surfactant or sacrificial template and demonstrated as NH_3 sensing layers.[154] The Co_3O_4 nanosheets exhibited spinel structure with the average thickness of 39.5 nm. Interestingly, Co_3O_4 nanosheets exhibited NH_3 sensing property at room temperature with a sensitivity [R_g/R_a] of 9 at 100 ppm. Similarly, CuO nanosheets were prepared by hydrothermal method and investigated for sensing property toward acetone, ethanol, and methanol.[153] XRD analysis revealed the crystal phase of monoclinic structure with the average crystallite size of 18.79 nm. Characteristic sensing properties were observed with responses [R_g/R_a] of 7.725, 12.541, and 9.325 toward acetone, ethanol, and methanol, respectively.

In order to enhance gas sensing property, increasing porosity is advantageous by facilitating diffusion and surface reaction of gas molecules. In this regard, various porous metal oxide nanosheets have been proposed including ZnO nanosheets,[148] NiO nanowalls,[157] Co_3O_4 nanosheets,[158] In_2O_3 nanosheets,[159] for improved detection of acetylene, H_2S, ethanol, and NO_x, respectively. Yu *et al*. hydrothermally reacted nickel sulfate and aqueous ammonia in a ceramic tube followed by calcination of the resulting $Ni(OH)_2$ to synthesized porous NiO nanowall arrays for H_2S detection.[157] The obtained NiO nanowalls exhibited a cubic structure after calcination at 500 °C for 2 h. SEM observation showed that the NiO nanowalls were interconnected into a network (Figure 9d). The average thickness of the NiO nanowalls

was 14 nm as confirmed by high-resolution SEM image (in the inset of Figure 9d). The thin NiO nanowalls exhibited porous structure with the pore size in the range of 5.7–27.1 nm due to stacking of NiO NPs (Figure 9e). Gas sensing property was evaluated toward diverse organic and inorganic compounds including H_2S, ammonia, CO, ethanol, acetone, allyl chloride, formaldehyde, and triethylamine at optimum temperature of 92 °C. In particular, sensitive and selective detection of H_2S was achieved using NiO nanowalls with the response [R_g/R_a] of 12.9 to 10 ppm, which was approximately 5.6-fold enhanced response compared to the thick NiO film sensor (Figure 9f). In addition, the minimum detectable concentration was 1 ppb, which indicated superior resistance transition of the sensor.

Along with porous structure, ultrathin 2D metal oxides comparable to a few atomic layers can provide superior sensitivity by effective modulation of electrical resistance upon exposure to analyte molecules. Recent advances in synthesis techniques have opened up a broad range of 2D metal oxide layers with atomic thickness.[160] Molecular assembly of ultrathin metal oxide nanosheets is an example of generalized synthesis strategy to obtain various 2D metal oxide nanosheets including TiO_2, ZnO, Co_3O_4, WO_3, Fe_3O_4 and MnO_2.[161] For gas sensing application, atomically thin hydrated vanadium pentoxide ($V_2O_5{\cdot}0.76H_2O$) nanosheets have been investigated as H_2 sensor at an elevated temperature.[162] The ultrathin $V_2O_5{\cdot}0.76H_2O$ nanosheets were prepared through sol-gel chemistry by confinement of condensation reactions within the planar surface (*i.e.*, *ab* plane). Specifically, the $V_2O_5{\cdot}0.76H_2O$ nanosheets were synthesized by hydrolysis and condensation of vanadium (V) oxytripropoxide in a nitric acid (HNO_3) solution at 80 °C. Subsequently, hydrothermal reaction was performed at 200 °C for 12 h to form nanosheet structure. TEM analysis revealed that the $V_2O_5{\cdot}0.76H_2O$ nanosheets possessed single crystalline structure with a thickness of 1.5–1.6 nm, which is comparable to single atomic layer (Figure 9g-h). Nitrogen adsorption/desorption isotherms of $V_2O_5{\cdot}0.76H_2O$ nanosheets indicated exceptionally high Brunauer-Emmett-Teller (BET)

surface area of 164.4 m^2g^{-1}. Interestingly, shorter hydrothermal reaction time resulted in defects/holes on the surface of $V_2O_5 \cdot 0.76H_2O$ nanosheets with sizes in the range of 1.5–2.5 nm. For application as gas sensing materials, the $V_2O_5 \cdot 0.76H_2O$ nanosheets exhibited high sensitivity with low LOD toward H_2 at 250 °C (Figure 9i). An appreciable resistance transition [$(R–R_0)/R_0$ (%)] of about 2% to 10 ppm of H_2 was achieved using the $V_2O_5 \cdot 0.76H_2O$ nanosheets.

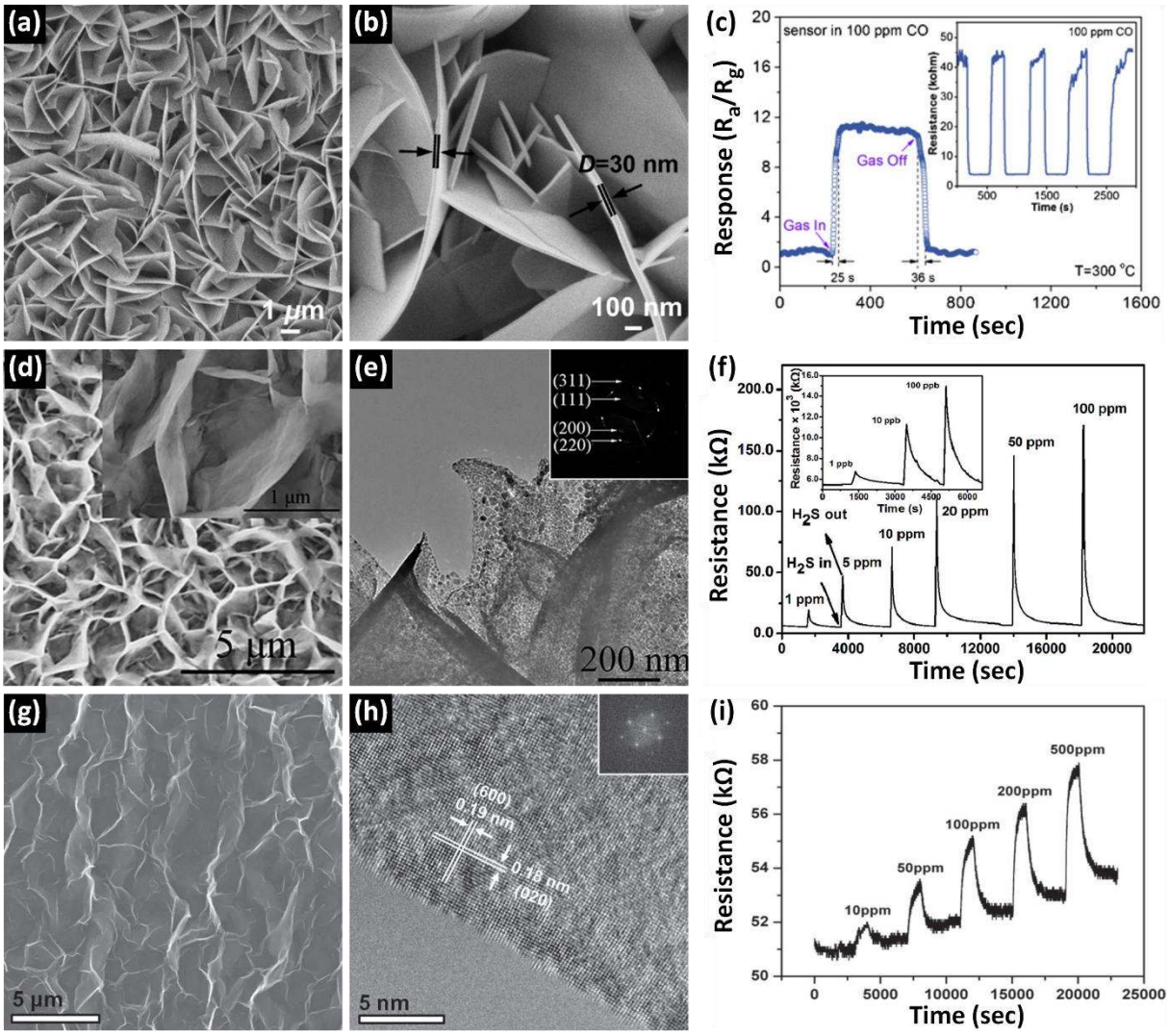

Figure 9. (a) SEM image and (b) high-resolution SEM image of ZnO nanosheets. (c) Dynamic response property of ZnO nanosheets toward 100 ppm of CO at 300 °C. Reprinted with permission from Ref.[146] Copyright (2012), Elsevier. (d) SEM and (e) TEM images of NiO nanowall arrays grown by hydrothermal method and subsequent calcination at 500 °C. (f) Dynamic resistance transitions of NiO nanowalls toward H_2S in the concentration range of 1

ppb–100 ppm at 92 °C. Reprinted with permission from Ref.[157] Copyright (2015), The Royal Society of Chemistry. (g) SEM and (h) high-resolution TEM images of hydrated vanadium pentoxide ($V_2O_5 \cdot 0.76H_2O$) nanosheets with FFT pattern in the inset of (h). (i) Dynamic resistance transitions of $V_2O_5 \cdot 0.76H_2O$ nanosheets toward H_2 in the concentration range of 10–500 ppm at 250 °C. Reprinted with permission from Ref.[162] Copyright (2013), Wiley.

Recently, atomically thin and porous RuO_2 nanosheets were synthesized by liquid phase chemical exfoliation and subsequent optical sintering technique on Ag NW-embedded cPI film for reversible NO_2 reaction.[163] The thin Ru oxide nanosheets were synthesized by protonation and an intercalation of organic ions into the bulk $NaRuO_2$ layered structure. Specifically, bulk $NaRuO_2$ was treated in hydrogen chloride (HCl) to exchange interlayer sodium (Na^+) with protons (H^+). Subsequently, intercalation of organic ions using tetrabutylammonium hydroxide aqueous solution was performed to exfoliate single-layered Ru oxide nanosheets. Multi-layered Ru oxide nanosheets were coated on the Ag NW-embedded flexible cPI substrate for application in flexible sensors. In order to form nanoscale pores on the Ru oxide nanosheets, optical sintering was performed by irradiation of xenon flash lamp for 15 msec to the Ru oxide nanosheets on the Ag NW-embedded flexible cPI substrate (**Figure 10a**). As a result, sub-5 nm scale pores were generated on the Ru oxide nanosheets while maintaining the 2D structure (Figure 10b). In addition, 2.65-fold reduction in electrical conductivity was observed compared to the pristine Ru oxide nanosheets. Moreover, surface chemical analysis using XPS revealed that dehydration of Ru oxide as well as fully oxidation occurred during the optical sintering process, which resulted in the porous RuO_2 nanosheets. Temperature-controlled NO_2 reaction property was demonstrated using the porous RuO_2 nanosheets as sensing layer while Ag NW-embedded cPI substrate was used as a heating film (Figure 10c). The substrate temperatures were confirmed by applying voltages to the Ag NW-embedded cPI heater, in which room temperature, 41.9 °C, and 80.3 °C were achieved at applied voltages of 0 V, 0.8 V, and 1.4 V, respectively. At room temperature, negligible resistance transition was observed toward NO_2 due to low reaction kinetics of the

porous RuO_2 nanosheets. Slightly increased response and recovery properties were observed at 41.9 °C (0.8 V). However, continuous drift in baseline resistance was observed due to the insufficient recovery kinetics. On the other hand, dramatically improved response and recovery characteristics were observed at 80.3 °C (1.4 V) with appreciable resistance transition at 5 ppm of NO_2, which was mainly attributed to the activated reaction kinetics at elevated temperatures. The maximum sensitivity [$(R_{gas}-R_{air})/R_{air}$ (%)] of the porous RuO_2 nanosheets was 1.124% at 80.3 °C (1.4 V) toward 20 ppm of NO_2. The improved reaction kinetics of the porous RuO_2 nanosheets were also observed under controlled operating temperature even in the bent state.

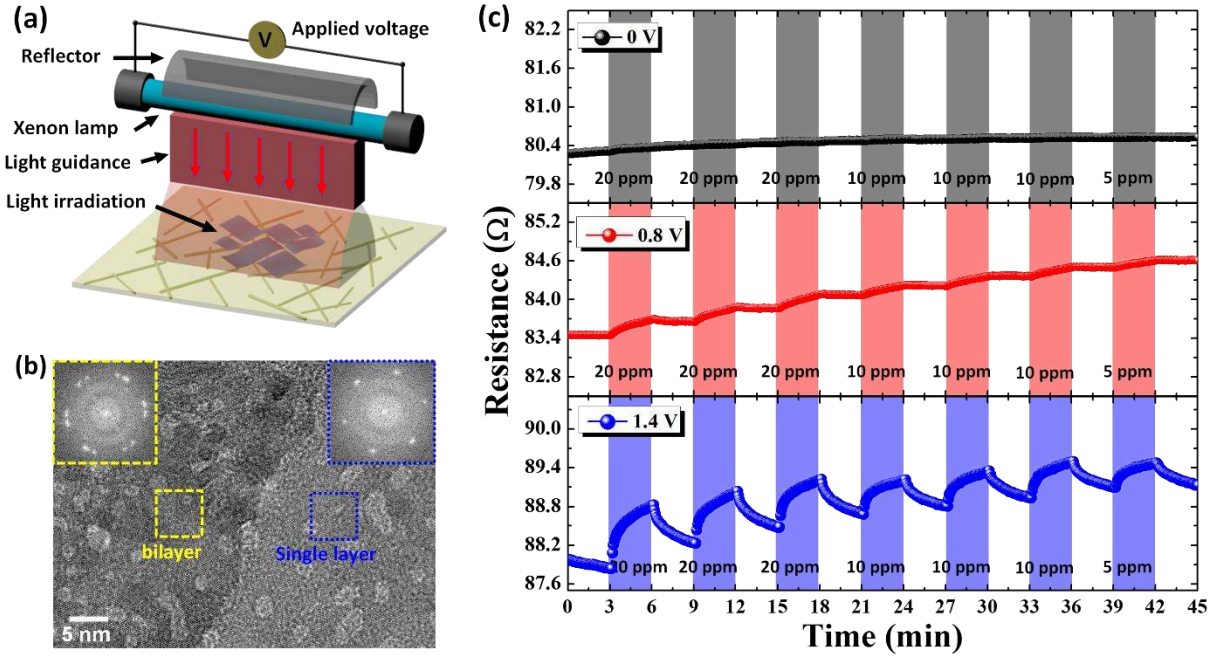

Figure 10. (a) Schematic illustration of optical irradiation using intense pulsed light (IPL) to form porous Ru oxide on the Ag NWs embedded flexible substrate. (b) TEM analysis of the porous Ru oxide nanosheets with FFT diffraction patterns in the inset. (c) Dynamic resistance changes of the porous Ru oxide nanosheets at different operating temperatures, i.e., 0 V (room temperature), 0.8 V (41.9 °C), and 1.4 V (80.3 °C), toward NO_2 in flat state. Reprinted with permission from Ref. [163] Copyright (2017), Wiley.

Choi *et al*. demonstrated RuO_2 nanosheet-based wearable chemical sensors to detect NO_2

for environmental air quality monitoring.[163] A patch-type wearable sensing module was developed for wireless transmission of sensing data to a smartphone (**Figure 11a**). Porous RuO_2 nanosheets on the Ag NW-embedded cPI substrate were integrated on the wearable sensing module. The operating temperature of the porous RuO_2 nanosheets was controlled by applying voltage to the Ag NW-embedded cPI heating film (Figure 11b). Improved sensing property toward 20 ppm of NO_2 was observed at 1.4 V compared to the operation at 0 V (room temperature) toward 20 ppm of NO_2 (Figure 11c).

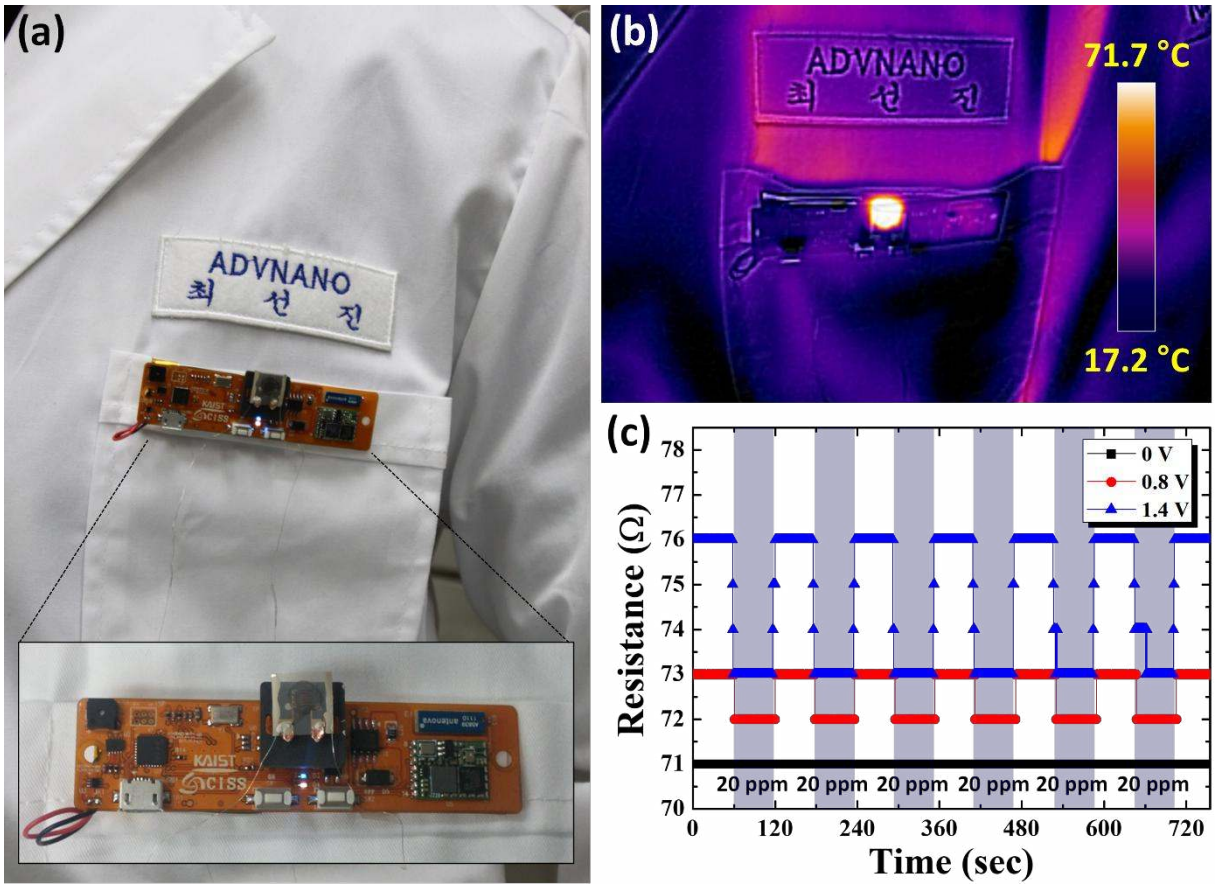

Figure 11. (a) Wearable sensing platform using the porous Ru oxide sensing layer on Ag NWs embedded cPI film. (b) Infrared image of Ru oxide sensing layer during operation. (c) Dynamic sensing property under cyclic exposure of Ru oxide sensing layer to 20 ppm of NO_2 measured by the wearable sensing platform at different operating voltages. Reprinted with permission from Ref.[163] Copyright (2017), Wiley.

Functionalization of 2D sensing materials with NPs such as Pt,[164, 165] Pd,[166] Au,[167] and intermetallic components[168, 169] have been demonstrated for further improvement of sensitivity and selectivity. In this regard, composite nanostructures with metal oxide nanosheets have been intensively studied with simultaneously engineering of microstructure and surface morphologies. Masuda *et al*. investigated 1-nonanal gas sensing performance by combining SnO_2 nanosheets with SnO_2 NPs and noble metallic Pd NPs for application in diagnosis of lung cancer.[170] The composite structure was prepared by coating a paste containing SnO_2 NPs and catalytic Pd NPs onto a substrate. After drying and subsequent heat treatment, the top surface of the composite film was covered with SnO_2 nanosheets. The sensitivity [R_a/R_g] of the composite nanosheets toward 1–10 ppm of 1-nonanal at 300 °C was up to 1.12-fold higher than that of pristine SnO_2 NPs, and the recovery ratio toward 1 ppm of 1-nonanal was 80.4%. Heterogeneous composite structure of In_2O_3 nanosheets decorated with tungsten oxide (WO_x) clusters was also demonstrated for HCHO detection.[171] The composite structure was synthesized by impregnation method, wherein ammonium tungstate hydrate was added into a suspension of indium glycerolate in ethanol. Subsequently, WO_x decorated In_2O_3 nanosheets were formed after calcination of the precursors at 400 °C for 3 h in air. The In_2O_3 nanosheets decorated with 4 wt% WO_x exhibited high sensitivity [R_{air}/R_{gas}] of 25 to100 ppm of HCHO with short response time (1 sec) and low LOD of 0.1 ppm at 170 °C. In addition, multi-compositional doping of ZnO nanosheets with Sn-Rh has been attempted for improved gas sensing property toward ethanol.[172] Very high sensitivity [R_{air}/R_{gas}] of 149.38 toward 100 ppm of ethanol was observed at 300 °C with fast response (3 sec) and recovery (10 sec) times. Hierarchical structure combining 2D layered nanosheets on 3D scaffold can further increase gas sensing property by facilitating surface reaction and gas penetration. In this regard, several studies have been demonstrated by forming metal oxide nanosheets on a nanofibrous 3D scaffold. For example, TiO_2 and Fe_2O_3 nanosheets were grown on the surface of

polyaniline nanofibers by hydrothermal process for detection of NH_3.[173, 174] Recently, Jang *et al*. synthesized WO_3 nanosheets on SnO_2 nanofiber networks by forming heterojunction structure for application in H_2S sensors. Electrospinning technique was employed for synthesis of the fibrous structure using composite solution of Sn precursor, W precursor, and a polymer scaffold. The WO_3 nanosheets were formed due to the preferential growth in planar structure of hexagonal $Sn[W_3O_9]$ upon thermal reduction at 400 °C for 3 h in reducing ambient (N_2), and subsequent calcination at 400 °C for 1 h in air ambient. The response [R_{air}/R_{gas}] of 1.02 to 5 ppm of H_2S was observed at room temperature in highly humid (95% RH) ambient, which displays its potential application in diagnosis of halitosis.[169]

Combination of heterogeneous nanostructures with diverse 2D metal oxide nanosheets is potential research strategy to obtain unique sensing properties with high sensitivity and selectivity. In particular, metal oxide nanosheets assembled on different 3D morphologies are gaining continuous interests for gas sensing application to maximize surface area and porosity for effective surface reactions. In addition, diverse metallic catalysts decorated on the surface of metal oxide nanosheets can further enhance gas sensing properties.

Table 3. Recent studies for chemical sensors using 2D metal oxide nanosheets and composites.

Material	Sensing type	Response definition	Sensitivity (Response)	Detection limit	Testing ambient	Target gas	Selectivity	Response / recovery time	Operating temperature	Ref.
ZnO nanosheets	Resistance change	R_{air}/R_{gas}	11.2 @ 100 ppm	5 ppm	Dry air	CO	SO_2, NH_3, H_2, NO_2, Cl_2, $C_6H_5CH_3$	25 sec/ 36 sec	300 °C	[146]
Porous ZnO nanosheets	Resistance change	R_{air}/R_{gas}	83.6 @ 50 ppm	1 ppm	Air	C_2H_5OH	NH_3, CH_3OH, HCHO, CO, H_2, NO_x	15 sec/ 12 sec	330 °C	[147]
Mesoporous ZnO nanosheets	Resistance change	R_{air}/R_{gas}	101.1 @ 100 ppm	1 ppm	Air	C_2H_2	C_6H_6, $C_6H_5CH_3$, CH_2Cl_2, $CHCl_3$, CCl_4, CH_4, H_2, CO	11 sec/5 sec	400 °C	[148]
SnO_2 nanosheets	Resistance change	R_{air}/R_{gas}	39.6 @ 100 ppm	5 ppm	Dry air	C_2H_5OH	CO_2, H_2, C_2H_4, H_2S, C_3H_6O	1 sec/ 9 sec	300 °C	[150]
SnO_2 nanosheets	Resistance change	R_{air}/R_{gas}	~70 @ 100 ppm	100 ppm	Air	CO	-	9 sec/ 18 sec	300 °C	[151]
WO_3 nanosheets	Resistance change	R_{gas}/R_{air}	5.67 @ 50 ppb	5 ppb	Air	NO_2	C_2H_5OH, CO, CO_2, H_2, NH_3	140 sec/ 75 sec	140 °C	[152]
CuO nanosheets	Resistance change	R_{gas}/R_{air}	8.933 @ 100 ppm	10 ppm	Air	C_2H_5OH	CH_3COCH_3, CH_3OH	15 sec/ 11 sec	370 °C	[153]
Co_3O_4 nanosheets	Resistance change	R_{gas}/R_{air}	9 @ 100 ppm	0.2 ppm	Dry air	NH_3	H_2S, H_2, CO, C_2H_5OH	9 sec/ 134 sec	Room temp.	[154]
ZnO nanosheets	Resistance change	R_{air}/R_{gas}	106.1 @ 200 ppm	810 ppm^{+}	Air	CH_3COCH_3	HCHO, C_2H_5OH, C_6H_6, $C_6H_5CH_3$, $(CH_3)_2C_6H_4$, CH_3NH_2	18.71 sec/ 13.75 sec	300 °C	[155]

ZnO nanosheets	Resistance change	$\Delta R/R_{gas}$ (%)	75–77% @ 1 ppm	50 ppb	Air	HCHO, CH_3CHO	-	10 sec/ 62 sec	220 °C	[156]
NiO porous nanowall	Resistance change	R_{gas}/R_{air}	12.9 @ 10 ppm	1 ppb	Air	H_2S	HCHO, C_6H_5Cl, CO, C_2H_5OH, CH_3COCH_3, NH_3, $(C_2H_5)_3N$	100 sec/ 79 sec	92 °C	[157]
Co_3O_4 nanosheets	Resistance change	R_{gas}/R_{air}	14.3 @ 100 ppm	10 ppm	Humid air (50–60%)	C_2H_5OH	CH_4, HCHO, C_6H_6, NH_3	-/-	160 °C	[158]
In_2O_3 Nanosheets	Resistance change	R_{gas}/R_{air}	213 @ 10 ppm	10 ppb	Air	NO_x	-	4 sec/ 9 sec	120 °C	[159]
$V_2O_5 \cdot 0.76$ H_2O nanosheets	Resistance change	$\Delta R/R_0$ (%)	2% @ 10 ppm	10 ppm	Air	H_2	-	-/-	250 °C	[162]
RuO_2 nanosheets	Resistance change	$\Delta R/R_0$ (%)	1.124% @ 20 ppm	5 ppm	Dry air	NO_2	H_2, CO, $C_6H_5CH_3$, CH_3COCH_3, NO	-/-	80.3 °C	[163]
4 wt% WO_x/In_2O_3 nanosheets	Resistance change	R_{air}/R_{gas}	25 @ 100 ppm	100 ppb	Air	HCHO	NH_3, C_6H_6, $C_6H_5CH_3$, NO_x, $(CH_3)_2C_6H_4$,	1 sec/ 67 sec	170 °C	[171]
Sn-Rh-doped ZnO nanosheets	Resistance change	R_{air}/R_{gas}	14938 @ 100 ppm	5 ppm	Air	C_2H_5OH	NH_3, C_6H_6, $C_6H_5CH_3$, CH_3OH, CH_2O	3 sec/ 10 sec	300 °C	[172]
WO_3 nanosheets	Resistance change	$\Delta R/R_0$ (%)	80% @ 1% (10000 ppm)	0.06% 600 ppm	Air	H_2	-	120 sec/ 235 sec	250 °C	[175]
NiO nanowalls	Resistance change	$\Delta R/R_0$ (%)	~650% @ 8 ppm	8 ppb	Dry air	HCHO	NO_2, NH_3, CH_4, CH_3COCH_3, H_2O, C_2H_5OH	120 sec/ 120 sec	150 °C	[176]

[+]Theoretical detection limit

3.4 Metal-organic frameworks (MOFs)

As an emerging 2D nanosheet structure, metal-organic frameworks (MOFs) are gaining much attention for application in gas sensors due to exceptionally large surface area and high porosity. MOFs are generally synthesized by controlled coordination of metal ions and organic ligands. The overall specific surface area of MOFs ranges from 1000 to 7000 m^2/g.[177] In addition, MOFs have versatile merits including well-defined pore structure and structural flexibility, which are advantageous for gas separation and vapor capture.[178, 179] Furthermore, functional MOFs for various applications can be easily synthesized by incorporating foreign nanostructures such as NPs, quantum dots, organic, and metalorganic molecules inside their structures.[179] **Table 4** presents recent progresses of 2D MOFs and MOF-assisted nanostructures for chemiresistive-type sensors.

As a promising 2D MOF structure, Cu(II) and Ni(II) ions were incorporated with highly conjugated tricatecholate, *i.e.*, 2,3,6,7,10,11-hexahydroxytriphenylene ($H_{12}C_{18}O_6$, HHTP), to form porous 2D frameworks, named metal-catecholates (M-CATs).[180] The M-CATs exhibited high chemical stability, thermal stability, and porosity. In particular, Cu-CAT-1 exhibited high electrical conductivity and charge storage capacity. In addition, Kambe *et al*. synthesized π-conjugated nanosheet composed of planar nickel bis(dithiolene) complex nanosheets by bottom up method.[181] Single layer nanosheet with thickness of 0.6 nm was achieved with π-conjugated nickel bis-(dithiolene) showing hexagonal structure. Furthermore, Sheberla *et al*. investigated high electrical property of 2D MOF composed of Ni_3(2,3,6,7,10,11-hexaiminotriphenylene)$_2$ with a thickness of approximately 500 nm.[182] The 2D MOF deposited on a quartz substrate exhibited semiconducting property with an electrical conductivity of 40 S/cm at room temperature. The 2D MOF nanosheets have been employed in gas separation owing to the well-defined pores and cavities similar to molecular dimensions. Rodenas *et al*. incorporated copper 1,4-benzenedicarboxylate MOF nanosheets in

a polymeric matrix, and utilized the resulted composite for molecular separation of CO_2 in CO_2/CH_3 gas mixture.[183] 2D MOF nanosheets based on $[Cu_2(ndc)_2(dabco)]_n$ (ndc = 1,4-naphthalene dicarboxylate; dabco = 1,4-diazabicyclo[2.2.2]-octane) have also been reported to exhibit higher CO_2 uptakes than nanorods based on the same MOFs.[184] Recently, ultrathin MOF nanosheets of $[Zn_2(benzimidazole)_3(OH)(H_2O)]_n$ with sub-10 nm thickness were prepared by exfoliation of layered MOF material and investigated for H_2/CO_2 gas separation.[185]

The first successful demonstration of 2D MOF nanosheets for gas sensors was performed using $Cu_3(HITP)_2$ (HITP=2,3,6,7,10,11-hexaiminotriphenylene).[186] The synthesis of $Cu_3(HITP)_2$ was achieved by rapid precipitation after reaction of $CuSO_4$ in dilute aqueous ammonia solution with 2,3,6,7,10,11-hexaaminotriphenylene hexahydrochloride (HATP·6HCl) at 23 °C in ambient atmosphere. After washing and drying, the 2D $Cu_3(HITP)_2$ exhibited bulk conductivity of 0.2 S/cm at room temperature. Reversible NH_3 sensing property was observed in the concentration range of 0.5–10 ppm with increasing current transitions under NH_3 ambient. Similarly, Campbell *et al*. developed conductive 2D MOF array to discriminate different categories of VOCs such as alcohols, aromatics, ketones/ethers, amines, and aliphatic hydrocarbons.[187] The 2D MOF structures were composed of different ligands such as 2,3,6,7,10,11-hexahydroxytriphenylene (HHTP) and 2,3,6,7,10,11-hexaiminotriphenylene (HITP) with metal centers of Cu or Ni (**Figure 12a**). A sensor array based on structurally analogous 2D MOFs namely $Cu_3(HHTP)_2$ (**1**), $Cu_3(HITP)_2$ (**2**), and $Ni_3(HITP)_2$ (**3**) were prepared by either drop-coating or a solvent-free mechanical drawing of the sensing materials onto substrates patterned with Au electrodes (Figure 12b). The 2D MOF-based sensor array exhibited characteristic sensing properties toward various VOCs (Figure 12c). Specifically, Cu-based MOFs showed similar trends in sensing behaviors with varying degree of response ($\Delta G/G_0$). In contrast, $Ni_3(HITP)_2$ (**3**) exhibited an opposite trend to the sensing behaviors of

the Cu-based MOFs. Generally, the 2D MOF array (**1-3**) are responsive toward polar VOCs with minor responses toward aliphatic hydrocarbons. Diverse sensing arrays are advantageous to recognize and classify gas species with different chemical properties by pattern recognition. The different sensing properties of 2D MOF array could clearly classify and yield groupings of different categories of VOCs.

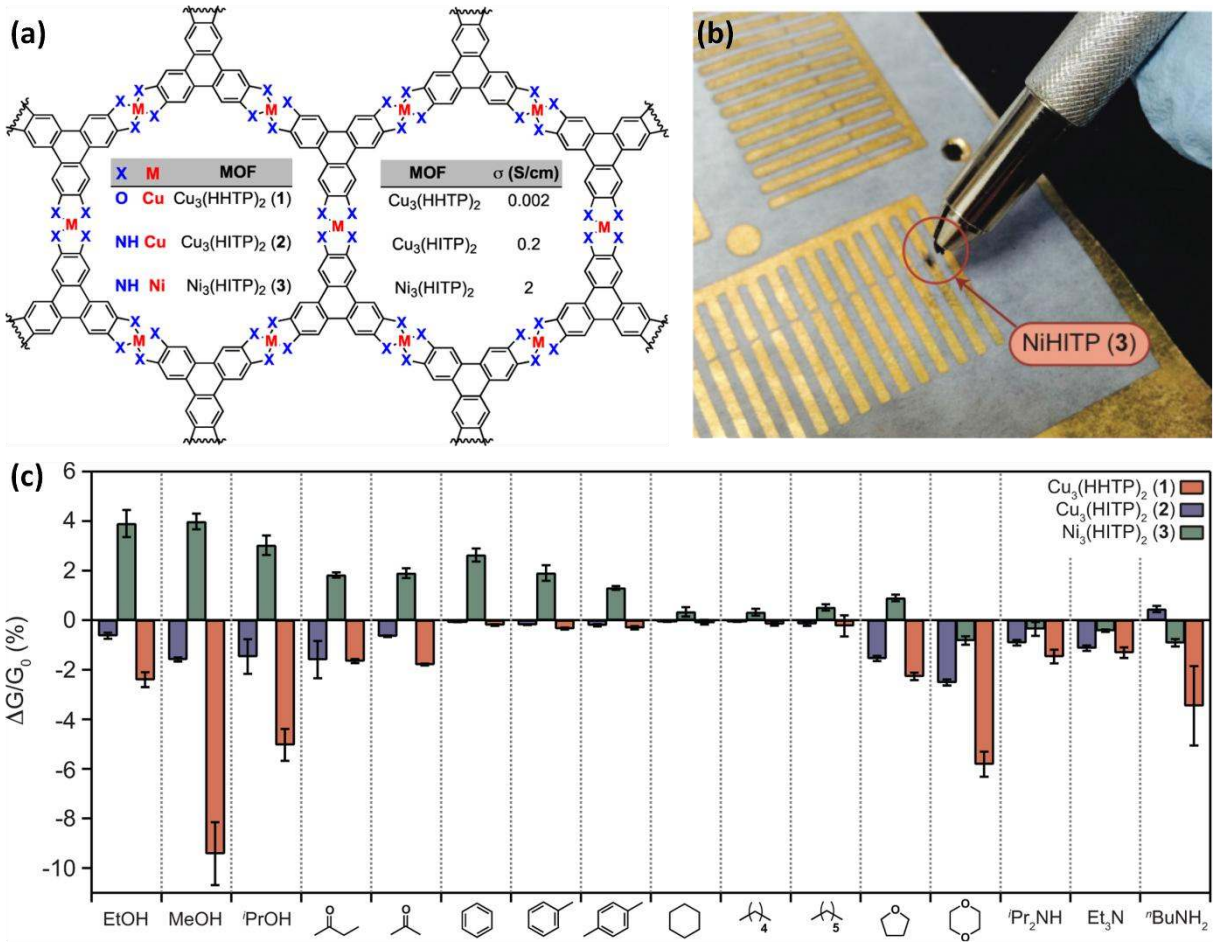

Figure 12. (a) Schematic chemical structure of electrically conductive 2D MOF. (b) Coating of 2D MOF sensing material on a paper substrate with Au electrodes by mechanical drawing technique. (c) Sensing property of 2D MOF-based sensing array toward diverse VOCs. Reprinted with permission from Ref.[187] Copyright (2015), American Chemical Society.

Beside pure MOF-based gas sensors, incorporation of metal and metal oxide NPs with MOFs has been attempted for application in gas separation, catalysts, and gas sensing.[188]

Composite MOF-based nanomaterials can take additional advantages in terms of material diversity with various electrical and chemical properties including high surface area and porosity. Recently, MOFs have been incorporated into different dimensional structures as sacrificial templates to form heterogenous composites.[189-192] The first attempt to form heterogeneous MOF-driven metal@metal oxide complex catalysts on 1D fibrous metal oxide nanofibers was demonstrated by Koo *et al.*[189] Pd-embedded zeolite imidazole frameworks (ZIF-8) were prepared and employed as sacrificial templates. Subsequently, these templates were dispersed in electrospinning solution to form MOF-decorated 1D polymer/W precursor composites nanofibers. Finally, 1D heterogeneous WO_3 nanofibers functionalized with Pd-ZnO catalysts were achieved after calcination at 500 °C for 1 h. The obtained Pd-ZnO decorated WO_3 nanofibers exhibited selective detection toward 1 ppm of toluene with a sensitivity (R_{air}/R_{gas}) of 22.22. The superior sensitivity of MOF-derived composite sensor was achieved at operating temperature of 350 °C. Similarly, MOF-derived nanotubular composite of PdO-ZnO catalyst-decorated SnO_2 nanotubes has been demonstrated by electrospinning to facilitate high surface area and porosity.[190] The MOF-derived SnO_2 nanotubes exhibited improved response (R_{air}/R_{gas}) of 5.06 toward 1 ppm of acetone at 400 °C with fast response (20 sec) and recovery (64 sec) times. Furthermore, various porous nanostructures including PdO-decorated Co_3O_4 hollow nanocages and Pd-decorated ZnO/$ZnCo_2O_4$ hollow spheres were synthesized from Co and Zn-based ZIFs for detection of acetone at high humidity.[191, 192] In particular, MOF-derived porous SnO_2 hollow polyhedron structures were firstly demonstrated by galvanic replacement of Co_3O_4 hollow cubes prepared from Co-based ZIF-67.[193] The *n*-type SnO_2 hollow cubes exhibited 29.1-fold improved acetone response (R_{air}/R_{gas} = 22.8 at 5 ppm) compared to the MOF-derived *p*-type Co_3O_4 hollow cubes without galvanic replacement. Although the templating strategies using MOF nanomaterials have not been tried on 2D layered nanosheets, one can expect that development of diverse 2D MOF

nanosheets as effective sacrificial templates can provide further enhanced gas sensing performance of 2D MOF-based sensing materials.

Table 4. Recent publications of 2D MOFs and MOF-assisted nanostructures for chemiresistive-type sensors

Material	Sensing type	Response definition	Sensitivity (Response)	Detection limit	Testing ambient	Target gas	Selectivity	Response /recovery time	Operating temperature	Ref.
$Cu_3(HITP)_2$	Conductivity change	$\Delta G/G_0$ (%)	~3.5% @ 10 ppm	0.5 ppm	N_2	NH_3	H_2O	30 sec/ 300 sec	Room temp.	[186]
$Cu_3(HHTP)_2$	Conductivity change	$\Delta G/G_0$ (%)	~10% @ 200 ppm	-	N_2	CH_3OH	Aromatics, aliphatic hydrocarbons	30 sec/ -	Room temp.	[187]
$Ni_3(HITP)_2$	Conductivity change	$\Delta G/G_0$ (%)	~4% @ 200 ppm	-	N_2	C_2H_5OH	Amines, aliphatic, ethers	30 sec/ -	Room temp.	[187]
ZIF-8-derived Pd-ZnO nanocubes	Resistance change	R_{air}/R_{gas}	22.22 @ 1 ppm	100 ppb	Humid air (95% RH)	$C_6H_5CH_3$	CH_3COCH_3, NH_3, H_2S, C_2H_5OH, NO	20 sec/ -	350 °C	[189]
ZIF-8-derived PdO-ZnO-SnO_2 nanotubes	Resistance change	R_{air}/R_{gas}	5.06 @ 1 ppm	100 ppb	Humid air (95% RH)	CH_3COCH_3	NH_3, H_2S, CO, C_5H_{12}, C_2H_5OH, $C_6H_5CH_3$	20 sec/ 64 sec	400 °C	[190]
ZIF-67-derived PdO-Co_3O_4 HNCs	Resistance change	R_{gas}/R_{air}	2.51 @ 5 ppm	400 ppb	Humid air (90% RH)	CH_3COCH_3	NH_3, H_2S, CO, C_5H_{12}, C_2H_5OH, $C_6H_5CH_3$	-/-	350 °C	[191]
Pd-ZnO/$ZnCo_2O_4$ HSs	Resistance change	$\Delta R/R_0$ (%)	69% @ 5 ppm	0.4 ppm	Humid air (90% RH)	CH_3COCH_3	NH_3, H_2S, CO, NO_2, H_2, C_5H_{12}, C_2H_5OH, $C_6H_5CH_3$	-/-	250 °C	[192]
ZIF-67-derived Co_3O_4-PdO-SnO_2 HNCs	Resistance change	R_{air}/R_{gas}	22.8 @ 5 ppm	5 ppb[+]	Humid air (90% RH)	CH_3COCH_3	NH_3, H_2S, CO, CH_3SH, C_5H_{12}, C_2H_5OH, $C_6H_5CH_3$	90.8 sec/ 108.4 sec	450 °C	[193]

[+]Theoretical detection limit, HITP=2,3,6,7,10,11-hexaiminotriphenylene, HHTP=2,3,6,7,10,11-hexahydroxytriphenylene, ZIF-8=Zn-based zeolite imidazole frameworks, ZIF-67=Co based zeolite imidazole framework, HNCs=hollow nanocubes, HSs=hollow spheres, BM-ZIFs=zinc and cobalt based zeolite imidazole frameworks

3.5 Black phosphorus

Since 2014, black phosphorus (BP) has suddenly gained tremendous attention due to the discovery of phosphorene, which is atomically thin two-dimensional variant of BP with good carrier mobility and structural properties. BP has orthorhombic crystal structure consisting of puckered hexagonal domains. Each atom in BP is connected to three neighboring atoms forming sp^3 hybridization.[194] BP possesses direct band gap approximately 1.5–2 eV for the monolayer, and 0.3 eV for bulk structure with *p*-type semiconductor property, which has triggered broad applications in electronics and optoelectronics.[195] Among various synthesis methods, top down exfoliation technique from bulk crystal has been generally performed to obtain layered BP nanosheets with uniform size and in large quantities.

Recently, Cui *et al*. investigated layer-dependent gas sensing performance of BP nanosheets toward NO_2 at room temperature.[196] In their study, BP nanosheets with different thickness were prepared by mechanical exfoliation technique using Scotch tape. Subsequently, the BP nanosheets were deposited on a silicon substrate with 300 nm-thick oxide layer. Transmission electron microscopy (TEM) analysis revealed the single crystalline BP nanosheets with orthorhombic structure (**Figure 13a**). The gas sensing property of FET-based BP nanosheets sensor was evaluated by injection of NO_2 in dry air ambient at room temperature. The dynamic conductivity transitions of 4.8 nm-thick BP nanosheets sensor revealed p-type sensing property upon injection of 20–1000 ppb of NO_2. The response [$\Delta G/G_0$ (%)] of the 4.8 nm-thick BP nanosheets sensor to 20 ppb and 100 ppb of NO_2 was up to 190% and 1600%, respectively (Figure 13b). Upon exposure of the sensors to 500 ppb of NO_2, the response of the 4.8 nm-thick BP nanosheets sensor was even higher than that of BP bulk sensor. However, a significant decrease in response was observed when the thickness was decreased further, demonstrating that the response of BP nanosheets was significantly dependent on the layer thickness. The BP nanosheets exhibited selective NO_2 detection property with minor

responses toward interfering analytes such as CO, H_2, and H_2S. To investigate the sensing mechanism, DFT calculations were performed, and the adsorption density of NO_2 on BP nanosheets was revealed to be higher compared to graphene nanosheets. However, several orders of magnitude smaller adsorption densities were observed toward CO, H_2, and H_2S. The thickness dependent NO_2 sensing property of BP nanosheets was attributed to the band gap energy dependence on thickness. Large band gap BP nanosheets show poor sensitivity due to the low concentration of charge carriers, thereby inducing lower density of adsorbed gas molecules. On the other hand, conductivity change is less obvious in the case of low band gap energy of BP nanosheets due to high concentration of charge carriers. Mechanically exfoliated multilayered BP flakes were also investigated by integration with FET for detection of NO_2.[197] The thickness of BP flakes was approximately 55 nm with multilayered structure as confirmed by AFM (Figure 13c). The FET-based BP flakes exhibited high sensitivity [$\Delta G/G_0$ (%)] of 2.9% toward 5 ppb of NO_2 (Figure 13d). Increasing conductivity toward NO_2 was observed for the BP flakes due to the electron withdrawing property of NO_2 from *p*-type BP flakes.

Liquid phase exfoliation technique is advantageous to obtain stable BP suspension. Hanlon *et al*. prepared 2D BP nanosheets suspension by exfoliation of BP crystals followed by dispersion of the nanosheets in *N*-cyclohexyl-2-pyrrolidone (CHP).[195] The BP nanosheets were very stable in CHP solution due to the protection by solvation shell preventing reaction with oxygen and water. The BP nanosheets obtained by liquid exfoliation exhibited lateral dimension around 1 μm without defect (inset of Figure 13e). Gas sensing behavior toward NH_3 was investigated using the BP nanosheets with the conductivity of approximately 1 S/m (Figure 13e). Increasing resistance transition was observed with respect to NH_3 concentrations due to the *p*-type sensing property of BP nanosheets and electron donating property of NH_3. The estimated LOD was 80 ppb calculated by signal to noise ratio. Recently, Cho *et al*.

investigated comparative sensing property of BP flakes with other 2D nanosheets such as graphene and MoS_2 flakes.[198] All the 2D flakes showed similar lateral size distribution around 400 nm. BP flakes exhibited better sensitivity with high response [$\Delta R/R_0$ (%)] of proximately 80% toward 1 ppm of NO_2 at room temperature, which was up to 20 times higher compared to that of graphene and MoS_2 flakes. In addition, the BP flakes presented high selectivity toward NO_2 with negligible response to interfering chemical species including H_2, acetone, acetyl aldehyde (CH_3CHO), ethanol, toluene, and hexane (C_6H_{14}). DFT simulation analysis suggested that the selectivity toward NO_2 was mainly attributed to the higher adsorption energy of BP flakes than those of graphene and MoS_2 flakes.

Instability of BP in humid ambient has been a major issue in many applications. However, facile reaction of BP with humidity is advantageous for its application in humidity sensors. Recently, several studies demonstrated the exceptionally sensitive humidity sensors using layered BP flakes.[199-201] Yasaei *et al*. investigated humidity sensing property of BP flakes in the form of multilayered film with thickness of 26 μm. A four-order of magnitude enhanced current was observed in humidity levels of 10–85%, and the sensor was stable up to 3 months. In addition, atomically thin BP nanosheets with the thickness of 1.4 nm were prepared by electrochemical exfoliation method.[200] The BP nanosheets exhibited high sensitivity [(R_{Dry}-R_{Humid})/R_{Humid} (%)] of ~521% at 97% Rh. BP nanosheets of different sizes were obtained upon centrifugation of liquid exfoliated sample at different centrifuged speeds, and then their humidity sensing property was investigated.[201] The result revealed that BP nanosheets with smaller lateral dimension (10–200 nm) and thickness (~3 nm) exhibited improved humidity sensitivity [(R_{Humid}-R_{N2}) R_{N2} (%)] of 99.17% at 97.3% RH than large and thick BP nanosheets. In order to obtain enhanced stability of BP nanosheets toward humidity sensing property, Miao *et al*. proposed very thin Al_2O_3 layer for encapsulation of BP nanosheets.[202] Atomic layer deposition (ALD) was utilized to form 6 nm-thick Al_2O_3 encapsulation layer on BP

nanosheets. As a result, the BP nanosheets exhibited long-term stability with minor degradation in response even after exposure in air for over a week.

As a futuristic strategy, BP nanosheets functionalized by noble metals have been demonstrated as an effective gas sensing layer. Cho *et al.* developed heterostructure by incorporating Pt NPs on BP nanosheets for improved H_2 sensing property.[203] The exfoliated BP nanosheets were incorporated with Pt precursor ($PtCl_4$) at an elevated temperature (60 °C) for 12 h. TEM analysis confirmed the densely distributed Pt NPs with the diameter distribution range of 1–5 nm on BP nanosheets (Figure 13f). High-resolution TEM images confirmed crystalline structures of Pt (111) and BP nanosheets (012). Gas sensing characteristic was evaluated at room temperature in N_2 ambient toward H_2, NO_2, acetone, ethanol, hexane, toluene, and acetaldehyde. For the pristine BP nanosheets, significantly high response toward NO_2 was observed with minor responses toward interfering analytes. On the other hand, highly sensitive and selective response [$\Delta R/R_0$ (%)] property of BP nanosheets after incorporation of Pt NPs was up to 500% at 1% H_2 (Figure 13g). The improved H_2 sensing property of BP nanosheets was explained by activated charge transfer from Pt to BP nanosheets due to decreased work function of Pt after adsorption of H atom. In addition, the Pt incorporated BP nanosheets exhibited high stability in ambient condition (～23 °C and ～35% RH) with consistent H_2 response, which was mainly attributed to the blocking of lone pair electrons on BP surfaces by Pt NPs that prevented reactions with oxygen and water.[204]

Beside sensing application, the layered 2D BP with unique electronic property have been applied for photodetector,[205] memory device,[206] and energy conversion device.[207] Nevertheless, lack of environmental stability due to the undesirable reactions with oxygen and water should be addressed to obtain reliable material property and device performance.

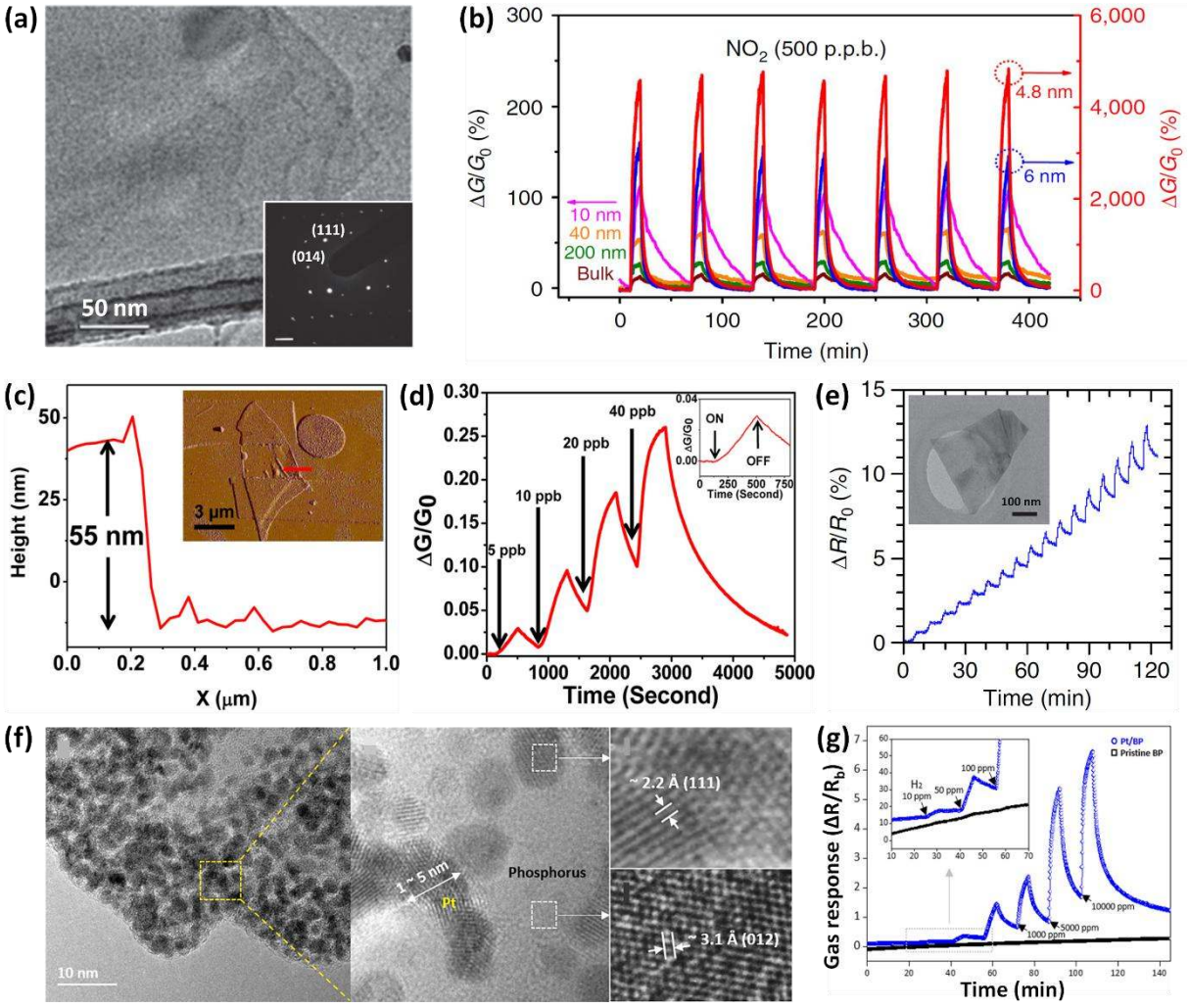

Figure 13. (a) TEM image of BP nanosheets with selected area electron diffraction (SAED) pattern in the inset. (b) Dynamic response [$\Delta G/G_0$ (%)] transitions with respect to the thickness of BP nanosheets toward 500 ppb NO_2 at room temperature. Reprinted with permission from Ref.[196] Copyright (2015), Nature Publishing Group. (c) Height profile and amplitude image of BP flakes using atomic force microscopy (AFM). (d) Dynamic sensitivity [$\Delta G/G_0$] transitions of FET-based BP flake sensor toward NO_2 in the concentration range of 5–40 ppb. Reprinted with permission from Ref.[197] Copyright (2015), American Chemical Society. (e) Dynamic response [$\Delta R/R_0$ (%)] of BP nanosheets toward NH_3 in the concentration range of 1–10 ppm at room temperature and TEM image of BP nanosheets in the inset. Reprinted with permission from Ref.[195] Copyright (2015), Nature Publishing Group. (f) TEM analysis of Pt-incorporated BP nanosheets. (g) Dynamic gas response [$\Delta R/R_0$] of pristine BP and Pt-incorporated BP nanosheets toward H_2 in the concentration range of 10–10000 ppm at room temperature. Reprinted with permission from Ref.[203] Copyright (2017), American Chemical Society.

Table 5. Recent publications of 2D phosphorus nanosheets for chemiresistive-type sensors.

Material	Sensing type	Response definition	Sensitivity (Response)	Detection limit	Testing ambient	Target gas	Selectivity	Response / recovery time	Operating temperature	Ref.
Black phosphorus nanosheets	Resistance change	$\Delta R/R_0$ (%)	~13% @ 10 ppm	80 ppb$^+$	N_2	NH_3	-	-/-	Room temp.	[195]
Phosphorene nanosheets (4.8 nm thick)	Conductivity change	$\Delta G/G_0$ (%)	1600% @ 1000 ppb	20 ppb	Dry air	NO_2	CO, H_2S, H_2	-/-	Room temp.	[196]
Black phosphorus (55 nm thick)	Conductivity change	$\Delta G/G_0$ (%)	2.9% @ 5 ppb	5 ppb	Ar	NO_2	-	~840 sec/ ~840 sec	Room temp.	[197]
Black phosphorus	Resistance change	$\Delta R/R_0$ (%)	80% @ 1 ppm	0.1 ppm	N_2	NO_2	H_2, CH_3COCH_3, CH_3CHO, C_2H_5OH, $C_6H_5CH_3$, C_6H_{14}	70 sec/-	Room temp.	[198]
Black phosphorus nanosheets	Resistance change	$(R_{Dry}-R_{Humid})/R_{Humid}$ (%)	~521% @ 97% RH	32% RH	Dry air (32% RH)	Humidity	-	101 sec/ 26 sec	Room temp.	[200]
Black phosphorus nanosheets	Resistance change	$(R_{Humid}-R_{N2})/R_{N2}$ (%)	99.17% @ 97.3% RH	11.3% RH	N_2	Humidity	-	255 sec/ 10 sec	Room temp.	[201]
Black phosphorus nanosheets	Conductivity change	$\Delta G/G_0$ (%)	~40% @ 60% RH	60% RH	Ar (21% RH)	Humidity	-		Room temp.	[202]
Black phosphorus-Pt NPs	Resistance change	$\Delta R/R_0$ (%)	500% @ 10000 ppm (1%)	10 ppm	N_2	H_2	NO_2, CH_3COCH_3, CH_3CHO, C_2H_5OH, $C_6H_5CH_3$, C_6H_{14}	-/-	Room temp.	[203]

[+]Theoretical detection limit.

3.6 MXene

MXenes are a new family of 2D layered nanomaterials based on transition metal carbides, nitrides, and carbonitrides. In general, Mxene can be prepared by selective etching of the A element from the MAX phase. The MAX phase is composed of $M_{n+1}AX_n$, in which M is transition metal, A is generally a group IIIA or IVA element, X is C and/or N with n = 1, 2, or 3.[208] It is estimated that over 60 different MAX phases have been invented including Ti_2AlC, V_2AlC, Ti_2AlN, Ti_3SiC_2, V_2PC, Ti_2SC, Ti_2GaC, Ti_2GeC, V_2AsC, Ti_2CdC, Ti_2InC, and Ti_2SnC.[209] In addition, MXene layered nanomaterials include Ti_3C_2, Ti_2C, V_2C, $(Ti_{0.5}, Nb_{0.5})_2C$, $(V_{0.5}, Cr_{0.5})_3C_2$, Ti_3CN, and Ta_4C_3.[210] The primary merit of MXenes is their tunable electronic properties by combination of various transition metals and changing their surface termination. Because of their high conductivity, Mxenes have been experimentally demonstrated as functional materials for energy storage applications[211] such as lithium ion batteries,[212] supercapacitors,[213] and fuel cells.[214] In addition, a recent review highlights applications of MXenes in various types of sensors.[215] Nevertheless, only few studies have reported on the gas sensing property of Mxenes.

A theoretical study of NH_3 sensing using Ti_2CO_2 as a MXene with oxygen termination group has been performed by first-principle simulation.[216] The Ti_2CO_2 nanosheets exhibited semiconducting property, unlike Ti_2C, Ti_2CF_2, and $Ti_2C(OH)_2$, which exhibited metallic conductivity.[217] Semiconducting property of Ti_2CO_2 nanosheets demonstrates its potential application in chemiresistive-type sensors. The theoretical study investigated the possible adsorption sites for various chemical molecules such as NH_3, H_2, CH_4, CO, CO_2, N_2, NO_2, and O_2 on the monolayer Ti_2CO_2 nanosheet. The results revealed that the strongest binding site was N atom directly above the Ti atom on the Ti_2CO_2 nanosheet with the adsorption energy of –0.37 eV, and a charge transfer of 0.174 e from NH_3 to the Ti_2CO_2 nanosheet. In contrast, the other chemical species exhibited minor interaction with the Ti_2CO_2 nanosheet

with negligible adsorption energy changes and charge transfers. The strong interaction of NH_3 with the Ti_2CO_2 nanosheet was mainly due to the deformation of local binding structure as well as charge transfer. As shown in **Figure 14a**, orbital mixing and charge transfer likely occurred due to the overlapping of electronic charge between NH_3 molecule and the Ti_2CO_2 nanosheet. The simulated current-voltage (I-V) curves revealed large current transitions toward NH_3 adsorption on the monolayer Ti_2CO_2 nanosheet with minor current changes toward other interfering molecules (Figure 14b). The results imply that monolayer Ti_2CO_2 nanosheet can be used for sensitive and selective detection of NH_3. In addition, the adsorption energy can be further decreased to –0.51 eV under 3% biaxial strain, which effectively facilitates NH_3 adsorption on the surface of Ti_2CO_2 nanosheet (Figure 14c).

Recently, experimental demonstration for NH_3 detection of MXene using titanium carbide was reported by Lee *et al.*[218] $Ti_3C_2T_x$ nanosheets were prepared by selective removal of Al atoms in Ti_3AlC_2 (MAX phase). The 2D $Ti_3C_2T_x$ nanosheets were formed with two layers of carbon atoms stacked between three layers of titanium atoms (Figure 14d). During the synthesis process, surface of $Ti_3C_2T_x$ nanosheets were randomly terminated with various functional groups such as −OH, −O, and −F. Cross-sectional SEM image revealed the stacked 2D layers of $Ti_3C_2T_x$ nanosheets (Figure 14e). Gas sensing property was investigated toward 100 ppm of chemical gases such as ethanol, methanol, acetone, and NH_3 at room temperature. In particular, $Ti_3C_2T_x$ nanosheets exhibited *p*-type sensing property, with large resistance change upon exposure to NH_3. The response $[(R_{gas}–R_{air})/R_{air}]$ of 0.21 was obtained toward NH_3 compared to lower responses toward other VOC species. The increasing resistance transitions were mainly due to electron transfer from the adsorbed gas to the $Ti_3C_2T_x$ nanosheets by the reaction with surface functional groups such as O^- and OH^-. The $Ti_3C_2T_x$ nanosheets were integrated on a flexible polyimide substrate for potential application in flexible chemical sensors. It is anticipated that MXenes will attract further investigations by

combination with different 2D nanostructures or functionalization of multi-dimenstional catalytic materials for improved gas sensing properties.

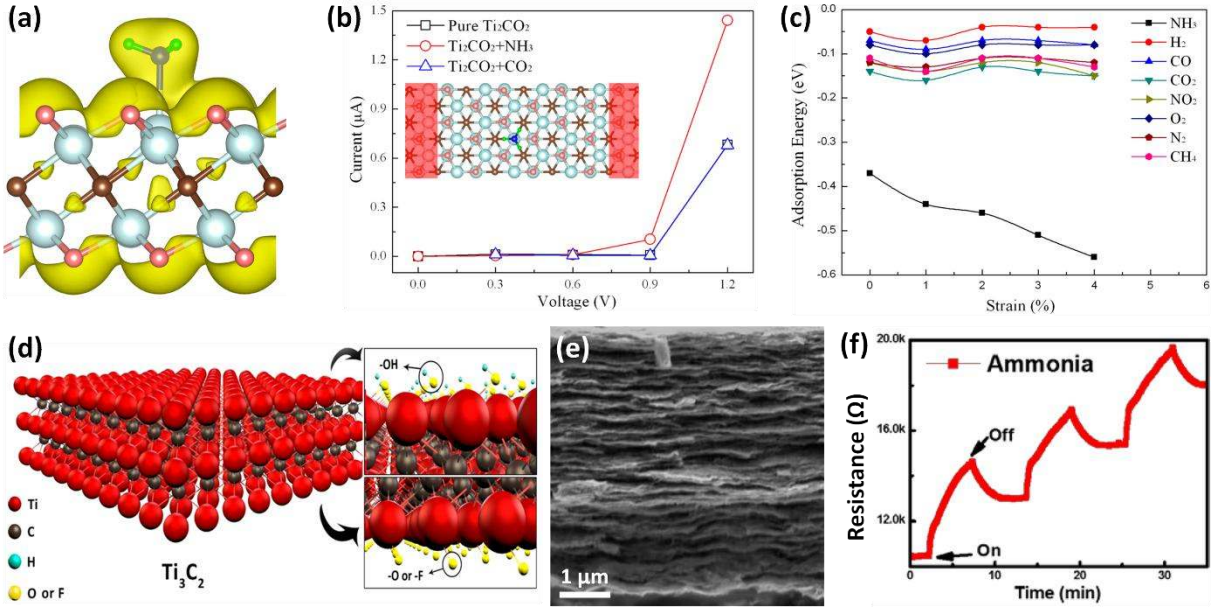

Figure 14. (a) Total charge density under NH_3 adsorption on monolayer Ti_2CO_2 nanosheet. (b) Current-voltage (I-V) characteristic of monolayer Ti_2CO_2 nanosheet before and after gas adsorption and schematic illustration of monolayer Ti_2CO_2 sensor in the inset. (c) Adsorption energies of various chemical molecules including NH_3, H_2, CH_4, CO, CO_2, N_2, NO_2, and O_2 on the monolayer Ti_2CO_2 nanosheet with respect to the applied biaxial strains in the range of 0–4%. Reprinted with permission from Ref.[216] Copyright (2015), American Chemical Society. (d) Schematic illustration of 2D $Ti_3C_2T_x$ nanosheets with various functional groups on the surface such as −OH, −O, and −F. (e) Cross-sectional SEM image of stacked $Ti_3C_2T_x$ nanosheets through vacuum filtration. (f) Dynamic resistance transitions of $Ti_3C_2T_x$ nanosheets toward 100 ppm of NH_3 at room temperature. Reprinted with permission from Ref.[218] Copyright (2017), American Chemical Society.

3.7 Emerging layered composites

Recently, heterogeneous junction formation has attracted much attention to form new types of 2D composites for improved sensing properties. Novel electrical and optical properties are generally achieved by combination of multi-layered nanosheets. A recent review empathized the importance of heterostructure composed of graphene and MoS_2 for applications in electrochemical energy storage, sensing, hydrogen generation, and FETs.[219] In addition,

comprehensive perspective of epitaxial growth for heterogeneous nanostructures using 2D nanosheets have been introduced to exploit unique *p-n* heterojunctions for optimization of chemical and electrical properties of nanosheets.[220]

Recently, several studies demonstrated the improved sensing properties of heterogeneous composites. Graphene and metal oxide nanosheets composites such as graphene/ZnO nanosheets,[221] RGO/NiO nanosheets,[222] and RGO/hexagonal WO_3 nanosheets[223] have been synthesized and evaluated for enhanced gas sensing application. The RGO/NiO nanosheets were prepared by forming RGO layer on a substrate followed by growing vertical NiO nanosheets on its surface.[222] The composite structure exhibited high sensitivity and selectivity toward NO_2 with 100-fold enhancement compared to pristine NiO nanosheets. In the case of RGO/hexagonal WO_3 nanosheets, hydrothermal method and subsequent calcination treatment were performed to form the composite structure.[223] The RGO/hexagonal WO_3 nanosheets exhibited the response [R_{air}/R_{gas}] of 168.58 at 330 °C toward 40 ppm of H_2S, which was 3.7-fold improved response compared to the response (45.86) of pristine WO_3 nanosheets. Chemical sensing property of graphene and TMD composites has also been investigated as a new type of heterostructure. Cho *et al.* developed unique hybrid structure comprising patterned graphene as a charge collector with MoS_2 flakes as a sensing layer (inset of **Figure 15a**).[224] In addition, the composite structure was successfully fabricated on a flexible polyimide film for application in flexible chemical sensors (Figure 15a). The MoS_2 flakes were prepared by mechanical exfoliation technique on a SiO_2/Si substrate. Subsequently, CVD-grown graphene layer was transferred onto the MoS_2 flakes after patterning using photolithography and reactive ion etching. The hybrid graphene/MoS_2 flakes exhibited high sensitivity [$\Delta R/R_{N2}$ (%)] of 6.83% toward 5 ppm of NO_2 at 150 °C (Figure 15b). The improved NO_2 sensing property was mainly attributed to the increased carrier concentration of the graphene/MoS_2 flakes. The hybrid composite exhibited

p-type sensing property with decreasing resistance upon exposure to NO_2. As a potential material for flexible sensors, its bending stability toward gas sensing was investigated. It was found that the response remained stable even after 5000 bending cycles (Figure 15c). Similar composition of MoS_2/graphene hybrid aerogel was synthesized for ultrasensitive NO_2 sensors.[225] Graphene aerogel scaffold was first prepared and subsequently MoS_2 nanosheets were coated on the surface of graphene aerogel by solution dipping followed by annealing. The hybrid MoS_2/graphene aerogel exhibited high porosity with average pore size of 6 nm as well as large surface area (700 m^2/g), which are advantageous for gas accessibility and surface reactions. Very thin monolayer of MoS_2 was covered around graphene aerogel forming three-dimensional structure. Fast response (21.6 sec) and stable recovery (within 29.4 sec) were achieved using the hybrid aerogel sensor at an elevated operating temperature (200 °C) even at very low NO_2 concentration (50 ppb). In addition, selective NO_2 detection was confirmed with minor responses toward interfering analytes such as H_2 and CO.

As an alloy junction hybrid structure, two different 2D TMD nanosheets of $NbSe_2/WSe_2$ were synthesized by one-step CVD method for improved gas sensing characteristic toward NO_2.[226] The hybrid $NbSe_2/WSe_2$ nanosheets were prepared by selenisation of prepatterned WO_3 and Nb_2O_5 using CVD system, thereby forming $NbSe_2$ (metallic layer)-$Nb_xW_{1-x}Se_2$ (transition layer)-WSe_2 (semiconducting layer) heterojunction (Figure 15d). Energy-dispersive spectroscopy (EDS) analysis confirmed the cross-sectional compositions of Nb and W, which revealed the interlayer structure of $Nb_xW_{1-x}Se_2$ (Figure 15e). Large resistance transitions were observed using $NbSe_2/WSe_2$ nanosheets with decreasing resistance upon exposure to 1.2–5 ppm of NO_2 with *p*-type sensing behavior (Figure 15f). The improved NO_2 sensing performance of $NbSe_2/WSe_2$ nanosheets was mainly attributed to a decrease of Schottky barrier height due to the interlayer alloy junction, thereby effectively transferring charge carriers induced by chemical reactions. Interestingly, $NbSe_2/WSe_2$ nanosheets were

integrated on PET film to demonstrate its performance as a flexible sensor (in the inset of Figure 15f). NO_2 sensing characteristic with the response [$(R_{gas}-R_{N2})/R_{N2}$ (%)] of 30% was maintained under bending stress up to 10000 bending cycles and bending radius of 5 mm. In addition, gas sensing property was maintained after conventional laundry process.

Another intriguing 2D hybrid structure, which is based on hexagonal boron nitride (h-BN), has been explored to modulate electrical property.[227] For example, unique electronic properties of heterostructures including BP/h-BN for tunneling TFTs,[228] h-BH/graphene nanosheets,[229] and WSe_2-hBN-graphene multi-layered structure for transparent TFTs[230] have been investigated. As evidenced by growing interests in heterogeneous structures, it is expected that gas sensing characteristics of various heterojunction nanosheets with engineered interlayer compositions will be actively investigated.

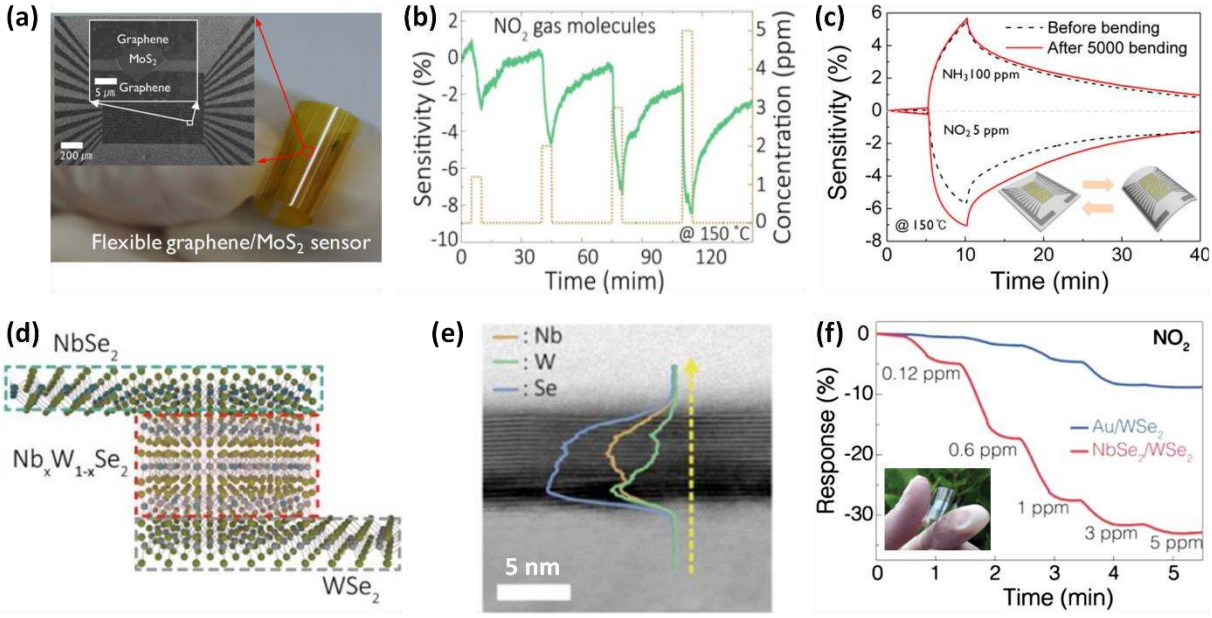

Figure 15. (a) Camera image of 2D heterostructure on a flexible substrate with SEM image of MoS_2 film on a patterned graphene film. (b) Dynamic sensitivity transition of the heterostructure toward NO_2 in the concentration range of 1.2–5 ppm. (c) Sensor response characteristic toward NH_3 and NO_2 before and after bending. Reprinted with permission from Ref.[224] Copyright (2015), American Chemical Society. (d) Schematic illustration of heterojunction structure of $NbSe_2$ (metallic layer)-$Nb_xW_{1-x}Se_2$ (transition layer)-WSe_2 (semiconducting layer). (e) Cross-sectional TEM image with X-ray EDS elemental analysis.

(f) Dynamic response transition of heterojunction structure of $NbSe_2/WSe_2$ and Au/WSe_2. Reprinted with permission from Ref.[226] Copyright (2016), American Chemical Society.

4. Summary and perspective

In this review, we comprehensively summarized the recent progresses on the 2D layered nanosheets for gas sensor applications. Diverse 2D nanomaterials such as graphene, TMDs, metal oxide, MOFs, phosphorus, MXenes, and their composites have been synthesized and their gas sensing properties have been investigated. We introduced various synthesis strategies to prepare 2D nanosheet structures and discussed their sensing performance mainly focusing on response (sensitivity), reaction speed, selectivity, and limit of detection.

As future perspectives, there are great opportunities on 2D nanosheet based materials as promising gas sensing materials. On material aspect, compositional modification is an attractive strategy to customize gas sensing properties. For example, chemical doping with foreign materials on graphene can differentiate gas sensing properties with improved reversible reaction. In addition, ternary or multi-compositional 2D layers can be synthesized and investigated to explore new sensing behaviors. For structural effect, sensing characteristic of nanosheet materials can be significantly improved by forming porous structures due to the enhanced gas penetration through the pores. Furthermore, nanopores can generate active reaction sites by increasing density of edge sites. On sensor fabrication aspect, integration of nanosheet materials on a flexible substrate will be futuristic approach for application in real-time wearable sensors. Although several 2D nanomaterials have been integrated on plastic substrates for demonstration of flexible gas sensors, majority 2D nanomaterials were evaluated on rigid substrates due to difficulty in their fabrication on flexible substrates. Moreover, the sensing performance of the 2D nanomaterials on flexible sensor should be further improved in terms of sensitivity and reliability under mechanical stress. New synthesis techniques compatible with flexible substrate can provide new wearable sensing platforms. Based on the current research state and future perspectives, there are still numerous

opportunities for exploring diverse 2D nanomaterials by elaborate manipulation of compositions, microstructures, and sensor fabrication techniques.

Acknowledgements

This work was supported by Wearable Platform Materials Technology Center (WMC) funded by the National Research Foundation of Korea (NRF) Grant of the Korean Government (MSIP; No. 2016R1A5A1009926). This material is based upon work supported by the Ministry of Trade, Industry & Energy (MOTIE, Korea) under Industrial Technology Innovation Program (No.10070075). This research was supported by Research and Business Development Program through the Korea Institute for Advancement of Technology (KIAT) funded by the Ministry of Trade, Industry and Energy (MOTIE) (No. N0002418). This study was supported by Ministry of Science, ICT & Future Planning as Biomedical Treatment Technology Development Project (2015M3A9D7067418).

References

1. C. Tan, X. Cao, X. J. Wu, Q. He, J. Yang, X. Zhang, J. Chen, W. Zhao, S. Han, G. H. Nam, M. Sindoro, H. Zhang, *Chem. Rev.*, **117,** 6225 (2017).

2. S. A. Han, R. Bhatia, S.-W. Kim, *Nano Convergence*, **2,** 17, (2015).

3. W. Choi, N. Choudhary, G. H. Han, J. Park, D. Akinwande, Y. H. Lee, *Mater. Today*, **20,** 116 (2017).

4. K. J. Koski, Y. Cui, *ACS Nano*, **7,** 3739 (2013).

5. S. Z. Butler, S. M. Hollen, L. Y. Cao, Y. Cui, J. A. Gupta, H. R. Gutierrez, T. F. Heinz, S. S. Hong, J. X. Huang, A. F. Ismach, E. Johnston-Halperin, M. Kuno, V. V. Plashnitsa, R. D. Robinson, R. S. Ruoff, S. Salahuddin, J. Shan, L. Shi, M. G. Spencer, M. Terrones, W. Windl, J. E. Goldberger, *ACS Nano*, **7,** 2898 (2013).

6. P. K. Kannan, D. J. Late, H. Morgan, C. S. Rout, *Nanoscale*, **7,** 13293 (2015).

7. M. Park, T. P. Nguyen, K. S. Choi, J. Park, A. Ozturk, S. Y. Kim, *Electron. Mater. Lett.*, **13,** 344 (2017).

8. C. Xie, C. Mak, X. Tao, F. Yan, *Adv. Func. Mater.*, **27,** 1603886 (2017).

9. A. Takagaki, C. Tagusagawa, S. Hayashi, M. Hara, K. Domen, *Energy Environ. Sci.*, **3,** 82 (2010).

10. J. Shen, Y. Zhu, H. Jiang, C. Li, *Nano Today*, **11,** 483 (2016).

11. D. Ghosh, S. O. Kim, *Electron. Mater. Lett.*, **11,** 719 (2015).

12. H. T. Tan, W. Sun, L. Wang, Q. Yan, *Chem. Nano Mat.*, **2,** 562 (2016).

13. R. Kurapati, K. Kostarelos, M. Prato, A. Bianco, *Adv. Mater.*, **28,** 6052 (2016).

14. G. Yang, C. Zhu, D. Du, J. Zhu, Y. Lin, *Nanoscale*, **7,** 14217 (2015).

15. Y. Chen, C. Tan, H. Zhang, L. Wang, *Chem. Soc. Rev.*, **44,** 2681 (2015).

16. J. Ping, Z. Fan, M. Sindoro, Y. Ying, H. Zhang, *Adv. Func. Mater.*, **27,** 1605817 (2017).

17. S. Yang, C. Jiang, S.-h. Wei, *Appl. Phys. Rev.*, **4,** 021304 (2017).

18. X. Liu, T. Ma, N. Pinna, J. Zhang, *Advanced Functional Materials*, **27,** 1702168 (2017).

19. W. Yang, L. Gan, H. Li, T. Zhai, *Inorg. Chem. Front.*, **3,** 433 (2016).

20. T. Wang, D. Huang, Z. Yang, S. Xu, G. He, X. Li, N. Hu, G. Yin, D. He, L. Zhang, *Nano-Micro Lett.*, **8,** 95 (2015).

21. G. Neri, *Chemosensors*, **5,** 21 (2017).

22. K. Toda, R. Furue, S. Hayami, *Anal. Chim. Acta*, **878,** 43 (2015).

23. F. Yavari, N. Koratkar, *J. Phys. Chem. Lett.*, **3,** 1746 (2012).

24. T. Kim, Y. Kim, S. Park, S. Kim, H. Jang, *Chemosensors*, **5,** 15 (2017).

25. K. Chan, C. Tsai, H. A. Hansen, J. K. Nørskov, *Chem. Cat. Chem*, **6,** 1899 (2014).

26. D. Akinwande, N. Petrone, J. Hone, *Nat. Commun.*, **5,** 5678 (2014).

27. S. J. Kim, K. Choi, B. Lee, Y. Kim, B. H. Hong, *Annu. Rev. Mater. Res.*, **45,** 63 (2015).

28. E. Singh, M. Meyyappan, H. S. Nalwa, *ACS Appl. Mater. Interfaces*, **9,** 34544 (2017).

29. Z. Qin, D. Zeng, J. Zhang, C. Wu, Y. Wen, B. Shan, C. Xie, *Appl. Surf. Sci.*, **414,** 244 (2017).

30. D. J. Late, Y. K. Huang, B. Liu, J. Acharya, S. N. Shirodkar, J. J. Luo, A. M. Yan, D. Charles, U. V. Waghmare, V. P. Dravid, C. N. R. Rao, *ACS Nano*, **7,** 4879 (2013).

31. B. L. Liu, L. Chen, G. Liu, A. N. Abbas, M. Fathi, C. W. Zhou, *ACS Nano*, **8,** 5304 (2014).

32. F. Schedin, A. K. Geim, S. V. Morozov, E. W. Hill, P. Blake, M. I. Katsnelson, K. S. Novoselov, *Nat. Mater.*, **6,** 652 (2007).

33. S. Basu, P. Bhattacharyya, *Sens. Actuators B*, **173,** 1 (2012).

34. W. Yuan, G. Shi, *J. Mater. Chem. A*, **1,** 10078 (2013).

35. S. S. Varghese, S. Lonkar, K. K. Singh, S. Swaminathan, A. Abdala, *Sens. Actuators B*, **218,** 160 (2015).

36. Y. R. Choi, Y.-G. Yoon, K. S. Choi, J. H. Kang, Y.-S. Shim, Y. H. Kim, H. J. Chang, J.-H. Lee, C. R. Park, S. Y. Kim, H. W. Jang, *Carbon*, **91,** 178 (2015).

37. J. D. Fowler, M. J. Allen, V. C. Tung, Y. Yang, R. B. Kaner, B. H. Weiller, *ACS Nano*, **3,** 301 (2009).

38. Y. Y. Wang, L. L. Zhang, N. T. Hu, Y. Wang, Y. F. Zhang, Z. H. Zhou, Y. H. Liu, S. Shen, C. S. Peng, *Nanoscale Res. Lett.*, **9,** 1 (2014).

39. G. Lu, L. E. Ocola, J. Chen, *Nanotechnology*, **20,** 445502 (2009).

40. P.-G. Su, H.-C. Shieh, *Sens. Actuators B*, **190,** 865 (2014).

41. R. Y. Gengler, D. S. Badali, D. Zhang, K. Dimos, K. Spyrou, D. Gournis, R. J. Miller, *Nat. Commun.*, **4,** 2560 (2013).

42. S. H. Park, H. S. Kim, *Nanotechnology*, **26,** 205601 (2015).

43. B. Senyuk, N. Behabtu, A. Martinez, T. Lee, D. E. Tsentalovich, G. Ceriotti, J. M. Tour, M. Pasquali, Smalyukh, II, *Nat. Commun.*, **6,** 7157 (2015).

44. L. Huang, Y. Liu, L.-C. Ji, Y.-Q. Xie, T. Wang, W.-Z. Shi, *Carbon*, **49,** 2431 (2011).

45. E. B. Secor, B. Y. Ahn, T. Z. Gao, J. A. Lewis, M. C. Hersam, *Adv. Mater.*, **27,** 6683 (2015).

46. E. Kymakis, K. Savva, M. M. Stylianakis, C. Fotakis, E. Stratakis, *Adv. Func. Mater.*, **23,** 2742 (2013).

47. S.-J. Choi, S.-J. Kim, I.-D. Kim, *NPG Asia Mater.*, **8,** e315 (2016).

48. W. Yuan, A. Liu, L. Huang, C. Li, G. Shi, *Adv. Mater.*, **25,** 766 (2013).

49. Y. H. Kim, J. S. Park, Y.-R. Choi, S. Y. Park, S. Y. Lee, W. Sohn, Y.-S. Shim, J.-H. Lee, C. R. Park, Y. S. Choi, B. H. Hong, J. H. Lee, W. H. Lee, D. Lee, H. W. Jang, *J. Mater. Chem. A*, **5,** 19116 (2017).

50. M.-S. Park, K. H. Kim, M.-J. Kim, Y.-S. Lee, *Colloids Surf., A*, **490,** 104 (2016).

51. R. T. Lv, G. G. Chen, Q. Li, A. McCreary, A. Botello-Mendez, S. V. Morozov, L. B. Liang, X. Declerck, N. Perea-Lopez, D. A. Culleni, S. M. Feng, A. L. Elias, R. Cruz-Silva, K. Fujisawa, M. Endo, F. Y. Kang, J. C. Charlier, V. Meunier, M. H. Pan, A. R. Harutyunyan, K. S. Novoselov, M. Terrones, *P. Natl. Acad. Sci. USA*, **112,** 14527 (2015).

52. G. Lee, G. Yang, A. Cho, J. W. Han, J. Kim, *Phys. Chem. Chem. Phys.*, **18,** 14198 (2016).

53. B. Kumar, K. Min, M. Bashirzadeh, A. B. Farimani, M. H. Bae, D. Estrada, Y. D. Kim, P. Yasaei, Y. D. Park, E. Pop, N. R. Aluru, A. Salehi-Khojin, *Nano Lett.*, **13,** 1962 (2013).

54. G. Yang, C. Lee, J. Kim, F. Ren, S. J. Pearton, *Phys. Chem. Chem. Phys.*, **15,** 1798 (2013).

55. R. Ghosh, A. Singh, S. Santra, S. K. Ray, A. Chandra, P. K. Guha, *Sens. Actuators B*, **205,** 67 (2014).

56. S. Kumar, S. Kaushik, R. Pratap, S. Raghavan, *ACS Appl. Mater. Interfaces*, **7,** 2189 (2015).

57. H. Choi, H. Y. Jeong, D.-S. Lee, C.-G. Choi, S.-Y. Choi, *Carbon Lett.*, **14,** 186 (2013).

58. M. W. Jung, S. Myung, W. Song, M. A. Kang, S. H. Kim, C. S. Yang, S. S. Lee, J. Lim, C. Y. Park, J. O. Lee, K. S. An, *ACS Appl. Mater. Interfaces*, **6,** 13319 (2014).

59. Y. H. Kim, S. J. Kim, Y. J. Kim, Y. S. Shim, S. Y. Kim, B. H. Hong, H. W. Jang, *ACS Nano*, **9,** 10453 (2015).

60. H. Choi, J. S. Choi, J. S. Kim, J. H. Choe, K. H. Chung, J. W. Shin, J. T. Kim, D. H. Youn, K. C. Kim, J. I. Lee, S. Y. Choi, P. Kim, C. G. Choi, Y. J. Yu, *Small*, **10,** 3685 (2014).

61. S. Hong, H. Lee, J. Lee, J. Kwon, S. Han, Y. D. Suh, H. Cho, J. Shin, J. Yeo, S. H. Ko, *Adv. Mater.*, **27,** 4744 (2015).

62. B. W. An, E. J. Gwak, K. Kim, Y. C. Kim, J. Jang, J. Y. Kim, J. U. Park, *Nano Lett.*, **16,** 471 (2016).

63. A. Khan, S. Lee, T. Jang, Z. Xiong, C. Zhang, J. Tang, L. J. Guo, W. D. Li, *Small*, **12,** 3021 (2016).

64. S. J. Choi, H. J. Choi, W. T. Koo, D. Huh, H. Lee, I. D. Kim, *ACS Appl. Mater. Interfaces*, (2017).

65. S. J. Choi, S. J. Kim, J. S. Jang, J. H. Lee, I. D. Kim, *Small*, **12,** 5826 (2016).

66. W. W. Li, X. M. Geng, Y. F. Guo, J. Z. Rong, Y. P. Gong, L. Q. Wu, X. M. Zhang, P. Li, J. B. Xu, G. S. Cheng, M. T. Sun, L. W. Liu, *ACS Nano*, **5,** 6955 (2011).

67. M. G. Chung, D.-H. Kim, D. K. Seo, T. Kim, H. U. Im, H. M. Lee, J.-B. Yoo, S.-H. Hong, T. J. Kang, Y. H. Kim, *Sens. Actuators B*, **169,** 387 (2012).

68. D. H. Shin, J. S. Lee, J. Jun, J. H. An, S. G. Kim, K. H. Cho, J. Jang, *Sci. Rep.*, **5,** 12294 (2015).

69. J. S. Lee, J. Oh, J. Jun, J. Jang, *ACS Nano*, **9,** 7783 (2015).

70. L. Huang, Z. Wang, J. Zhang, J. Pu, Y. Lin, S. Xu, L. Shen, Q. Chen, W. Shi, *ACS Appl. Mater. Interfaces*, **6,** 7426 (2014).

71. B. Cho, J. Yoon, M. G. Hahm, D.-H. Kim, A. R. Kim, Y. H. Kahng, S.-W. Park, Y.-J. Lee, S.-G. Park, J.-D. Kwon, C. S. Kim, M. Song, Y. Jeong, K.-S. Nam, H. C. Ko, *J. Mater. Chem. C*, **2,** 5280 (2014).

72. S. Gupta Chatterjee, S. Chatterjee, A. K. Ray, A. K. Chakraborty, *Sens. Actuators B*, **221,** 1170 (2015).

73. Z. Jiang, J. Li, H. Aslan, Q. Li, Y. Li, M. Chen, Y. Huang, J. P. Froning, M. Otyepka, R. Zbořil, F. Besenbacher, M. Dong, *J. Mater. Chem. A*, **2,** 6714 (2014).

74. S. J. Choi, F. Fuchs, R. Demadrille, B. Grevin, B. H. Jang, S. J. Lee, J. H. Lee, H. L. Tuller, I. D. Kim, *ACS Appl. Mater. Interfaces*, **6,** 9061 (2014).

75. S. J. Choi, C. Choi, S. J. Kim, H. J. Cho, M. Hakim, S. Jeon, I. D. Kim, *Sci. Rep.*, **5,** 8067 (2015).

76. S.-J. Choi, C. Choi, S.-J. Kim, H.-J. Cho, S. Jeon, I.-D. Kim, *RSC Adv.*, **5,** 7584 (2015).

77. S. J. Choi, B. H. Jang, S. J. Lee, B. K. Min, A. Rothschild, I. D. Kim, *ACS Appl. Mater. Interfaces*, **6,** 2588 (2014).

78. X. Chu, R. Hu, J. Wang, Y. Dong, W. Zhang, L. Bai, W. Sun, *Sens. Actuators B*, **251,** 120 (2017).

79. A. Chen, R. Liu, X. Peng, Q. Chen, J. Wu, *ACS Appl. Mater. Interfaces*, **9,** 37191 (2017).

80. S. Zhang, N. T. Hang, Z. Zhang, H. Yue, W. Yang, *Nanomaterials*, **7,** 12 (2017).

81. N. T. Hang, S. Zhang, W. Yang, *Sens. Actuators B*, **248,** 940 (2017).

82. J. Hu, C. Zou, Y. Su, M. Li, N. Hu, H. Ni, Z. Yang, Y. Zhang, *J. Mater. Chem. C*, **5,** 6862 (2017).

83. L. T. Duy, T. Q. Trung, A. Hanif, S. Siddiqui, E. Roh, W. Lee, N.-E. Lee, *2D Mater.*, **4,** (2017).

84. Y. J. Yun, W. G. Hong, N. J. Choi, B. H. Kim, Y. Jun, H. K. Lee, *Sci. Rep.*, **5,** 10904 (2015).

85. Y. Seekaew, S. Lokavee, D. Phokharatkul, A. Wisitsoraat, T. Kerdcharoen, C. Wongchoosuk, *Org. Electron.*, **15,** 2971 (2014).

86. M. G. Chung, D. H. Kim, H. M. Lee, T. Kim, J. H. Choi, D. k. Seo, J.-B. Yoo, S.-H. Hong, T. J. Kang, Y. H. Kim, *Sens. Actuators B*, **166-167,** 172 (2012).

87. D. H. Wang, Y. Hu, J. J. Zhao, L. L. Zeng, X. M. Tao, W. Chen, *J. Mater. Chem. A*, **2,** 17415 (2014).

88. P. Yasaei, B. Kumar, R. Hantehzadeh, M. Kayyalha, A. Baskin, N. Repnin, C. Wang, R. F. Klie, Y. P. Chen, P. Kral, A. Salehi-Khojin, *Nat. Commun.*, **5,** 4911 (2014).

89. X. Wang, Z. Xiong, Z. Liu, T. Zhang, *Adv. Mater.*, **27,** 1370 (2015).

90. Q. H. Wang, K. Kalantar-Zadeh, A. Kis, J. N. Coleman, M. S. Strano, *Nat. Nanotechnol.*, **7,** 699 (2012).

91. R. Lv, J. A. Robinson, R. E. Schaak, D. Sun, Y. Sun, T. E. Mallouk, M. Terrones, *Acc. Chem. Res.*, **48,** 56 (2015).

92. F. Wang, Z. Wang, Q. Wang, F. Wang, L. Yin, K. Xu, Y. Huang, J. He, *Nanotechnology*, **26,** 292001 (2015).

93. D. M. Andoshe, J.-M. Jeon, S. Y. Kim, H. W. Jang, *Electron. Mater. Lett.*, **11,** 323 (2015).

94. K. Kalantar-zadeh, J. Z. Ou, T. Daeneke, A. Mitchell, T. Sasaki, M. S. Fuhrer, *Appl. Mater. Today*, **5,** 73 (2016).

95. X. Li, J. Shan, W. Zhang, S. Su, L. Yuwen, L. Wang, *Small*, **13,** 1602660 (2017).

96. X. Huang, Z. Zeng, H. Zhang, *Chem. Soc. Rev.*, **42,** 1934 (2013).

97. H. Li, J. Wu, Z. Yin, H. Zhang, *Acc. Chem. Res.*, **47,** 1067 (2014).

98. Y. Tao, X. Wu, W. Wang, J. Wang, *J. Mater. Chem. C*, **3,** 1347 (2015).

99. C. Tan, P. Yu, Y. Hu, J. Chen, Y. Huang, Y. Cai, Z. Luo, B. Li, Q. Lu, L. Wang, Z. Liu, H. Zhang, *J. Am. Chem. Soc.*, **137,** 10430 (2015).

100. B. L. Li, J. Wang, H. L. Zou, S. Garaj, C. T. Lim, J. Xie, N. B. Li, D. T. Leong, *Adv. Func. Mater.*, **26,** 7034 (2016).

101. M. Park, Y. J. Park, X. Chen, Y. K. Park, M. S. Kim, J. H. Ahn, *Adv. Mater.*, **28,** 2556 (2016).

102. W. Zhang, P. Zhang, Z. Su, G. Wei, *Nanoscale*, **7,** 18364 (2015).

103. Y. Huang, J. Guo, Y. Kang, Y. Ai, C. M. Li, *Nanoscale*, **7,** 19358 (2015).

104. X. Zhang, Z. Lai, C. Tan, H. Zhang, *Angew. Chem. Int. Ed.*, **55,** 8816 (2016).

105. C. N. R. Rao, U. Maitra, U. V. Waghmare, *Chem. Phys. Lett.*, **609,** 172 (2014).

106. H. Li, Z. Yin, Q. He, H. Li, X. Huang, G. Lu, D. W. Fam, A. I. Tok, Q. Zhang, H. Zhang, *Small*, **8,** 63 (2012).

107. F. K. Perkins, A. L. Friedman, E. Cobas, P. M. Campbell, G. G. Jernigan, B. T. Jonker, *Nano Lett.*, **13,** 668 (2013).

108. B. Cho, A. R. Kim, Y. Park, J. Yoon, Y. J. Lee, S. Lee, T. J. Yoo, C. G. Kang, B. H. Lee, H. C. Ko, D. H. Kim, M. G. Hahm, *ACS Appl. Mater. Interfaces*, **7,** 2952 (2015).

109. K. Lee, R. Gatensby, N. McEvoy, T. Hallam, G. S. Duesberg, *Adv. Mater.*, **25,** 6699 (2013).

110. S. Y. Cho, S. J. Kim, Y. Lee, J. S. Kim, W. B. Jung, H. W. Yoo, J. Kim, H. T. Jung, *ACS Nano*, **9,** 9314 (2015).

111. T. F. Jaramillo, K. P. Jorgensen, J. Bonde, J. H. Nielsen, S. Horch, I. Chorkendorff, *Science*, **317,** 100 (2007).

112. K. Y. Ko, J. G. Song, Y. Kim, T. Choi, S. Shin, C. W. Lee, K. Lee, J. Koo, H. Lee, J. Kim, T. Lee, J. Park, H. Kim, *ACS Nano*, **10,** 9287 (2016).

113. C. Zhou, W. Yang, H. Zhu, *J. Chem. Phys.*, **142,** 214704 (2015).

114. D. J. Late, T. Doneux, M. Bougouma, *Appl. Phys. Lett.*, **105,** 233103 (2014).

115. S. Zhang, T. H. Nguyen, W. Zhang, Y. Park, W. Yang, *Appl. Phys. Lett.*, **111,** 092104 (2017).

116. C. Yim, K. Lee, N. McEvoy, M. O'Brien, S. Riazimehr, N. C. Berner, C. P. Cullen, J. Kotakoski, J. C. Meyer, M. C. Lemme, G. S. Duesberg, *ACS Nano*, **10,** 9550 (2016).

117. A. Yang, J. Gao, B. Li, J. Tan, Y. Xiang, T. Gupta, L. Li, S. Suresh, J. C. Idrobo, T.-M. Lu, M. Rong, N. Koratkar, *2D Mater.*, **3,** 045012 (2016).

118. S.-L. Zhang, H.-H. Choi, H.-Y. Yue, W.-C. Yang, *Curr. Appl. Phys.*, **14,** 264 (2014).

119. J. Feng, L. Peng, C. Wu, X. Sun, S. Hu, C. Lin, J. Dai, J. Yang, Y. Xie, *Adv. Mater.*, **24,** 1969 (2012).

120. R. K. Jha, P. K. Guha, *Nanotechnology*, **27,** 475503 (2016).

121. B. Cho, J. Yoon, S. K. Lim, A. R. Kim, S. Y. Choi, D. H. Kim, K. H. Lee, B. H. Lee, H. C. Ko, M. G. Hahm, *Sensors*, **15,** 24903 (2015).

122. S. Y. Cho, H. J. Koh, H. W. Yoo, J. S. Kim, H. T. Jung, *ACS Sens.*, **2,** 183 (2017).

123. S. Y. Choi, Y. Kim, H. S. Chung, A. R. Kim, J. D. Kwon, J. Park, Y. L. Kim, S. H. Kwon, M. G. Hahm, B. Cho, *ACS Appl. Mater. Interfaces*, **9,** 3817 (2017).

124. C. Kuru, C. Choi, A. Kargar, D. Choi, Y. J. Kim, C. H. Liu, S. Yavuz, S. Jin, *Adv. Sci.*, **2,** 1500004 (2015).

125. Q. He, Z. Zeng, Z. Yin, H. Li, S. Wu, X. Huang, H. Zhang, *Small*, **8,** 2994 (2012).

126. Z. Zeng, Z. Yin, X. Huang, H. Li, Q. He, G. Lu, F. Boey, H. Zhang, *Angew. Chem. Int. Ed.*, **50,** 11093 (2011).

127. Z. Qin, C. Ouyang, J. Zhang, L. Wan, S. Wang, C. Xie, D. Zeng, *Sens. Actuators B*, **253,** 1034 (2017).

128. S. Cui, Z. Wen, X. Huang, J. Chang, J. Chen, *Small*, **11,** 2305 (2015).

129. Y. Dai, X. Wu, D. Sha, M. Chen, H. Zou, J. Ren, J. Wang, X. Yan, *Electron. Mater. Lett.*, **12,** 789 (2016).

130. J.-H. Cha, S.-J. Choi, S. Yu, I.-D. Kim, *J. Mater. Chem. A*, **5,** 8725 (2017).

131. M. O'Brien, K. Lee, R. Morrish, N. C. Berner, N. McEvoy, C. A. Wolden, G. S. Duesberg, *Chem. Phys. Lett.*, **615,** 6 (2014).

132. J. S. Kim, H. W. Yoo, H. O. Choi, H. T. Jung, *Nano Lett.*, **14,** 5941 (2014).

133. J. W. Yoon, J. H. Lee, *Lab Chip*, **17,** 3537 (2017).

134. N. Ma, K. Suematsu, M. Yuasa, T. Kida, K. Shimanoe, *ACS Appl. Mater. Interfaces*, **7,** 5863 (2015).

135. K. Suematsu, Y. Shin, Z. Hua, K. Yoshida, M. Yuasa, T. Kida, K. Shimanoe, *ACS Appl. Mater. Interfaces*, **6,** 5319 (2014).

136. H. S. Woo, C. W. Na, J. H. Lee, *Sensors*, **16,** E1531 (2016).

137. N. Ramgir, N. Datta, M. Kaur, S. Kailasaganapathi, A. K. Debnath, D. K. Aswal, S. K. Gupta, *Colloids Surf., A*, **439,** 101 (2013).

138. S. J. Kim, S. J. Choi, J. S. Jang, H. J. Cho, I. D. Kim, *Acc. Chem. Res.*, **50,** 1587 (2017).

139. S. J. Choi, S. J. Kim, H. J. Cho, J. S. Jang, Y. M. Lin, H. L. Tuller, G. C. Rutledge, I. D. Kim, *Small*, **12,** 911 (2016).

140. S.-J. Choi, L. Persano, A. Camposeo, J.-S. Jang, W.-T. Koo, S.-J. Kim, H.-J. Cho, I.-D. Kim, D. Pisignano, *Macromol. Mater. Eng.*, **302,** 1600569 (2017).

141. J.-S. Jang, S.-J. Choi, S.-J. Kim, M. Hakim, I.-D. Kim, *Adv. Func. Mater.*, **26,** 4740 (2016).

142. S. J. Choi, I. Lee, B. H. Jang, D. Y. Youn, W. H. Ryu, C. O. Park, I. D. Kim, *Anal. Chem.*, **85,** 1792 (2013).

143. S. J. Choi, S. Chattopadhyay, J. J. Kim, S. J. Kim, H. L. Tuller, G. C. Rutledge, I. D. Kim, *Nanoscale*, **8,** 9159 (2016).

144. B. Y. Kim, J. H. Ahn, J. W. Yoon, C. S. Lee, Y. C. Kang, F. Abdel-Hady, A. A. Wazzan, J. H. Lee, *ACS Appl. Mater. Interfaces*, **8,** 34603 (2016).

145. J.-W. Yoon, S. H. Choi, J.-S. Kim, H. W. Jang, Y. C. Kang, J.-H. Lee, *NPG Asia Mater.*, **8,** (2016).

146. Y. Zeng, L. Qiao, Y. Bing, M. Wen, B. Zou, W. Zheng, T. Zhang, G. Zou, *Sens. Actuators B*, **173,** 897 (2012).

147. J. Xu, Z. Xue, N. Qin, Z. Cheng, Q. Xiang, *Sens. Actuators B*, **242,** 148 (2017).

148. P.-Y. Qiao, L.-X. Zhang, M.-Y. Zhu, Y.-Y. Yin, Z.-W. Zhao, H.-N. Sun, J.-Y. Dong, L.-J. Bie, *Sens. Actuators B*, **250,** 189 (2017).

149. R. Khan, S. Raj, J. H. Yun, Y.-T. Yu, J. I. Lee, I.-H. Lee, *Electron. Mater. Lett.*, **12,** 784 (2016).

150. Z. Lou, L. Wang, R. Wang, T. Fei, T. Zhang, *Solid-State Electron.*, **76,** 91 (2012).

151. W. Zeng, M. Wu, Y. Li, S. Wu, *J. Mater. Sci.: Mater. Electron.*, **24,** 3701 (2013).

152. Z. Wang, D. Wang, J. Sun, *Sens. Actuators B*, **245,** 828 (2017).

153. A. Umar, A. A. Alshahrani, H. Algarni, R. Kumar, *Sens. Actuators B*, **250,** 24 (2017).

154. Z. Li, Z. Lin, N. Wang, J. Wang, W. Liu, K. Sun, Y. Q. Fu, Z. Wang, *Sens. Actuators B*, **235,** 222 (2016).

155. S.-M. Li, L.-X. Zhang, M.-Y. Zhu, G.-J. Ji, L.-X. Zhao, J. Yin, L.-J. Bie, *Sens. Actuators B*, **249,** 611 (2017).

156. S.-L. Zhang, J.-O. Lim, J.-S. Huh, J.-S. Noh, W. Lee, *Curr. Appl. Phys.*, **13,** S156 (2013).

157. T. Yu, X. Cheng, X. Zhang, L. Sui, Y. Xu, S. Gao, H. Zhao, L. Huo, *J. Mater. Chem. A*, **3,** 11991 (2015).

158. X. Wang, S. Yao, X. Wu, Z. Shi, H. Sun, R. Que, *RSC Adv.*, **5,** 17938 (2015).

159. X. Wang, J. Su, H. Chen, G. D. Li, Z. Shi, H. Zou, X. Zou, *ACS Appl. Mater. Interfaces*, **9,** 16335 (2017).

160. D. J. Li, Z. Huang, T. H. Hwang, R. Narayan, J. W. Choi, S. O. Kim, *Electron. Mater. Lett.*, **12,** 211 (2016).

161. Z. Sun, T. Liao, Y. Dou, S. M. Hwang, M. S. Park, L. Jiang, J. H. Kim, S. X. Dou, *Nat. Commun.*, **5,** 3813 (2014).

162. X. Rui, Z. Lu, Z. Yin, D. H. Sim, N. Xiao, T. M. Lim, H. H. Hng, H. Zhang, Q. Yan, *Small*, **9,** 716 (2013).

163. S.-J. Choi, J.-S. Jang, H. J. Park, I.-D. Kim, *Adv. Func. Mater.*, **27,** 1606026 (2017).

164. S.-J. Choi, K. H. Ku, B. J. Kim, I.-D. Kim, *ACS Sens.*, **1,** 1124 (2016).

165. J. S. Jang, S. Yu, S. J. Choi, S. J. Kim, W. T. Koo, I. D. Kim, *Small*, **12,** 5989 (2016).

166. S. J. Kim, S. J. Choi, J. S. Jang, N. H. Kim, M. Hakim, H. L. Tuller, I. D. Kim, *ACS Nano*, **10,** 5891 (2016).

167. S. J. Choi, M. P. Kim, S. J. Lee, B. J. Kim, I. D. Kim, *Nanoscale*, **6,** 11898 (2014).

168. S. J. Kim, S. J. Choi, J. S. Jang, H. J. Cho, W. T. Koo, H. L. Tuller, I. D. Kim, *Adv. Mater.*, **29,** 1700737 (2017).

169. J. S. Jang, S. J. Choi, W. T. Koo, S. J. Kim, J. Y. Cheong, I. D. Kim, *ACS Appl. Mater. Interfaces*, **9,** 24821 (2017).

170. Y. Masuda, T. Itoh, W. Shin, K. Kato, *Sci. Rep.*, **5,** 10122 (2015).

171. Y. Cao, Y. He, X. Zou, G.-D. Li, *Sens. Actuators B*, **252,** 232 (2017).

172. Z. Chen, Z. Lin, M. Xu, Y. Hong, N. Li, P. Fu, Z. Chen, *Electron. Mater. Lett.*, **12,** 343 (2016).

173. Y. Li, H. Ban, H. Zhao, M. Yang, *RSC Adv.*, **5,** 106945 (2015).

174. Y. Li, H. Zhao, H. Ban, M. Yang, *Sens. Actuators B*, **245,** 34 (2017).

175. M. B. Rahmani, M. H. Yaacob, Y. M. Sabri, *Sens Actuators B*, **251,** 57 (2017).

176. G. Li, X. Wang, L. Liu, R. Liu, F. Shen, Z. Cui, W. Chen, T. Zhang, *Small*, **11,** 731 (2015).

177. P. Deria, J. E. Mondloch, O. Karagiaridi, W. Bury, J. T. Hupp, O. K. Farha, *Chem. Soc. Rev.*, **43,** 5896 (2014).

178. K. Adil, Y. Belmabkhout, R. S. Pillai, A. Cadiau, P. M. Bhatt, A. H. Assen, G. Maurin, M. Eddaoudi, *Chem. Soc. Rev.*, **46,** 3402 (2017).

179. L. Chen, R. Luque, Y. Li, *Chem. Soc. Rev.*, **46,** 4614 (2017).

180. M. Hmadeh, Z. Lu, Z. Liu, F. Gándara, H. Furukawa, S. Wan, V. Augustyn, R. Chang, L. Liao, F. Zhou, E. Perre, V. Ozolins, K. Suenaga, X. Duan, B. Dunn, Y. Yamamto, O. Terasaki, O. M. Yaghi, *Chem. Mater.*, **24,** 3511 (2012).

181. T. Kambe, R. Sakamoto, K. Hoshiko, K. Takada, M. Miyachi, J. H. Ryu, S. Sasaki, J. Kim, K. Nakazato, M. Takata, H. Nishihara, *J. Am. Chem. Soc.*, **135,** 2462 (2013).

182. D. Sheberla, L. Sun, M. A. Blood-Forsythe, S. Er, C. R. Wade, C. K. Brozek, A. Aspuru-Guzik, M. Dinca, *J. Am. Chem. Soc.*, **136,** 8859 (2014).

183. T. Rodenas, I. Luz, G. Prieto, B. Seoane, H. Miro, A. Corma, F. Kapteijn, I. X. F. X. Llabres, J. Gascon, *Nat. Mater.*, **14,** 48 (2015).

184. M.-H. Pham, G.-T. Vuong, F.-G. Fontaine, T.-O. Do, *Cryst. Growth Des.*, **12,** 3091 (2012).

185. Y. Peng, Y. Li, Y. Ban, W. Yang, *Angew. Chem. Int. Ed.*, **56,** 9757 (2017).

186. M. G. Campbell, D. Sheberla, S. F. Liu, T. M. Swager, M. Dinca, *Angew. Chem. Int. Ed.*, **54,** 4349 (2015).

187. M. G. Campbell, S. F. Liu, T. M. Swager, M. Dinca, *J. Am. Chem. Soc.*, **137,** 13780 (2015).

188. P. Falcaro, R. Ricco, A. Yazdi, I. Imaz, S. Furukawa, D. Maspoch, R. Ameloot, J. D. Evans, C. J. Doonan, *Coord. Chem. Rev.*, **307,** 237 (2016).

189. W. T. Koo, S. J. Choi, S. J. Kim, J. S. Jang, H. L. Tuller, I. D. Kim, *J. Am. Chem. Soc.*, **138,** 13431 (2016).

190. W. T. Koo, J. S. Jang, S. J. Choi, H. J. Cho, I. D. Kim, *ACS Appl. Mater. Interfaces*, **9,** 18069 (2017).

191. W. T. Koo, S. Yu, S. J. Choi, J. S. Jang, J. Y. Cheong, I. D. Kim, *ACS Appl. Mater. Interfaces*, **9,** 8201 (2017).

192. W. T. Koo, S. J. Choi, J. S. Jang, I. D. Kim, *Sci. Rep.*, **7,** 45074 (2017).

193. J. S. Jang, W. T. Koo, S. J. Choi, I. D. Kim, *J. Am. Chem. Soc.*, **139,** 11868 (2017).

194. V. Eswaraiah, Q. Zeng, Y. Long, Z. Liu, *Small*, **12,** 3480 (2016).

195. D. Hanlon, C. Backes, E. Doherty, C. S. Cucinotta, N. C. Berner, C. Boland, K. Lee, A. Harvey, P. Lynch, Z. Gholamvand, S. Zhang, K. Wang, G. Moynihan, A. Pokle, Q. M. Ramasse, N. McEvoy, W. J. Blau, J. Wang, G. Abellan, F. Hauke, A. Hirsch, S. Sanvito, D. D. O'Regan, G. S. Duesberg, V. Nicolosi, J. N. Coleman, *Nat. Commun.*, **6,** 8563 (2015).

196. S. Cui, H. Pu, S. A. Wells, Z. Wen, S. Mao, J. Chang, M. C. Hersam, J. Chen, *Nat. Commun.*, **6,** 8632 (2015).

197. A. N. Abbas, B. L. Liu, L. Chen, Y. Q. Ma, S. Cong, N. Aroonyadet, M. Kopf, T. Nilges, C. W. Zhou, *ACS Nano*, **9,** 5618 (2015).

198. S. Y. Cho, Y. Lee, H. J. Koh, H. Jung, J. S. Kim, H. W. Yoo, J. Kim, H. T. Jung, *Adv. Mater.*, **28,** 7020 (2016).

199. P. Yasaei, A. Behranginia, T. Foroozan, M. Asadi, K. Kim, F. Khalili-Araghi, A. Salehi-Khojin, *ACS Nano*, **9,** 9898 (2015).

200. M. B. Erande, M. S. Pawar, D. J. Late, *ACS Appl. Mater. Interfaces*, **8,** 11548 (2016).

201. D. J. Late, *Microporous Mesoporous Mater.*, **225,** 494 (2016).

202. J. Miao, L. Cai, S. Zhang, J. Nah, J. Yeom, C. Wang, *ACS Appl. Mater. Interfaces*, **9,**

10019 (2017).

203. S.-Y. Cho, H.-J. Koh, H.-W. Yoo, H.-T. Jung, *Chem. Mater.*, **29,** 7197 (2017).

204. Y. Zhao, H. Wang, H. Huang, Q. Xiao, Y. Xu, Z. Guo, H. Xie, J. Shao, Z. Sun, W. Han, X. F. Yu, P. Li, P. K. Chu, *Angew. Chem. Int. Ed.*, **55,** 5003 (2016).

205. M. Buscema, D. J. Groenendijk, S. I. Blanter, G. A. Steele, H. S. van der Zant, A. Castellanos-Gomez, *Nano Lett.*, **14,** 3347 (2014).

206. C. Hao, F. Wen, J. Xiang, S. Yuan, B. Yang, L. Li, W. Wang, Z. Zeng, L. Wang, Z. Liu, Y. Tian, *Adv. Func. Mater.*, **26,** 2016 (2016).

207. J. Hu, Z. Guo, P. E. McWilliams, J. E. Darges, D. L. Druffel, A. M. Moran, S. C. Warren, *Nano Lett.*, **16,** 74 (2016).

208. M. Naguib, V. N. Mochalin, M. W. Barsoum, Y. Gogotsi, *Adv. Mater.*, **26,** 992 (2014).

209. M. W. Barsoum, *Max Phases: Properties of Machinable Ternary Carbides and Nitrides*, 1 (2013).

210. M. Naguib, O. Mashtalir, J. Carle, V. Presser, J. Lu, L. Hultman, Y. Gogotsi, M. W. Barsoum, *ACS Nano*, **6,** 1322 (2012).

211. B. Anasori, M. R. Lukatskaya, Y. Gogotsi, *Nat. Rev. Mater.*, **2,** 16098 (2017).

212. M. Naguib, J. Halim, J. Lu, K. M. Cook, L. Hultman, Y. Gogotsi, M. W. Barsoum, *J. Am. Chem. Soc.*, **135,** 15966 (2013).

213. M. R. Lukatskaya, O. Mashtalir, C. E. Ren, Y. Dall'Agnese, P. Rozier, P. L. Taberna, M. Naguib, P. Simon, M. W. Barsoum, Y. Gogotsi, *Science*, **341,** 1502 (2013).

214. X. Xie, S. Chen, W. Ding, Y. Nie, Z. Wei, *Chem. Commun.*, **49,** 10112 (2013).

215. J. Zhu, E. Ha, G. Zhao, Y. Zhou, D. Huang, G. Yue, L. Hu, N. Sun, Y. Wang, L. Y. S. Lee, C. Xu, K.-Y. Wong, D. Astruc, P. Zhao, *Coord. Chem. Rev.*, **352,** 306 (2017).

216. X. F. Yu, Y. C. Li, J. B. Cheng, Z. B. Liu, Q. Z. Li, W. Z. Li, X. Yang, B. Xiao, *ACS Appl. Mater. Interfaces*, **7,** 13707 (2015).

217. M. Khazaei, M. Arai, T. Sasaki, C.-Y. Chung, N. S. Venkataramanan, M. Estili, Y. Sakka, Y. Kawazoe, *Adv. Func. Mater.*, **23,** 2185 (2013).

218. E. Lee, A. VahidMohammadi, B. C. Prorok, Y. S. Yoon, M. Beidaghi, D. J. Kim, *ACS Appl. Mater. Interfaces*, **9,** 37184 (2017).

219. N. A. Kumar, M. A. Dar, R. Gul, J.-B. Baek, *Mater. Today*, **18,** 286 (2015).

220. C. Tan, H. Zhang, *J. Am. Chem. Soc.*, **137,** 12162 (2015).

221. Z.-W. Chen, Y.-Y. Hong, Z.-D. Lin, L.-M. Liu, X.-W. Zhang, *Electron. Mater. Lett.*, **13,** 270 (2017).

222. L. T. Hoa, H. N. Tien, V. H. Luan, J. S. Chung, S. H. Hur, *Sens. Actuators B*, **185,** 701 (2013).

223. J. Shi, Z. Cheng, L. Gao, Y. Zhang, J. Xu, H. Zhao, *Sens. Actuators B*, **230,** 736 (2016).

224. B. Cho, J. Yoon, S. K. Lim, A. R. Kim, D. H. Kim, S. G. Park, J. D. Kwon, Y. J. Lee, K. H. Lee, B. H. Lee, H. C. Ko, M. G. Hahm, *ACS Appl. Mater. Interfaces*, **7,** 16775 (2015).

225. H. Long, A. Harley-Trochimczyk, T. Pham, Z. Tang, T. Shi, A. Zettl, C. Carraro, M. A. Worsley, R. Maboudian, *Adv. Func. Mater.*, **26,** 5158 (2016).

226. B. Cho, A. R. Kim, D. J. Kim, H. S. Chung, S. Y. Choi, J. D. Kwon, S. W. Park, Y. Kim, B. H. Lee, K. H. Lee, D. H. Kim, J. Nam, M. G. Hahm, *ACS Appl. Mater. Interfaces*, **8,** 19635 (2016).

227. J. Bao, K. Jeppson, M. Edwards, Y. Fu, L. Ye, X. Lu, J. Liu, *Electron. Mater. Lett.*, **12,** 1 (2016).

228. G. C. Constantinescu, N. D. Hine, *Nano Lett.*, **16,** 2586 (2016).

229. G. Gao, W. Gao, E. Cannuccia, J. Taha-Tijerina, L. Balicas, A. Mathkar, T. N. Narayanan, Z. Liu, B. K. Gupta, J. Peng, Y. Yin, A. Rubio, P. M. Ajayan, *Nano Lett.*, **12,** 3518 (2012).

230. S. Das, R. Gulotty, A. V. Sumant, A. Roelofs, *Nano Lett.*, **14,** 2861 (2014).

The table of contents